NUREG/CR-4508
SAND85-1726
R1, R3, R5
Printed April 1988

Behavior of a Corium Jet in High Pressure Melt Ejection From a Reactor Pressure Vessel

Wiktor Frid

Prepared by
Sandia National Laboratories
Albuquerque, New Mexico 87185 and Livermore, California 94550
for the United States Department of Energy
under Contract DE-AC04-76DP00789

Prepared for
U. S. NUCLEAR REGULATORY COMMISSION

Available from

Superintendent of Documents
U.S. Government Printing Office
Post Office Box 37082
Washington, D.C. 20013-7082

and

National Technical Information Service
Springfield, VA 22161

NUREG/CR-4508
SAND85-1726
R1, R3, R5

BEHAVIOR OF A CORIUM JET IN HIGH PRESSURE MELT EJECTION FROM A REACTOR PRESSURE VESSEL*

Wiktor Frid**

April 1988

Sandia National Laboratories
Albuquerque, NM 87185
Operated by
Sandia Corporation
for the
U.S. Department of Energy

Prepared for
Division of Accident Evaluation
Office of Nuclear Regulatory Research
U.S. Nuclear Regulatory Commission
Washington, DC 20555
NRC FIN 1406

*Work supported by the U.S. Nuclear Regulatory Commission, the Swedish Nuclear Power Inspectorate, and the Swedish State Power Board.

**On assignment from the Swedish State Power Board.

ABSTRACT

Discharge of the molten core debris from a pressurized reactor vessel has been recognized as an important accident scenario for pressurized water reactors. Recent high-pressure melt streaming experiments conducted at Sandia National Laboratories, designed to study cavity and containment events related to melt ejection, have resulted in two important observations:

1. Expansion and breakup of the ejected molten jet.

2. Significant aerosol generation during the ejection process.

The expansion and breakup of the jet in the experiments are attributed to rapid evolution of the pressurizing gas (nitrogen or hydrogen) dissolved in the melt. It has been concluded that aerosol particles may be formed by condensation of melt vapor and mechanical breakup of the melt and that the extent of melt disruption influences the aerosol generation. It was also shown that the above stated phenomena are likely to occur in reactor accidents.

This report provides results from analytical and experimental investigations on the behavior of a gas supersaturated molten jet expelled from a pressurized vessel. Aero-hydrodynamic stability of liquid jets in gas, stream degassing of molten metals, and gas bubble nucleation in molten metals are relevant problems that are addressed in this work.

Models are developed for jet expansion, primary breakup of the jet, and secondary fragmentation of melt droplets resulting from violent effervescence of dissolved gas. The jet expansion model is based on a general relation for bubble growth, which includes both inertia-controlled and diffusion-controlled growth phases. The jet expansion model is able to predict the jet void fraction, jet radius as a function of axial distance from the pressure vessel, bubble size, and bubble pressure. The number density of gas bubbles in the melt, which is a basic parameter in the model, was determined experimentally and is about $10^8/m^3$ of liquid. The primary breakup of the jet produces a spray of droplets, about 2 to 3 mm in diameter.

Parametric calculations for a TMLB' reactor accident sequence show that the corium jet is disrupted within a few initial jet diameters from the reactor vessel and that the radius of corium spray at the level of the reactor cavity floor is in the range of 0.8 to 2.6 m.

Three possible mechanisms of secondary fragmentation have been investigated: acceleration induced fragmentation resulting from gas expansion when gas bubbles burst, fragmentation

due to droplet explosion, and fragmentation resulting from collapse of gas-inflated melt droplets. Predicted fragment sizes are in reasonably good agreement with experimental data.

Calculations of aerosol generation show that vaporization of iron may produce significant amounts of aerosol during pressurized melt ejection.

The average size of particles produced during the breakup of a corium jet is estimated using the concept of overall jet breakup efficiency. The Sauter mean diameter (D_{32}) and mass mean diameter are in the 75- to 630-μm and 220- to 1400-μm-size range, respectively, depending on initial conditions. In accordance with experimental results, the particle size distribution is lognormal with geometric standard deviation of about 3.5.

CONTENTS

CONTENTS (Continued)

CONTENTS (Concluded)

LIST OF FIGURES

LIST OF FIGURES (Concluded)

LIST OF TABLES

LIST OF TABLES (Concluded)

NOMENCLATURE

(All dimensional variables are in SI Units.)

Symbols

A	- jet cross-sectional area, constant, surface area, or parameter (Equation 188)
a	- chemical activity or interface acceleration
a_n	- distortion amplitude (Equation 186)
B	- constant
$\bar{B}_I, \bar{B}_K, \bar{B}_{IK}$	- dimensionless parameters
C	- concentration, integration constant, or velocity of sound
C_D	- droplet drag coefficient
D	- diffusion coefficient
D_o	- initial droplet diameter
d	- maximum stable droplet size or fragment size
E	- constant or energy
E_o	- activation energy for diffusion step
F	- Helmholtz free energy
f	- volume fraction
$f(D)$	- distribution function of fragment sizes
G	- mass flux
g	- gravitational acceleration
h	- distance, specific enthalphy, or thickness of the liquid shell (Figure 27)
i	- number of molecules in critical bubble
J	- nucleation rate
$\bar{J}a$	- dimensionless parameter or Jakob number for supersaturated liquid
K, K'	- equilibrium constants
k	- Boltzmann constant, effective surface-dilational viscosity, or wave number
M	- mass of gas in the bubble or total melt mass
m	- molecular mass or mass
N	- number density of nuclei

n - exponent, number of fragments, or disturbance growth rate parameter

n_o - molecular density

n^* - number density of critical bubbles

n_s - number of molecules absorbed at the bubble surface

On - Ohnesorge Number, $\frac{\mu}{(\rho\sigma D_o)^{1/2}}$

P - pressure

p - nondimensional jet radius

R - bubble radius

R - universal gas constant

R_g - gas constant

$\dot{R}$ - bubble wall velocity

$\ddot{R}$ - bubble wall acceleration

R^+ - dimensionless bubble radius

Re - Reynolds Number, $\frac{\rho VD}{\mu}$

r - radius

r - radial distance

s - Boltzmann transformation variable or specific entropy

T - temperature or dimensionless total breakup time

t - time

t^+ - dimensionless time

u - liquid velocity

V - volume, velocity, or free stream velocity (Equation 141)

v - velocity

W - work

We - Weber Number, $\frac{\rho V^2 D}{\sigma}$

x - parameter (Equation 191)

x_i - mass fraction of component i

Z - Zel'dovich nonquilibrium factor

z - axial distance

z_i - volume fraction of component i

α - void fraction, mass transfer coefficient, parameter (Equation 150), or accommodation coefficient

β - growth constant

γ - initial supersaturation or isentropic exponent

δ - diffusion boundary-layer thickness

ϵ - accuracy or $\frac{\rho_g}{\rho_\ell}$ (density ratio)

η - breakup efficiency or disturbance amplitude

θ - contact angle or half-angle of the jet spread

λ - disturbance wavelength

μ - chemical potential, dynamic viscosity, or parameter in lognormal distribution

ν - kinematic viscosity

ξ - dimensionless bubble radius

π - 3.14159

ρ - density

σ - surface tension or parameter in lognormal distribution

σ_g - geometric standard deviation

σ_o - electrostatic energy density

τ - time

τ_M - dimensionless time

Φ - normalized concentration driving force

$\Phi(\beta)$ - bubble growth function

Ψ - variable defined in Equation 31

Ω - molecular volume

ω - frequency of addition of a single molecule to unit area of critical bubble

Subscripts

a - ambient

b - bubble

c - critical

d - droplet

eq - equilibrium
f - liquid
g - gas
I - inertia
i - interface
j - jet
K - surface kinetics
l - liquid
N - nozzle
o - initial value
s - surface
s - saturation (equilibrium) value
∞ - value at large r or ambient

Superscripts

i - iteration parameter
+ - dimensionless
* - value at critical condition or fastest growing disturbance

Overscore

$\bar{}$ - average value
$\bar{\bar{}}$ - value at ambient conditions (corresponding to p_∞)

Brackets

[ ] - concentration

ACKNOWLEDGMENTS

First and foremost, the author expresses his sincere thanks to M. Pilch for his valuable advice, helpful discussions, and encouragement throughout the course of this work. Sincere thanks are also due to W. Tarbell, who was responsible for the experiments described in this document, and to D. Powers for their helpful advice and discussions. The author also thanks W. Camp for his useful comments and continued support.

1. INTRODUCTION

1.1 Background and Objective

In the event of certain postulated core meltdown accidents in light water reactors, part of the reactor fuel, fuel cladding, and internal structures will melt and slump into the lower plenum of the reactor pressure vessel (RPV). This material, if still molten, could be discharged from the RPV as a high velocity jet if an in-core instrumentation tube penetration fails and if the primary system pressure is significantly above containment pressure. Probabilistic Risk Assessment studies have concluded that pressurized water reactors (PWR) have a relatively high probability for a core meltdown accident.

The in-vessel phenomena of a severe accident are currently being studied through intensive research and computer modeling such as the MELPROG project.[1] In this study, we are mainly interested in the final stage of the in-vessel accident progression, namely vessel failure and melt transport from the RPV to the containment building. Our attention is limited to the PWR, which means that molten material, often called corium, will be released from the reactor vessel to the reactor cavity region.

The amount of melt, its composition, temperature, and content of dissolved gases, as well as the primary system pressure and temperature at the instant of vessel failure, are dependent on the prior events of the accident. The detailed analysis of the accident initiating events and various accident sequences is carried out in a probabilistic manner. Well-known examples of such studies are the WASH-1400 report[2] and Zion Probabilistic Safety Study (ZPSS).[3]

For our purpose, it is enough to note that in-vessel accident progression and vessel failure can occur under various pressures in the primary system, ranging between 0.1 MPa and full system pressure, i.e., about 17 MPa.

If the accident is initiated by a large break of one of the reactor cooling circuits, the primary system pressure will rapidly decrease and eventually come to equilibrium with containment pressure. However, if the accident is initiated by the small break or transient event, the primary system pressure may be above that of containment at the time of vessel melt through. How the accident is initiated needs to be known to determine how the corium will be relocated from the reactor vessel to the reactor cavity and the subsequent cavity phenomena.

We can distinguish between two modes of corium transport in this connection; so-called gravity drop when the primary system pressure is equal to the containment pressure, and

forceful melt ejection, schematically illustrated in Figure 1, when there is a substantial pressure difference between the reactor vessel and the containment building. The ZPSS found that in the 18 cases analyzed, all but one showed the vessel failure to occur through failure of the welds around the instrument tubes. In this case, the debris will be dispersed through the hole created by the instrument tube ejection. The failed in-core instrumentation tube will cause an initial vessel breach 4 cm in diameter. The size of this hole will, according to ZPSS, increase substantially d ring the period of melt discharge because of the ablation of the steel structure surrounding the breach. The final breach size is calculated to be approximately 40 cm.

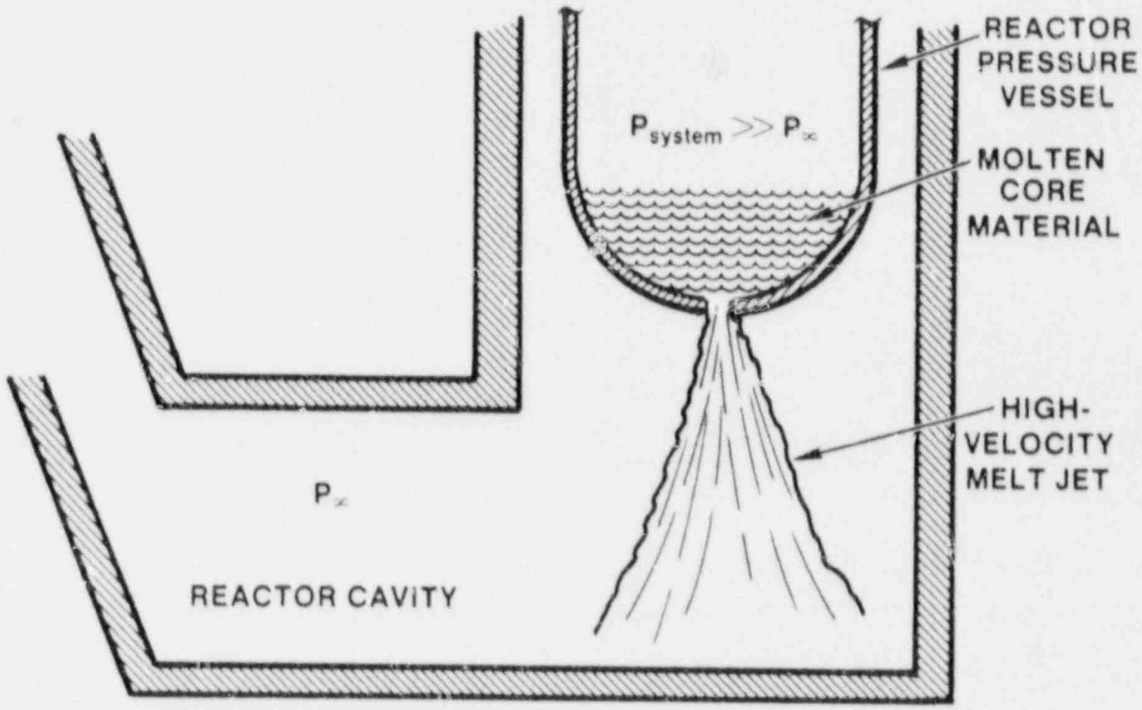

Figure 1. Schematic of Pressurized Melt Ejection in PWR

The ZPSS shows that the way in which debris enters the cavity region is of crucial importance for the accident progression in the containment building. It was predicted that ejection of molten core material while the primary system is pressurized, followed by the blowdown of steam and hydrogen, will cause the debris to enter into the containment region. This scenario was considered as favorable regarding containment integrity because debris dispersed over a large area of the

containment floor would be easily quenched. On the contrary, the effective quenching of debris in the cavity could be difficult, thus leading to the possibility of concrete erosion and hydrogen generation.

The ZPSS does not give a detailed description of the configuration of the jet stream emanating from the breach in the reactor pressure vessel. The analysis predicts that the jet will be composed entirely of liquid core material with a diameter equivalent to the breach dimension. Additionally, the stream does not expand from the point of discharge until contact with the cavity floor.

The ZPSS investigation concerning melt ejection from the pressurized primary system and behavior of high-temperature materials in confined geometries was mainly analytical and experimental confirmation was desired. To provide this, two experimental programs were undertaken; small-scale experiments at the Argonne National Laboratories[4] and large-scale experiments at Sandia National Laboratories (SNL).[5] Results of both the Argonne and SNL experiments indicate that, indeed, the debris can be removed from the reactor cavity into the containment building in the case of melt ejection from the pressurized primary system.

The experimental program at Sandia, called the High-Pressure Melt Streaming (HIPS) program, was initiated by the small-scale experiments (SPIT tests) to study high-velocity jets, jet-water interactions, and 1/20th scale cavity geometries.[5] The results from the Phase I SPIT tests have shown that the ejected melt is not a coherent, stable stream. These results have been recently confirmed by the JETA-B jet characterization tests.

Two important observations have been made:

1. Expansion and breakup of the ejected molten jet occurs.

2. Significant aerosol generation accompanies the ejection process.

The expansion and breakup of the jet in the experiments are attributed to rapid evolution of the pressurizing gases (nitrogen in SPIT tests and hydrogen in JETA-B tests) dissolved in the melt.

It was also concluded that aerosol particles may be formed by condensation of melt vapor and mechanical breakup of the melt and that the extent of melt disruption influences the aerosol generation. These observations and conclusions, if applicable to a reactor accident, would draw attention to new and important aspects of cavity and containment phenomena not

considered in previous safety studies. The disruption of a corium jet could affect (1) aerosol generation and through this the source term, (2) concrete erosion in the cavity region, (3) molten fuel-coolant interactions if water is present in the cavity, (4) removal of core debris from the cavity region, and (5) direct containment heating.

Figures 2 and 3 show flash X-ray photographs of the melt stream taken during two SPIT tests. The experiments were conducted at the same conditions except for the type of gas. The SPIT-8 test was charged with nitrogen, while carbon dioxide was used in SPIT-12 test. Solubility of carbon dioxide in liquid iron is low compared to that of nitrogen in liquid iron.

Table 1 shows the values of nitrogen solubility in molten iron for conditions typical for SPIT tests. Nitrogen concentration is expressed in units of percent nitrogen by weight.

For SPIT-8 test conditions (i.e., temperature approximately 2800 K and pressure 7.5 MPa) the amount of dissolved nitrogen is 367 cm^3 at STP per 100 g of iron. Considering that 100 g of iron will occupy about 14.3 cm^3, it shows the great potential for disruption of the jet by nitrogen evolution from the melt.

On the X-ray photograph of N_2-driven jet (Figure 2), the expansion of the jet (half-angle about 10°) and voids within the stream are visible. The photo from SPIT-12 test (Figure 3) shows the appearance of a CO_2-driven jet. In this case, the jet appears as a nearly coherent stream with ligament-type instabilities emanating from the surface. No large voids or lower-density areas are obvious within the stream, as would be expected without gas in the solution.

The crucial question is whether or not the expansion and breakup of the molten jet by the violent evolution of dissolved gas are typical for a reactor accident. The pressurizing gases in the reactor case are principally water vapor and hydrogen. It is estimated that the solubilities of these two gases in molten corium are of the same order as the solubility of nitrogen in iron.

Table 2 gives the solubility of hydrogen in molten iron, and Table 3 the estimated solubility of hydrogen and water vapor in oxidic melt.

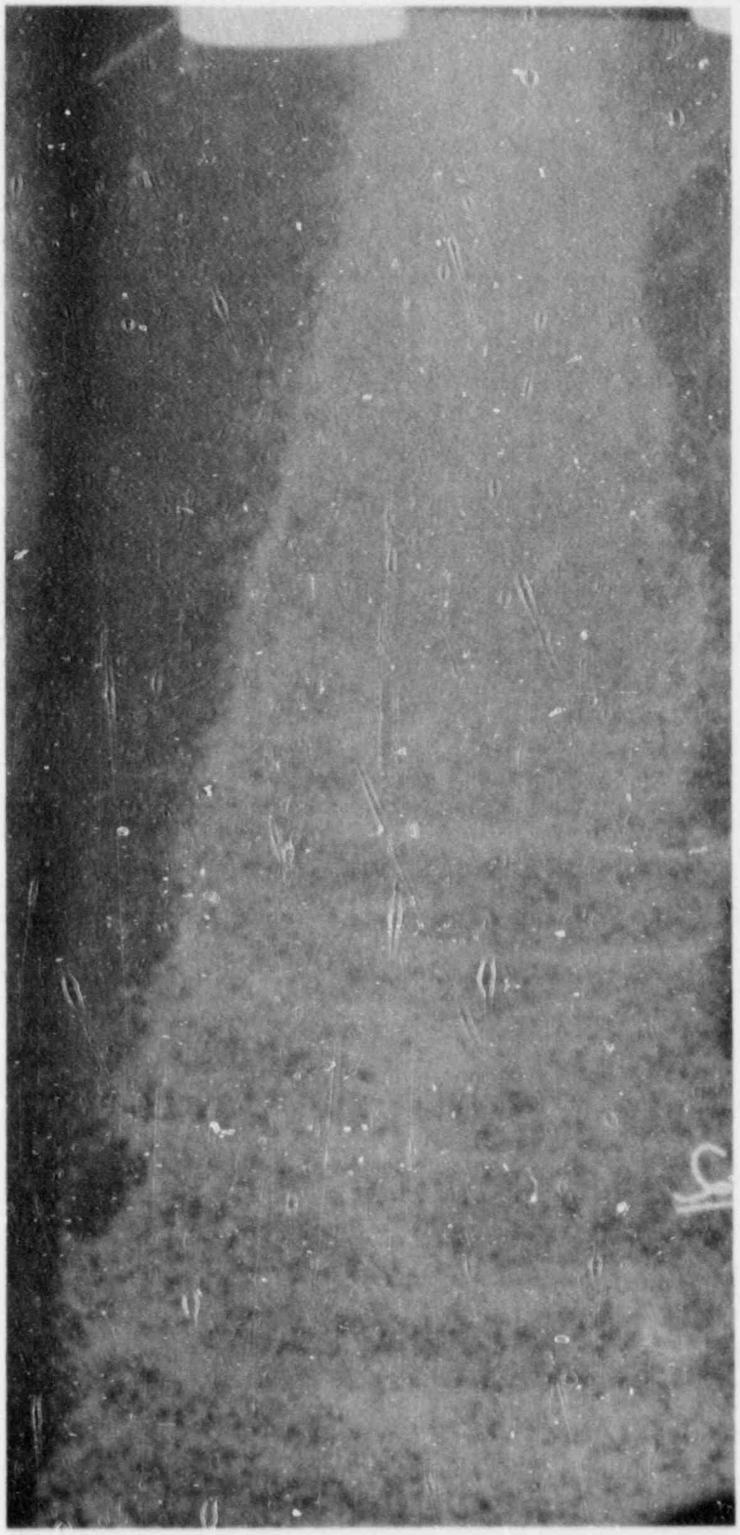

Figure 2. Flash X-Ray Photograph of N_2-Driven Melt Jet Taken 30 ms After Start of Melt Ejection

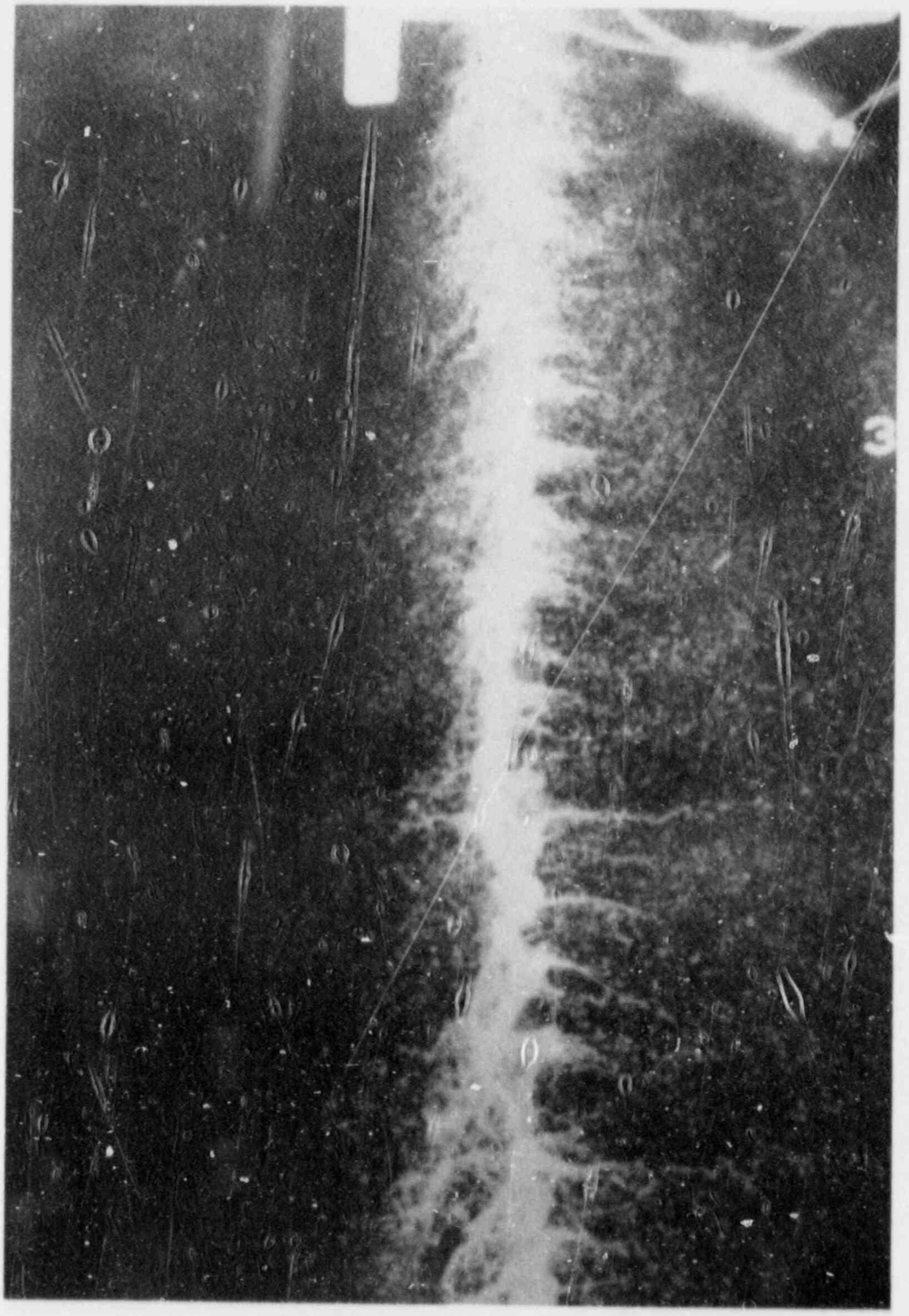

Figure 3. Flash X-Ray Photograph of CO_2-Driven Melt Jet Taken 30 ms After Start of Melt Ejection

Table 1
(From Powers[6])

Estimated Nitrogen Solubility in Molten Iron

Temperature (K)	Pressure (atms)	N %	N_2 (cm^3(STP)/100 g Fe)
1810	150	0.547	477
1810	75	0.387	338
1810	41	0.286	250
1810	0.65[a]	0.036	31.4
2800	150	0.596	520
2800	75	0.421	367
2800	41	0.311	271
2800	0.65[a]	0.039	34

[a]Partial pressure of N_2 in air at one Albuquerque atmosphere.

Comparing values from Tables 1 and 2, we can see that hydrogen solubility in the molten iron at a range of conditions representative of a reactor accident is of the same order as nitrogen solubility in the SPIT tests. Therefore, in a postulated reactor accident, the behavior of the corium jet caused by gas evolution would be expected to be similar to melt behavior in experiments using nitrogen.

As a result of the information and insights gained from the SPIT experiments and from theoretical considerations, an analytical and experimental effort was undertaken aimed at the development and validation of a model describing the behavior of a gas-supersaturated liquid jet expelled from a pressurized vessel.

It was also realized that an understanding of physiochemical processes responsible for jet behavior in high pressure melt ejection is necessary for a meaningful interpretation of experimental results and their extrapolation to reactor accident situations.

1.2 Applicability

The nature of the jet emanating from the reactor vessel will have a direct influence on the subsequent behavior of the melt within the cavity.

As stated in the preceding section, the configuration of a corium jet entering the reactor cavity region could affect the following phenomena:

Table 2
(From Powers[6])

Dissolved Hydrogen in Molten Iron

Temperature (K)	P_{H_2} (MPa)	$[H_2]$ cm^3(STP)/100 g Fe	$[H_2]$ cm^3(STP)/cm^3 Fe
1810	15.0	383	26.8
	7.5	271	19.0
	4.1	200	14.0
	0.1	31	2.2
2800	15.0	800	55.9
	7.5	565	39.5
	4.1	418	29.2
	0.1	65	4.5

Table 3

Solubility of H_2 and H_2O in an Oxidic Melt

Temperature (K)	P_{H_2} (MPa)	P_{H_2O} (MPa)	Concentration H_2 (1 STP/1 of oxide)	Concentration H_2O (1 STP/1 of oxide)
2800	7.5	7.5	3.27	0.59
	1.5	13.5	0.65	1.06
	0.2	14.8	0.07	1.17
1800	7.5	7.5	3.11	0.22
	1.5	13.5	0.62	0.39
	0.2	14.8	0.06	0.43

1. Aerosol generation

2. Concrete erosion in the cavity region

3. Molten fuel-coolant interactions

4. Removal of core debris from the cavity region

5. Direct containment heating

- Aerosol generation

The implication of aerosol generation for accident progression and consequences is quite obvious and will not be discussed here.

- Concrete erosion in the cavity region

The concrete erosion refers to the thermal decomposition caused by contact with high-temperature jet. According to Reference 5, "the rate and extent of erosion in the HIPS tests are important aspects of the ex-vessel debris behavior. Concrete erosion may influence the development and magnitude of the key hydrodynamic processes being studied in the tests." It was shown that the rate of concrete erosion will be proportional to the imposed heat flux, which in turn depends on stream diameter, d, as $d^{1/2}$.

Parametric study of jet expansion for the TMLB' sequence, presented in Section 2.7, shows that the diameter of the fragmented jet at the level of the reactor cavity floor may be 40 to 130 times the breach diameter. In this case, the concrete erosion rate would probably be reduced by several orders of magnitude.

- Molten fuel-coolant interactions

A molten fuel-coolant interaction of an explosive character, known as a steam or vapor explosion, is an important issue in connection with postulated core meltdown accidents.[2,3,7] The ZPSS postulates that a steam explosion will occur when the melt stream exits the reactor pressure vessel, penetrates the water pool, and contacts the cavity floor. The molten fuel-coolant interaction may displace the water and a portion of the debris from the cavity region.

It is possible to distinguish four phases of an effective vapor explosion. They are:

1. Coarse premixing of fuel and coolant

2. Triggering

3. Fragmentation and propagation

4. Expansion

It is very difficult to assess which, and to what extent, each of these four phases will be affected by a particular jet configuration. However, it is likely that phases one and three are strongly dependent on the melt configuration before water contact. An extensive fragmentation and dispersion of molten jet before water contact would probably make a large-scale coherent explosion difficult for the following reasons:

1. Separation of corium particles.

2. Solidification and crust formation on the surface of fuel particles that could hinder the direct liquid-liquid contact, which is a necessary condition for triggering an explosion.

3. Crust formation, which also can prevent hydrodynamic fragmentation.

4. Gas evolution from the melt, which can shield it from the water.

Another phenomenon that should be considered in this context is hydrogen generation from fuel-water contact. The hydrogen is produced by the chemical reaction between steam and metallic components of the fuel; Zr or Fe. The blanket of hydrogen surrounding the fuel particle has a hindering effect on the explosion.[8]

It has been observed[9] that no large-scale explosions occurred when a stream of molten aluminum was broken while poured into water. A recent uncertainty study of PWR steam explosions[10] has found that among the most important uncertainties is the jet pour diameter. The study was concerned only with consequences of in-vessel steam explosions, but this result should also apply to ex-vessel steam explosions.

- Removal of core debris from the cavity region

According to Reference 5, "the average pressure exerted by the jet on the concrete floor provides the driving force that induces the radial movement of the debris and subsequent splashout" and that "this pressure is inversely related to the area of the jet." Thus the jet expansion and breakup would alter the conditions for debris removal from the cavity region.

- Direct containment heating

  Direct containment heating refers to the situation in which fragmented core debris is ejected from the cavity region into the main containment volume. If the melt droplets are small the rapid liberation of thermal and chemical energy (oxidation of the metallic constituents of the corium) can directly heat and consequently pressurize the containment. Disruption of the corium jet is, however, only one of the mechanisms which will affect the direct containment heating problem.

1.3 Approach

The problem breaks up naturally into the following four tasks:

1. Aero-hydrodynamic stability of the molten jet.
2. Jet behavior due to evolution of dissolved gases.
3. Comparison of model predictions with experimental observations.
4. Model predictions for reactor accidents.

A thorough investigation of jet behavior due to evolution of dissolved gases should include analysis of the following phenomena:

1. Nucleation of gas bubbles
2. Bubble dynamics
3. Jet expansion due to growth of gas bubbles
4. Jet breakup and fragmentation

This report consists of four major sections: Section 1 is this introduction; Section 2 addresses jet expansion and primary breakup; Section 3 addresses secondary fragmentation of melt droplets, the resulting particle size distribution, and aerosol generation; and Section 4 is the summary and conclusions.

Aero-hydrodynamic stability of a liquid jet in gas is discussed in Section 2.1. Time-scales for jet breakup by the aero-hydrodynamic forces in experimental and reactor accident situations are presented.

A review of relevant literature on jet disruption due to dissolved gases is presented in Section 2.2. It is shown that stream degassing of liquid steel has much in common with our problem.

An important and difficult issue is nucleation of gas bubbles in a liquid metal. Nucleation theory and its application to experimental and reactor accident situations are addressed in Section 2.3.

The jet expansion model is developed in Section 2.4. Dynamic of gas bubble growth in supersaturated liquid plays a major role in this model. An appropriate mode of gas bubble growth is developed in Section 2.5.

Experimental results from relevant SPIT and JETA-B tests and analyses using the jet expansion model are presented in Section 2.6. Number density of gas bubbles in the molten jet, which is a basic parameter, is determined.

In Section 2.7 parametric calculations for a high pressure reactor accident scenario are presented.

Section 3.1 presents three models of secondary fragmentation of melt droplets. The models are (1) acceleration induced fragmentation resulting from gas expansion, (2) fragmentation due to droplet explosion, and (3) fragmentation resulting from droplet inflation followed by collapse of the liquid layer.

The size distribution of the debris collected from the JETA-B tests is described and characterized in Section 3.2.

Aerosol generation by condensation of iron vapor and film fragmentation when gas bubbles burst is addressed in Section 3.3.

Section 3.4 shows how the mean diameter of corium particles generated by jet fragmentation can be estimated from the concept of overall efficiency of jet breakup process.

2. JET EXPANSION AND PRIMARY BREAKUP

2.1 Liquid Jet Stability in Gas

2.1.1 Introduction

Results of SPIT and JETA-B tests indicate that effervescence of dissolved gas is responsible for jet expansion and fragmentation. Before we will attempt to develop models of these processes it is necessary, however, to investigate stability of a high-velocity liquid jet in gas in order to compare time-scales for jet breakup by the aero-hydrodynamic forces and gas effervescence.

Stability and breakup of liquid jets have been the subject of extensive experimental and theoretical studies due to the importance of jet disintegration phenomena in technological applications, such as atomizers, internal combustion engines, and fire fighting equipment. Several literature reviews have been published on the subject, e.g., Schweitzer[11] and Reitz.[12] Most recently Pilch[13] and Ginsberg[14] have addressed the jet stability problem. In this section we will restrict ourselves to brief investigation of jet breakup length and size of the fragments produced by jet breakup. Predictions for experiments and reactor accident are presented.

2.1.2 Breakup Regimes

Jet breakup data are usually correlated with Weber Number (We), Reynolds Number (Re) and Ohnesorge Number (On).

Weber number is the ratio of the inertia force to the force of surface tension:

$$We = \frac{\rho V^2 D}{\sigma} \quad . \tag{1}$$

Here ρ is the density of the jet or the flow field surrounding the jet, V is the relative velocity between the gas and the jet, D is the jet diameter, and σ is the surface tension.

The Weber number may be based on either the gas density, and then is called ambient Weber number (We_a), or on the jet density, and then is called jet Weber number (We_j):

$$We_a = \frac{\rho_a V^2 D}{\sigma} \quad , \tag{2}$$

$$We_j = \frac{\rho_j V^2 D}{\sigma} \quad . \tag{3}$$

Here a and j refer to the ambient gas and jet, respectively.

The Reynolds number (Re), which is the ratio of the inertia force to the friction force, is defined as

$$Re_j = \frac{\rho_j V D}{\mu_j} \quad . \tag{4}$$

Here μ_j is the dynamic viscosity of the jet.

The Ohnesorge number (On), which expresses the viscous effects is defined as

$$On = \frac{\mu}{\left(\rho_j \sigma D\right)^{1/2}} \quad . \tag{5}$$

The Weber number, Reynolds number, and Ohnesorge number are related:

$$On = \frac{\left(We_j\right)^{1/2}}{Re_j} \quad . \tag{6}$$

Four breakup regimes are usually identified;[12,14] they are schematically illustrated in Figure 4. The regimes are:

1. Rayleigh Breakup

   In this regime, first treated by Rayleigh,[15] the breakup is caused by the growth of an axisymmetric disturbance due to capillary force. The effect of ambient atmosphere is negligible. Jet velocity is low and the size of the droplets is on the order of jet diameter.

   It is assumed that Rayleigh breakup occurs when $We_a < 0.4$.

   The breakup length, i.e., coherent portion of the jet, is given by

$$\frac{Z}{D} = C\left(We_j^{1/2} + 3\,\frac{We_j}{Re_j}\right) \quad , \tag{7}$$

or

$$\frac{Z}{D} = CWe^{1/2}\,(1+3\,On) \quad , \tag{8}$$

where the constant C is approximately 12.

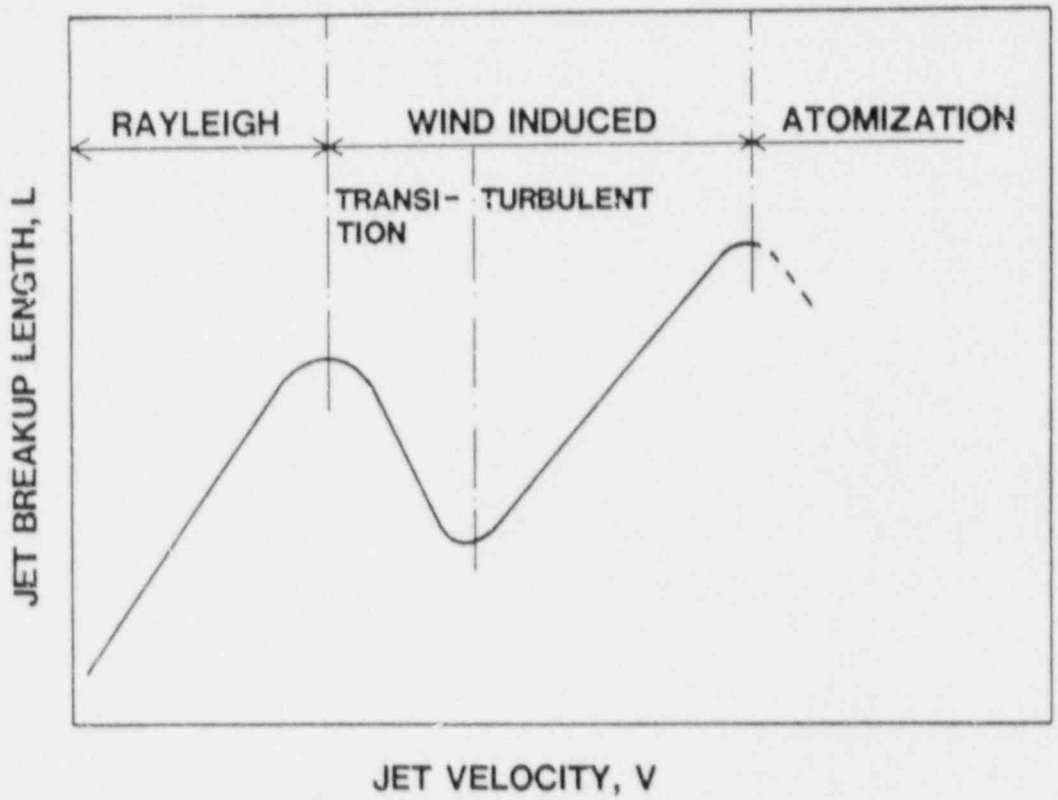

Figure 4. Schematic Description of Jet Breakup Regimes

2. Wind Induced Breakup (long wavelength waves)

3. Wind Induced Breakup (short wavelength waves)

These two regimes can be viewed as a transition region between the Rayleigh and the Atomization regimes. The action of ambient atmosphere becomes more and more important for jet stability. Also nozzle geometry and jet Reynolds Number play a role in jet behavior.

It is assumed that the jet is in Regimes 2 and 3 if

$$0.4 < We_a < 50\text{-}300 \quad .$$

According to Reitz[12] the transition between Rayleigh and Wind Induced Breakup occurs when

$$We_a = 1.2 + 3.41\ On^{0.9} \quad . \tag{9}$$

The breakup length in Regime 2 is not well defined. In Regime 3, which is sometimes called Turbulent Jet Regime, the breakup length is given by Grant and Middleman:[16]

$$\frac{Z}{D} = 8.51\left(We_j\right)^{0.32} \quad . \tag{10}$$

This formula seems to give reasonable results for We_j numbers of up to about 200.

No correlations for the size of fragments generated in Regimes 2 and 3 were found. The drop size seems to be in the range from jet diameter to much smaller, but still relatively coarse fragments.

4. Atomization Breakup

In this regime, a large number of small droplets are formed and the disintegrated jet resembles a spray. According to Levich[17] the jet is broken up into a few relatively large droplets which subsequently are atomized in a cloud of small droplets by the dynamic effect of surrounding medium. Most data and observations in Atomization Regime is for high-velocity, small-diameter jets.

The criteria for transition between the Wind Induced, Turbulent Regime, and Atomization Regime is not clear. As stated above, the reported ambient Weber number is in the range 50 to 300, thus indicating large uncertainty.

The intact length of the low viscosity (i.e., small On number) jet was calculated by Levich[17] and is given by

$$\frac{Z}{D} \approx \left(\frac{\rho_j}{\rho_a}\right)^{1/2} \quad . \tag{11}$$

We observe that the breakup length is independent of the jet velocity.

Levich[17] also estimated the size of droplets separated from the jet surface. The size is given by the length of the unstable wave.

For short waves:

$$d \sim \frac{\sigma}{\rho_g V^2} \quad . \tag{12}$$

For long waves:

$$d \sim 8D \quad . \tag{13}$$

Droplets produced by primary jet breakup may be subject to secondary breakup by the action of aerodynamic forces. The maximum stable fragment size in this case was given by Pilch:[18]

$$\frac{d}{D_o} = \frac{12}{We_a} \left[1 - 8.94\left(\frac{\rho_g}{\rho_j}\right)^{1/2}\right]^{-2} \quad , \tag{14}$$

where D_o is the initial drop diameter.

It is necessary to emphasize that the above correlations and data apply strictly speaking only to small diameter jets and nozzles with large length-to-diameter (L/D) ratio so that flow is turbulent. There is strong experimental evidence[13,19] that jets emanating from orifice or nozzle with small L/D ratio (<5) are much more stable.

2.1.3 Application to Experiments and Reactor Cases

The parameters pertinent to the experimental (SPIT and JETA-B tests) and reactor conditions are listed in Tables 4 and 5 for three system pressures and in the reactor case also for

Table 4

Jet Breakup Parameters Pertinent to SPIT and JETA-B Experiments

Δp [MPa]	V_j [m/s]	D [m]	L/D	Re_j	We_j	We_a	On
1	23	0.0254	1	7.5×10^5	5.2×10^4	13	3.0×10^{-4}
7	60	0.0254	1	1.9×10^6	3.5×10^5	91	3.0×10^{-4}
16	91	0.0254	1	3.0×10^6	8.0×10^5	210	3.0×10^{-4}

Table 5

Jet Breakup Parameters Pertinent to Reactor Cases

Δp [MPa]	V_j [m/s]	D [m]	L/D	Re_j	We_j	We_a	On
1	15.8	0.04	3.5	1.7×10^6	1.6×10^5	20	3.2×10^{-4}
7	41.8	0.04	3.5	3.3×10^6	1.1×10^6	140	3.2×10^{-4}
16	63.2	0.04	3.5	5.0×10^6	2.6×10^6	320	3.2×10^{-4}
1	15.8	0.40	0.35	1.7×10^7	1.6×10^6	200	3.2×10^{-4}
7	41.8	0.40	0.35	3.3×10^7	1.1×10^7	1400	3.2×10^{-4}
16	63.2	0.40	0.35	5.0×10^7	2.6×10^7	3200	3.2×10^{-4}

two jet diameters. The smaller diameter (4 cm) corresponds to the initial size of the reactor vessel breach at the time of vessel meltthrough and the larger diameter (40 cm) corresponds to the final breach size, enlarged by the ablation process.

The following material properties data were used:

Experiments: Fe/Al_2O_3 melt:

$\rho = 3843$ kg/m^3
$\sigma = 1$ N/m
$\mu = 3 \times 10^{-3}$ Pa•s

Reactor case: Corium (67.2 w/o UO_2, 16.4 w/o Fe, 8.2 w/o Zr, 8.2 w/o ZrO_2):

$\rho = 8000$ kg/m^3
$\sigma = 0.5$ N/m
$\mu = 4 \times 10^{-3}$ Pa•s

Tables 4 and 5 show that with exception of experimental jet at 1 MPa pressure and reactor case jet at 1 MPa pressure and D = 0.04 all jets are in the atomization regime according to ambient Weber number criteria.

The breakup lengths calculated according to the Levich formula are:

Experiments:

$$\frac{Z}{D} \approx \left(\frac{\rho_j}{\rho_a}\right)^{1/2} = 62 \quad ,$$

thus $Z \sim 1.5$ m .

Breakup time is given by

$$\tau = \frac{Z}{V_j} \quad , \tag{15}$$

and we have

$\tau \sim 17$ ms - 65 ms .

Reactor case:

$$\frac{Z}{D} \approx \left(\frac{\rho_j}{\rho_a}\right)^{1/2} = 89 \quad ,$$

thus $Z \sim 3.6\ m - 36\ m$

and for breakup time we get

$$\tau \sim 57\ ms - 2\ s \quad .$$

The size of the fragments produced by various hydrodynamic breakup processes is on the order of 1 to 20 mm (see Section 3.1.1).

2.1.4 Conclusions

Even if calculated breakup lengths and breakup times are only estimates it is quite evident that jet breakup and fragmentation observed in SPIT and JETA-B tests cannot be explained in terms of aero-hydrodynamic jet theory. X-ray photographs of melt jets of the SPIT 8, JETA-B2, and JETA-B3 tests clearly show that jets uniformly expand and are disrupted in a few milliseconds or within less than 10 jet diameters. These times and distances are much smaller than those calculated above and the difference would be even larger for jets emanating from orifice or nozzle with small length-to-diameter ratio, as in the experiments and reactor cases. Moreover, experiments show[14] that the breakup length in the Atomization Regime is greater by a factor of 3 to 16 than the breakup length given by Equation 11.

2.2 Review of Relevant Literature

2.2.1 Introduction

The problem of breakup of gas-supersaturated liquid metal stream has been studied, to some extent, in connection with stream degassing of steel. Stream degassing is one of the methods employed in the steel industry for removal of impurities dissolved in liquid steel, mainly gaseous, such as hydrogen, oxygen, and nitrogen.[20,21,22] This particular method belongs to a broad class of so-called vacuum degassing processes[22,23] in which molten metal is exposed to a low pressure in vacuum chamber.

The mechanism of removal is by transport of solute from a liquid phase to a gas phase, and therefore the rate of the process is, in general, a function of total interfacial area and a driving force for the mass transfer, which is the difference between gas concentration in a liquid and gas space. The most effective degassing is achieved when a significant bubble nucleation takes place in the bulk of a liquid, in that way increasing the gas-liquid surface and stirring the melt.

In stream degassing a stream of steel is discharged into a vacuum chamber. The behavior of the stream depends on a nucleation rate and rate of gas bubble growth. These, in turn, are functions of vacuum chamber pressure, gas supersaturation, and nozzle design. To obtain effective degassing it is necessary that the stream of molten metal breaks up into a spray of droplets, because the main part of degassing takes place from the droplets. Sometimes the evolution of dissolved gases is so vigorous that the molten stream is disrupted in an explosive manner.

2.2.2 Stream Degassing of Steel

As mentioned above, transport of gas from liquid to gas phase across the interface is one of the factors which controls the rate of the gas removal. The kinetic aspects of the process are reviewed and discussed by Bradshaw,[24] Bradshaw and Richardson,[25] Bogdandy[26] and Winkler.[27] The role of interfacial phenomena in this connection is discussed by Richardson.[28] According to Bradshaw, three steps can be distinguished in the transfer of gas from one phase to another, namely:

1. Transfer of the species to the interface from the bulk of the liquid
2. Transfer across the interface
3. Transfer from the interface to the bulk gas

Step 2 can be subdivided into:

a. Adsorption at the interface

b. Reaction at the interface

c. Desorption from the interface

The rate of mass transfer can be controlled by one or more of these steps and the problem is very complex. For example, as discussed by Richardson,[28] nonreacting surface active solutes may significantly affect interfacial phenomena under certain circumstances. Rosner and Epstein[29] consider the effect of chemical kinetics on the growth of nitrogen bubble in liquid iron. Robertson and Ogunleye[30] concluded in their study of stream degassing of molten iron that chemical kinetics was a controlling factor in the growth of nitrogen bubbles. The systematic investigation of what influence interfacial phenomena may have on the dynamics of bubble growth is beyond the scope of the current work. Such an investigation would probably be difficult considering that experimental data for liquid metals seem to be sparse and the involved mechanisms are not fully understood.

However, according to Szekely and Themelis[31] the diffusion in the liquid is a rate-controlling factor in many bubble-liquid systems of interest to metallurgists. Moreover, according to Bradshaw,[24] the major resistance in the removal of hydrogen from steel lies in the liquid phase.

Next, we shall account for the observations and results from stream degassing of liquid metals.

According to Belk[22] the liquid metal breaks up during stream degassing into a stream of droplets, thus giving a very effective degassing. The stream expands due to the gas evolution and breaks up into droplets with diameters between 10 and 10^{-3} mm.

Sharp[20] discusses removal of hydrogen and oxygen from droplets. No information is given regarding the mechanism of droplet formation, which probably occurs mainly just outside the nozzle. High-speed photography reveals that the bubbles form within the droplets and that very small liquid droplets are produced when these bubbles collapse. According to the author, the bubble collapses due to the cooling of the steel film. The bubble size is primarily controlled by the type of nozzle, the pressure in the chamber, and the surface tension of the steel. It is reported that "stream degassing offers an extremely rapid method of hydrogen removal."

An experimental study of stream breakup of molten steel and silver containing dissolved oxygen has been performed by Warner.[32] The author also proposed a kinetic model for the primary mechanism of the stream breakup. Experiments with molten steel were carried out initially with the nitrogen-melted charge and no breakup of the jet was observed. In subsequent experiments, the gas content of the melt was increased by bubbling a CO/CO_2 gas mixture through the melt and explosive disintegration of the steel jet was observed. Because of difficulties in handling molten steel, the steel was replaced by silver.

Some relevant observations made by Warner during his experiments are:

1. Jet disintegration was greater when more gas was dissolved in the melt, as expected.

2. The extent of breakup of oxygen-saturated silver (at 1 atm and 1100°C) is larger when discharged through a parallel-sided orifice compared with discharge through a sharp-edged orifice.

3. Maximum jet disintegration did not occur at the highest vacuum.

4. After the main stream disintegrated, secondary explosions were observed.

The author has discussed the possible mechanisms for bubble nucleation and growth. Homogeneous nucleation was ruled out because of low equilibrium pressure of CO. Then Warner considered four different possible initial sites of bubble growth. It was concluded that the initial sites for bubble growth in the main stream are small bubbles at vacuum chamber pressure entrained in the nozzle.

In concluding the review of Warner's article, we would like to note that in the introduction to his article the author emphasizes that according to practical observation made during stream degassing of steel, the molten metal is erupting violently as it enters vacuum chamber due to the rapid evolution of gas bubbles.

Olsson and Turkdogan[21] have investigated the expansion and breakup of streams of oil, mercury, and liquid steel by injection of argon gas bubbles into the liquid stream before it passes through a nozzle. Very fine sprays were produced due to the rapid expansion of these bubbles in the low pressure chamber. The authors have analyzed the mechanism of stream breakup by expansion of entrained argon bubbles. Based on the stream velocity, the angle of spread of the spray, and estimated (from photographs) droplet size, the bubble pressure before bursting was calculated.

The authors concluded that, according to what is generally believed, the breakup of the steel stream during degassing is a result of evolution and expansion of dissolved gases. It was also stated that the bubble nucleation in the free stream is not likely due to the high surface tension of molten steel and that the gas bubbles must be present in the stream as it leaves the nozzle.

The experimental and theoretical study of flow conditions during the degassing process have been performed by Mizoguchi, Robertson, and Bradshaw.[33] The authors have studied the behavior of molten silver streams saturated with oxygen at 0.2 and 1 atm, or degassed, and discharged into a tank at pressures between 500 and 2 mm Hg absolute through 4.75 and 2.38 mm nozzles. The streams of silver saturated with 1 atm oxygen behaved differently depending on pressure in the tank. At high pressure the stream behaved like degassed silver, i.e., no expansion, contraction, or breakup was observed. At a lower pressure the stream had a foamy appearance. When tank pressure was further decreased the stream diameter just outside the nozzle was appreciably

greater than the nozzle diameter, and at the very low pressure (10 Torr) the stream was completely disrupted.

These observations were interpreted in terms of the homogeneous, two-phase compressible flow in the bubbly regime and it was postulated that gas bubbles probably nucleated on the nozzle walls. Below certain tank pressures no increase in mass flux was observed when backpressure was reduced, i.e., critical conditions at the nozzle exit were reached (choked flow). The critical exit nozzle pressure and void fraction were calculated according to the theory of compressible two-phase flow. The theoretical predictions are reported to agree with experimental observations. It should be pointed out that the authors have not discussed the postulated bubble nucleation mechanism.

Mizoguchi, Robertson, and Bradshaw[34,35] have continued their study of behavior of oxygen supersaturated molten silver under stream degassing conditions. In Reference 34, the measurements of pressure at the nozzle exit for the choked two-phase flow, described in Reference 33, are reported. The authors have ensured that the previous observations were confirmed by pressure measurements, i.e., that the pressures at the nozzle exit were much higher than that of downstream in the tank and agreed with theoretical prediction.

In Reference 35, the authors have analyzed the bubble growth outside the nozzle for the same experiments as reported in References 33 and 34. A simple jet expansion model was proposed based on the two basic assumptions that bubble growth is diffusion controlled and that bubble nucleation occurs in the nozzle at a constant rate. Comparing the observed stream expansion with model predictions, the authors were able to confirm both mentioned assumptions and also calculate the nucleation rate. The rate of nucleation was on the order of 3000 bubbles per second (corresponding to about 10^8 bubbles per m^3 of liquid).

The calculated nucleation rate was higher at the lower supersaturation (i.e., for experiments at higher tank pressure), which is contrary to what one would intuitively expect. The authors were not able to explain this fact, but speculated that the bubble growth constant, on which calculations were based, could be affected by bubble interaction and that this interaction was more likely to occur at the lower tank pressure.

The inertial effect on bubble growth was found to be small in these experiments 2 cm from the nozzle exit. However, it was pointed out that inertial forces could contribute to growth retardation in the earlier stages of growth.

Robertson and Ogunleye[30] have investigated the behavior of molten iron saturated at 1 atm pressure with nitrogen, hydrogen, and carbon monoxide and discharged into a vacuum chamber through various nozzles with different L/D ratios and surface roughnesses. The nozzles were 2 mm in diameter and 2 to 10 mm long. The streams were observed using high-speed photography.

The nitrogen-saturated streams exhibited little breakup, contrary to hydrogen- and CO-saturated streams, which were vigorously disrupted. As in Reference 35, it was postulated that the bubbles were nucleated on the nozzle wall and the stream was interpreted in terms of two-phase bubble flow in the nozzle.

The extent of stream breakup has altered with nozzle type. For short-smooth nozzles little or no stream breakup was observed for nitrogen and hydrogen-saturated streams. The situation was much different for long-rough nozzles where there was extensive breakup of hydrogen-saturated streams but mainly "Rayleigh-type" breakup (due to capillary forces) of nitrogen-saturated streams.

It is interesting to note that when jet breakup was vigorous the fragmentation was extensive, since about 60 percent of the charge was found in the form of powder. It was concluded that growth of the nitrogen bubbles was controlled by chemical kinetics and that inertial effects were important. Growth of the hydrogen bubbles was very rapid with a lifetime of about 1 msec. The fragmentation of the hydrogen-saturated jet was very extensive in the rough nozzle; up to 80 percent of the discharged material was collected as a powder with 50 percent passing 250 μm. Finally, the authors reported that surface tension forces were important in the case of nitrogen bubbles.

In the opinion of the present author, it is not clearly and convincingly explained how important are the inertial and surface tension forces and also their connection with the growth controlled by chemical kinetics.

A short discussion concerning the hypothesized bubble nucleation on the nozzle wall is given by Ogunleye.[36] The author, after short presentation of work reported in Reference 30, is asking why nitrogen-saturated iron streams did not break up even in long-rough nozzles and at the very low tank pressure, especially considering that nitrogen has a more pronounced effect in lowering the surface tension of molten iron. It is suggested that heterogeneous nucleation at gas-filled crevices on the nozzle wall is easier in the hydrogen case due to its significantly higher diffusivity, (150×10^{-5} cm^2/s for hydrogen and 6 to 8×10^{-5} cm^2/s) for nitrogen.

Ogunleye[36] also reports that experiments with Fe-N-S and Fe-C-O, i.e., with surface active species that reduce surface tension, have not necessarily resulted in vigorous stream breakup.

2.2.3 Summary

We can summarize the insights gained from literature review as follows.

1. There is very convincing industrial and experimental evidence that a gas-supersaturated stream of molten iron can be disintegrated by the rapid evolution and expansion of the dissolved gas.

2. The gas evolution occurs in two steps; nucleation of gas bubbles and their subsequent growth.

3. Breakup of the hydrogen-supersaturated stream can be very vigorous and even of the explosive character. Breakup of the nitrogen-supersaturated stream is less vigorous.

4. In cases where breakup of the hydrogen-supersaturated stream is vigorous, more than 50 percent of the metal charge undergoes fragmentation to a sub-mm size.

5. After disintegration of the main stream, secondary fragmentation of liquid particles is possible.

6. Nucleation of gas bubbles in the free stream is unlikely and is hypothesized to occur at the cavities on the nozzle wall.

7. Less pronounced breakup of "nitrogen streams" compared to "hydrogen streams" can be due to lower diffusivity of nitrogen.

8. Growth of hydrogen bubbles in molten iron is mainly limited by gas transport in the liquid phase, whereas growth of nitrogen bubbles may be limited by interface kinetics.

9. Nozzle shape may be important to stream behavior.

10. Addition of surface tension-lowering elements to the molten iron seems to have no effect on the extent of stream breakup.

Statements from six to ten can be subject for discussion. The nucleation of gas bubbles in a supersaturated liquid

metal is not well understood. For example, what is the mechanism for the secondary fragmentation? If it is attributed to the bursting of gas bubbles then the possibility of spontaneous nucleation (i.e., due to spontaneous density fluctuations) within liquid droplets is implicitly assumed, contrary to the "general belief" that spontaneous nucleation in the main stream is not possible.

The likely mechanism of the preferential nucleation at the cavities on the nozzle wall has not been investigated to the knowledge of this author. This will be discussed in the next chapter. Finally, the role of chemical kinetics in growth of nitrogen bubble is not clear.

2.3 Nucleation of Gas Bubble in Liquid Metals

2.3.1 Introduction

Nucleation, defined as a process in which a stable phase is formed from a preexisting metastable phase, can be classified, following Bankoff,[37] as follows:

1. Spontaneous nucleation
2. Preferential nucleation

Spontaneous nucleation is due to statistical density fluctuations and can be homogeneous or heterogeneous. Nucleation is homogeneous if it occurs spontaneously in the bulk phase and heterogeneous if it occurs spontaneously at the interface with a second phase, such as a solid wall, inclusions, or liquid-liquid interface. Preferential nucleation refers to a condition when a stable nucleation embryo already exists in the form of, for example, microscopic gas bubbles.

Nucleation in liquids has been extensively studied because of its importance for boiling and cavitation processes. Recently, the nucleation theory has found an important application in liquid-liquid systems in connection with investigation of vapor explosions.[38] Bankoff[37] and Skripov[39] have reviewed theory, its applications, and experimental confirmation. The agreement between theoretical predictions and experimental observations for organic liquids is reported to be excellent. Agreement for water is not very good, which is due to some local pseudocrystallinity.[37]

The nucleation theory, in its "classical" shape, has been used in investigation of gas bubble nucleation in supersaturated liquid metals. Agreement between theory and observation is, however, poor.

It was mentioned in Section 2.2 that homogeneous nucleation of gas bubbles in the free, supersaturated stream of liquid iron is considered practically impossible due to the high surface tension of iron. Supersaturations corresponding to equilibrium gas partial pressure on the order of 40,000 atm would be required. On the other hand, according to Richardson,[40] it appears to be possible to obtain nucleation of gases in liquid metals under conditions that seem to preclude heterogeneous nucleation, with gas supersaturations in the range of 20 to 100 atm.

Results of nucleation theory applied to nucleation of gas bubbles in molten iron are presented next.

2.3.2 Homogeneous Nucleation

The following considerations are based on presentations by Hirth and Pound[41] and Skripov.[39] Nucleation theory was developed by Volmer, Becker, Döring, Zel'dovich, and others. A review and applications of the theory relevant to our problem may be found in References 42 through 45.

The frequency of spontaneous nucleation of bubbles per unit volume of superheated liquid is given by

$$J = Z\omega A^* n^* \quad , \tag{16}$$

where Z is the Zel'dovich nonequilibrium factor,

$$Z = (W^*/3\pi kTi^{*2})^{1/2} \quad . \tag{17}$$

Here ω is the rate by which the critical embryo (nucleus) gains a single molecule per unit area.

This rate is obtained from kinetic gas theory assuming the Maxwell-Boltzman velocity distribution:

$$\omega = P^*/(2\pi mkT)^{1/2} \quad . \tag{18}$$

In Equation (16) A^* is the area of the nucleus,

$$A^* = 4\pi r^{*2} \quad , \tag{19}$$

and n^* is the number density of critical bubbles at metastable equilibrium,

$$n^* = n_o \exp(-W^*/kT) \quad , \tag{20}$$

where n_o is the molecular density of the liquid. In Equation (17) i^* is the number of molecules in the critical bubble:

$$i^* = \frac{4}{3} \frac{\pi r^{*3}}{\Omega_g} \quad . \tag{21}$$

Here Ω_g is the molecular volume of the gas in the bubble. Assuming perfect-gas behavior we have

$$\Omega_g = \frac{kT}{P_g} \quad ,$$

thus

$$i^* = \frac{4}{3}\pi r^{*3} \frac{P_g}{kT} \quad , \tag{22}$$

where k is Boltzmann's constant.

In above expressions, W^* is the work required (in an isothermal, reversible process) to form a spherical nucleus, i.e., a critical bubble, within a large homogeneous mass of mother phase. This work was calculated by Gibbs[46] and interpreted by him as a measure of phase stability.

The work of formation of a spherical bubble at constant temperature and pressure is

$$W = 4\pi r^2 \sigma + \frac{4}{3}\pi r^3 \left(P_f - P_g\right) + \left(\mu_g - \mu_f\right) M_g \quad , \tag{23}$$

where r is the radius of the bubble, σ is the surface tension, P is the pressure, μ is the chemical potential, and M is the mass of the gas in the bubble. Subscripts f and g refer to liquid and gas phase, respectively.

The first term in this expression is the work of forming a surface, the second term is pV work and the last term represents the change of free energy when bubble is formed.

The work W has a maximum, W*, at r* and P_g^*. The bubble, which is now a critical embryo, is then in mechanical and chemical equilibrium with surrounding liquid and we have

$$P_g^* = P_f + \frac{2\sigma}{r^*} \tag{24}$$

and

$$\mu_g(P_g,T) = \mu_f(P_f,T) \quad . \tag{25}$$

Thus, combining Equations (23), (24), and (25), we get

$$W^* = \frac{16\pi\sigma^3}{3\left(P_g^* - P_f\right)^2} \quad . \tag{26}$$

Combining Equations (16), (17), (18), (19), (20), (21), (22) and (26) we obtain

$$J = \left(\frac{2\sigma}{\pi m}\right)^{1/2} n_o \exp -\left[\frac{16\pi\sigma^3}{3kT\left(P_g^* - P_f\right)^2}\right] \quad . \tag{27}$$

The mean waiting time, $\bar{t}$, for the critical bubble to appear in a volume V is

$$\bar{t} = \frac{1}{JV} \quad . \tag{28}$$

When Equation (27) is used in connection with nucleation process in gas-supersaturated liquid, then n_o is a molecular concentration of solute. Inspection of Equation (27) reveals that surface tension has a strong effect on J, but m and n_o are relatively unimportant.

The supersaturation necessary to nucleate a gas bubble in a given liquid volume can be calculated from Equation (27). At the critical supersaturation the rate of homogeneous nucleation will change rapidly from a very small to a very high value. According to Lothe and Pound[47] the critical supersaturation can be defined to be that at which the logarithm of the nucleation rate equals zero, i.e., J = 1.

Let us consider nucleation of the nitrogen bubble in liquid iron. The estimated nitrogen concentration in iron for conditions of the SPIT-8 test is 26 kgN/m^{3}Fe, which corresponds to the nitrogen equilibrium pressure of 7.5 MPa at 2800 K. From Equation (27) we have

$$\left(P_g^* - P_f\right)^2 = - \frac{16\pi\sigma^3}{3kT \ln\left(\frac{J}{n_o(2\sigma/\pi m)^{1/2}}\right)} \quad . \tag{29}$$

The following data have been used:

$$n_o = 1.12 \times 10^{27} \text{ atoms N/m}^3\text{Fe}$$

$$\sigma = 1.2 \text{ N/m}$$

$$m = \frac{28}{6.02 \times 10^{26}} = 4.65 \times 10^{-26} \text{ kg}$$

$$k = 1.38 \times 10^{-23} \text{ JK}^{-1}$$

$$T = 2800 \text{ K}$$

$$J = 1 \text{ m}^{-3}\text{s}^{-1}$$

We obtain

$$\left[P_g^* - P_f\right]^2 = 8.21 \times 10^{18} \text{ N}^2/\text{m}^4$$

and

$$P_g^* - P_f = 2.86 \times 10^9 \text{ N/m}^2 = 2.86 \times 10^3 \text{ MPa} \quad .$$

Thus the supersaturation corresponding to the partial equilibrium pressure of nitrogen on the order of 3×10^3 MPa would be required to achieve any substantial nucleation rate.

The result would be essentially the same if J or n_o were increased by a factor of 10. Similar results were obtained by Bradshaw[24] for the case of hydrogen bubble nucleation in liquid steel and by Levine[48] for the case of nucleation of gas bubbles in the liquid Zr-O-N system.

For the reactor case with hydrogen concentration in iron of 2.25 kgH/m^3Fe, corresponding to the hydrogen equilibrium pressure of 6.4 MPa at 2500 K, we would obtain $P_g^* - P_f = 3 \times 10^3$ MPa.

If we were to calculate J for $P_g^* = 7.5$ MPa then nucleation rate would be essentially zero and the waiting time, according to Equation (28), infinite. As mentioned earlier, it seems possible to nucleate gas bubbles in liquid metals with gas supersaturations in the range of 2 to 10 MPa. It has been speculated[40] that classical theory of homogeneous nucleation is not applicable for liquids with very high surface tension, like liquid metals, or for solutions.

The only serious attempt known to this author aimed at explanation of homogeneous nucleation in liquid metals is due to Levine.[48,49,50] Levine has analyzed the mechanism of bubble formation in Zr-O-N and Fe-C-O melts and the study was initiated by observation of explosion and sac formation in Zr-O-N systems.[51] The reversible work of formation of critical bubble was modified by including the electrostatic terms involved in forming a layer of chemisorbed oxygen ions. In consequence, the barrier to the phase change may be greatly reduced due to the electrostatic expansion pressure caused by the chemisorbed layer. According to Levine the maximum change in Helmholtz free energy ΔF^* (which corresponds to W^*) is

$$\Delta F^* = \frac{16\pi\sigma^3}{3\left(P_g^* - P_f\right)^2} \Psi \quad , \tag{30}$$

where

$$\Psi = 1 - 3\,(\sigma_o/\sigma)^2 + 2(\sigma_o/\sigma)^3 \quad , \tag{31}$$

and σ_o is the electrostatic energy density of the interface region. Thus, if $\sigma_o/\sigma = 1$ then Ψ and $\Delta F^* = 0$. Levine has analyzed bubble formation in Fe-C-O systems

and concluded that critical bubble nucleation conditions are determined almost entirely by the oxygen content of the melt. Critical concentration of oxygen was found to be in the 0.001 to 0.003 w/o range at 1823 K, i.e., for these values $\sigma_o/\sigma \rightarrow 1$ and $\Psi \rightarrow 0$.

The oxygen concentration in thermite melts and in corium is certainly higher than 0.001 w/o. Hence, Levine's modified theory of homogeneous nucleation would permit bubble nucleation in the free molten stream even in the absence of active nucleation sites.

The surface tension of liquid iron and steel is significantly reduced by additions of oxygen and sulfur, which are highly surface-active elements in iron. According to Swisher and Turkdogan,[52] addition of 0.1 weight percent oxygen lowers the surface tension of iron at its melting point (1537°C) from 1.8 N/m to 1.0 N/m. The surface tension decreases also with increasing temperature. According to Allen,[53] the temperature coefficient of the surface tension of iron at its melting point is $-4.9 \times 10^{-4} \pm 2.5 \times 10^{-4}$ N/m•K. Assuming that the surface tension of iron contaminated with oxygen is 1 N/m at its melting point, we obtain the following equation:

$$\sigma = 1.76 - 4.9 \times 10^{-4}(T-273) \quad , \tag{32}$$

where T is the temperature in degree Kelvin. The similar approach to account for temperature effects was used by Ostensen, et al.[54]

Nikolopoulos and Ondracek[55] investigated interfacial energies between uranium dioxide and liquid metals. The following formula for the surface tension of molten stainless steel was extracted from this reference:

$$\sigma = 1.19 - 0.57 \times 10^{-3}(T-1690) \quad . \tag{33}$$

It should be emphasized that the above formulas are only approximations.

If we use Equation (32) for the experimental and reactor conditions, we obtain:

Experiment: $T = 2800$ K, $\sigma = 0.52$ N/m

Reactor Case: $T = 2500$ K, $\sigma = 0.66$ N/m .

The critical supersaturation for these values of surface tension is:

$$\text{Experiment:} \quad P_g^* - P_f = 7.7 \times 10^2 \text{ MPa}$$

$$\text{Reactor Case:} \quad P_g^* - P_f = 1.2 \times 10^3 \text{ MPa}$$

Hence the critical supersaturation is reduced by a factor of 4 for the SPIT case and by a factor of 2.5 for the reactor case. However, the supersaturation required to achieve any substantial nucleation rate is still very high. If surface tension of liquid iron is reduced to 0.1 N/m, a critical supersaturation of about 70 MPa is obtained. Even if substantial uncertainty exists regarding temperature dependence of surface tension, its reduction below 0.1 N/m seems unlikely. However, the surface tension decrease with increasing temperature may allow for spontaneous heterogeneous bubble nucleation, because the work of critical bubble formation is substantially reduced in this case in comparison with spontaneous nucleation in a bulk phase.

2.3.3 Heterogeneous Nucleation

Heterogeneous nucleation in melts at a flat liquid-solid interface has been analyzed by Bradshaw.[24] Kaplan and Philbrook[56] have studied nucleation at liquid-liquid interface. In this case the wetting conditions, i.e., the contact angle between phases, is of crucial importance. According to Bradshaw,[24] the nucleation rate at flat liquid-solid interface is

$$J = \left(\frac{2\sigma}{\pi m(2-\cos\theta)}\right)^{1/2} n_s \exp\left[-\frac{16\pi\sigma^3}{3kT\left(P_g^*-P_f\right)^2} f(\theta)\right] , \quad (34)$$

where

$$f(\theta) = \frac{(2-\cos\theta)\ (1+\cos\theta)^2}{4} \quad (35)$$

Here θ is the contact angle and n_s is the number of molecules adsorbed on the surface. Figure 5 shows the

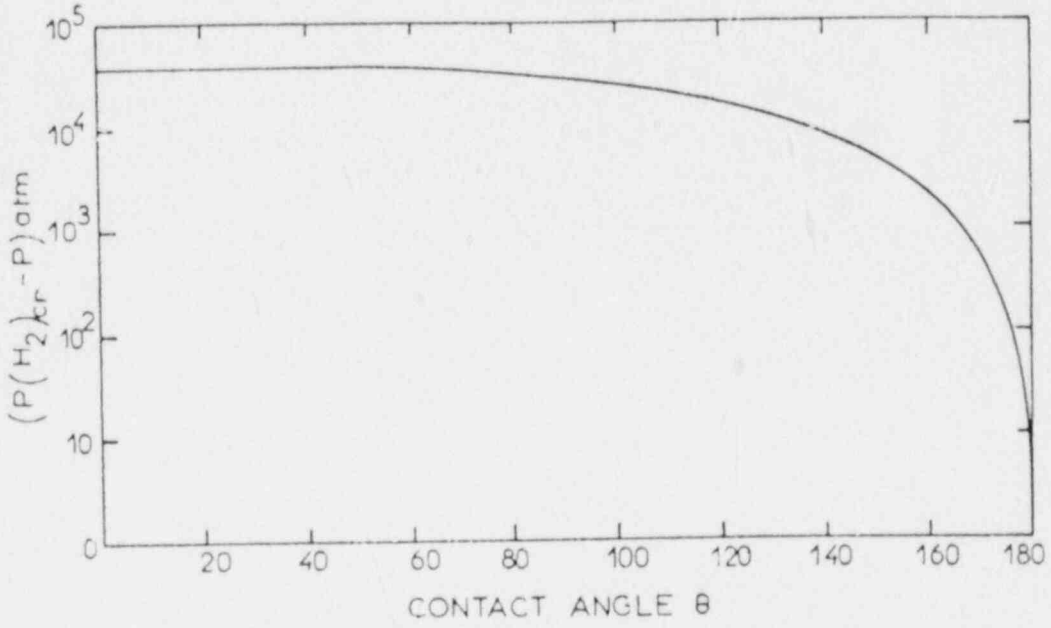

Figure 5. Heterogeneous Nucleation of Hydrogen in Steel on a Flat Substrate. Excess pressure in bubble versus contact angle.[24]

relationship between critical supersaturation and contact angle for the case of hydrogen bubble nucleation in liquid steel.

Figure 5 shows that in order to significantly reduce the critical supersaturation the contact angle corresponding to almost complete nonwetting is required. The situation is similar for other gases and other metals. The contact angles on the order of 160° have been reported for Al_2O_3 and pure iron systems with low content of sulfur and oxygen. For steel on silica or alumina refractories the reported contact angle is in the 100° to 150° range.

Kaplan and Philbrook[56] have calculated the rate of homogeneous and heterogeneous nucleation of CO bubbles within the levitated Fe drop at temperatures of 1900 and 2200 K. Heterogeneous nucleation was calculated at iron-iron oxide interface. The rate of homogeneous nucleation was found to be essentially zero. Although the critical work of CO bubble formation at the liquid-liquid interface was reduced, the nucleation rate was essentially zero even in this case.

2.3.4 Preferential Nucleation

Preferential nucleation from gas or vapor filled surface cavities controls the incipient boiling superheat and therefore is of large importance in studies of pool and forced convection nucleate boiling. The parameter of greatest interest in this connection is the number of active nucleation sites. The surface condition, for example, number and shape of cavities or cracks, surface wetability by liquid, liquid properties, and flow hydrodynamics, are controlling factors which have been investigated by many. In principle the mechanism of preferential nucleation in the case of gas-supersaturated liquid is identical to nucleation from superheated liquid.

In the reactor case, there is a possibility of preferential bubble nucleation in the melt at the sites created by γ, β and perhaps also α radiation due to the local energy deposition. This nucleation mechanism is operative in solid fuel due to the local energy deposition by fission products.

Bradshaw[24] and Richardson[40] have discussed the nucleation of gas bubbles in molten metals at gas-filled cavities. It was shown that a cavity of 10^{-3} cm radius in contact with molten steel (σ = 1 N/m) and for a contact angle less than 90° could be an active nucleation site if the supersaturation pressure exceeded 2 atm. Under the same conditions but for a larger contact angle, the required supersaturation would be reduced. The required cavity radius will also decrease with increasing supersaturation.

Bradshaw[24] has also briefly discussed the possibility of bubble formation at the cavities in suspended solids. The size of suspended particle will depend on the minimum required cavity size, which in turn is a function of contact angle and gas supersaturation. However, nucleation experiments with water show that suspended solid particles are completely wetted in pressurized system. Thus, it appears unlikely that preferential nucleation on suspended solid particles could play a role in experiments and reactor accident.

2.3.5 Discussion and Conclusions

The mechanism of gas bubble nucleation in supersaturated molten metals is obviously not well understood. This applies particularly to the case of spontaneous nucleation. This author is not aware of any study of bubble nucleation at surface cavities for the flowing, gas supersaturated molten metal. Considering these facts, the quantitative analysis of bubble nucleation in the free jet of supersaturated molten metal would be very difficult, if at all possible. Such an analysis could be a subject for separate

study and is beyond the scope of the present work. We would like to discuss, however, in qualitative manner some aspects of bubble formation in connection with stream degassing and experiments and reactor accidents.

There is some experimental evidence, as discussed earlier, that shape and surface conditions of the discharging nozzle affect the breakup of gas-supersaturated jets. Similar observations have been made for jets of superheated liquids.[57] However, Fedoseev[58] has reported that the extent to which the superheated water jet is disintegrated is only a function of nozzle diameter, not the shape. Some researchers postulate that bubble nucleation occurs on the nozzle wall and that these bubbles ultimately shatter the jet. A question which one can ask is what happens to these bubbles after they have detached from the nozzle wall. When the flow is turbulent, the bubbles may be transported toward the jet centrum because of the turbulent diffusion. If the flow is laminar, the bubbles should be found in the boundary region near the jet surface, and one would expect the "erosion" of only the outer layer of the jet, if there is no nucleation in the bulk of the stream.

In all experimental studies on jet disruption known to this author, the nozzle diameter was very small, normally in the range of tenths of millimeters to a few millimeters. Under such circumstances, only a few gas bubbles can disrupt the jet. The situation is quite different in SPIT and JETA-B tests and in reactor accident situations. The initial jet diameter in the tests is 2.5 cm and in the reactor case, 4 cm. In the latter case the jet diameter will increase substantially due to the ablation process. Thus, if bubble nucleation on the nozzle wall is postulated then the turbulent diffusion of microbubbles towards jet centrum is required.

Ablation of the nozzle wall, also observed in some tests, is an important consideration since gas-filled cavities on the nozzle wall, which can act as nucleation sites, will be quickly destroyed.

X-ray photographs of SPIT-8, JETA-B2 and JETA-B3 jets (see Figures 3, 6, and 7) show that void is more or less uniform throughout the jet close to the orifice. This observation, ablation of the nozzle wall, and the fact that nozzle flow in tests and reactor case is most likely not turbulent (L/D ~1) contradicts the hypothesis that jet disruption is caused by gas bubbles that are formed on the nozzle wall. However, regardless of what is the mechanism of bubble nucleation it appears that the nozzle geometry is an important factor since it determines the flow conditions inside and outside the nozzle.

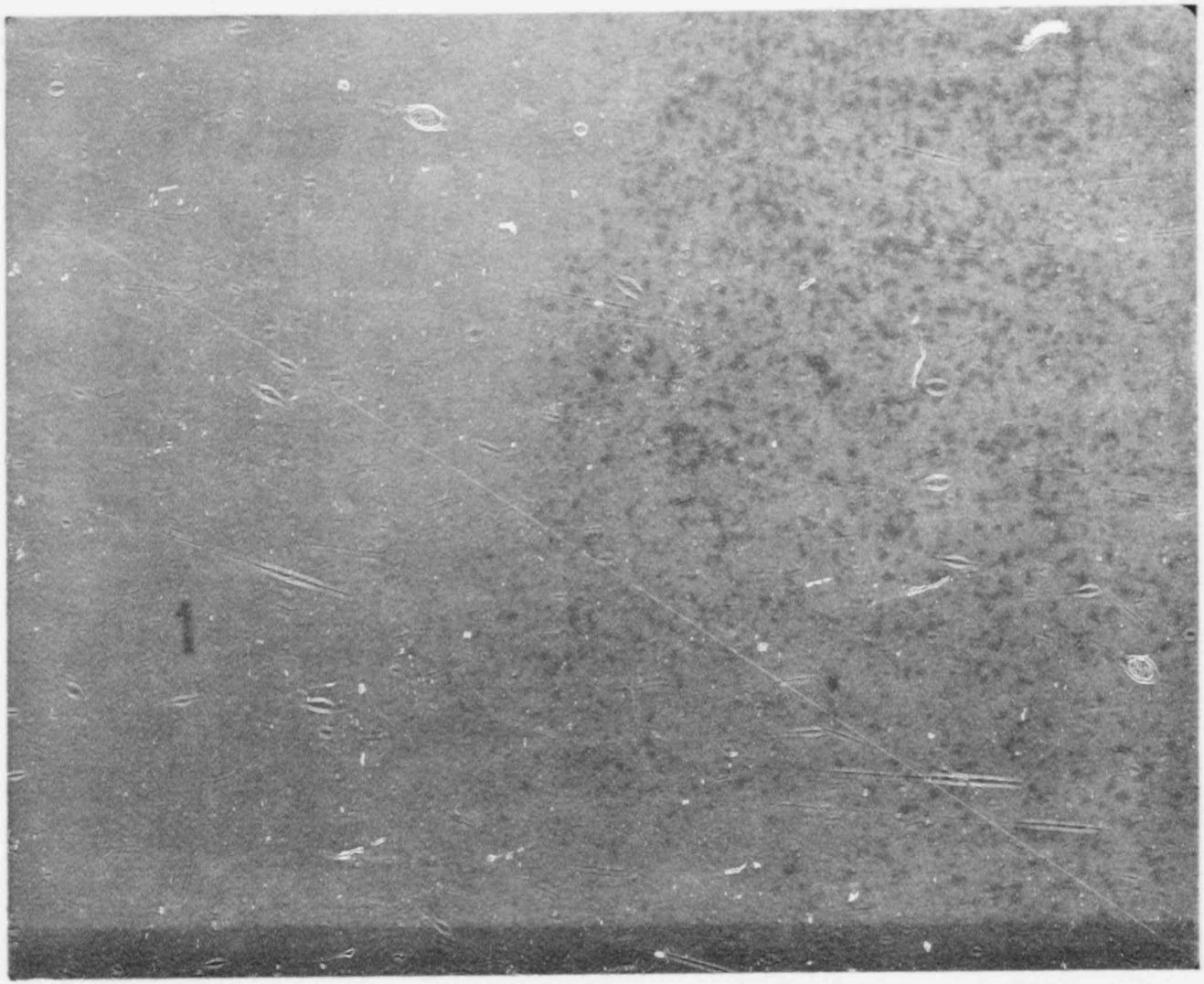

Figure 6. Flash X-Ray Photograph of H_2-Driven Jet of the JETA-B2 Test Taken 15 ms After Start of Melt Ejection. About half of the jet is shown. The jet length is 30 cm and the distance from the top edge of the photograph to the melt generator exit is 8 cm.

Figure 7. Flash X-Ray Photograph of H_2-Driven Jet of the JETA-B3 Test Taken 15 ms After Start of Melt Ejection. The jet length is 30 cm and the distance from the top edge of the photograph to the melt generator exit is 8 cm.

From above considerations we conclude that the possibility of spontaneous nucleation in the bulk of the melt stream cannot be disregarded. As stated earlier, the theory of Levine explains spontaneous nucleation in liquid metals. Another possible explanation, relevant to jet flow, was advanced by Kaskiwa and Mjolsness.[59] Based on analysis of some experimental data for flashing water jets, they proposed that strong flow acceleration, caused by the sudden depressurization, may lower the superheat required for spontaneous nucleation. As a result of flow acceleration, the relative motion between microbubbles and the liquid is induced which may cause normally stable bubbles to become unstable, thus lowering the required superheat, or supersaturation.

As mentioned earlier, experimental observations clearly indicate that gas bubbles are formed in the nozzle or just outside it. Therefore, it is interesting to compare the characteristic nucleation time with time it takes for the flow to pass through the nozzle. The characteristic time of spontaneous homogeneous nucleation in case of bubble nucleation due to diffusion of dissolved gas was obtained by Hijikata, Mori and Nagatani.[60] It is

$$t = \frac{n_c^2}{4\pi NDR_c} \quad , \tag{36}$$

where n_c is the number of molecules in the critical bubble, R_c is the critical bubble radius, N is the number of molecules per unit volume of the dissolved gas and D is the coefficient of diffusivity.

For SPIT, JETA-B, and reactor accident conditions the order of magnitude of the characteristic nucleation time obtained from the above expression is about 10^{-3} s. The time it takes the flow to pass through the nozzle is on the order of 10^{-3} to 10^{-4} s. Hence the spontaneous homogeneous nucleation would take place either inside the nozzle or within a short (< 10 cm) distance from the nozzle exit. This result is in agreement with observations.

We conclude finally, that we are not able to calculate the rate of bubble formation in experiments and reactor accident situations. Therefore, the number density of gas bubbles in the molten jet will be treated as a parameter in the model and determined experimentally.

2.4 Jet Expansion and Primary Breakup

2.4.1 Introduction

Our objective is to develop a model of jet expansion and primary breakup as a result of effervescence of dissolved

gas. In particular, we want to be able to predict the jet spread angle, the jet void fraction, size of the gas bubbles, and the bubble pressure as a function of time. This information is needed for comparison with experiments and fragmentation calculations.

A general description of jet behavior used in this work, along with all relevant variables, is shown in Figure 8. The molten jet in an experiment or reactor accident is characterized by temperature, T, average density, ρ, composition, x_i, equilibrium concentration of dissolved gas, C_o, and velocity, v_j. For reasons given in Sections 2.6 and 2.7, we consider only one gas, nitrogen or hydrogen, dissolved in the iron component of the melt.

Secondary fragmentation of melt droplets, indicated in Figure 8, is studied in Section 3 of this report.

In Section 2.4.2 a model of jet expansion is developed.

2.4.2 Jet Expansion Model

A schematic of a jet expansion model is shown in Figure 9. The following assumptions are made and additional assumptions will be introduced in the course of the presentation.

1. N gas bubbles per m^3 of liquid are formed at the same time. The bubbles have uniform size and are uniformly distributed in space.

   These assumptions are often made in studies of nonequilibrium vapor generation in flashing flows. In reality there will be a distribution of bubble sizes and the bubbles will nucleate in a flow zone of finite dimensions. Leslie[61] investigated the effect of initial bubble radius on the growth expression for a vapor bubble growing in a superheated liquid. The growth was diffusion controlled. He found that the bubble radius becomes independent of initial radius when the bubble has grown to a few times its initial radius.

   According to Saha et al.,[62] the nucleation zone is short and the contribution of the bubbles nucleated downstream of this zone can be neglected.

2. The assumption of spherical bubbles is quite accurate for small bubbles because of the surface tension forces and is a reasonable approximation for larger bubbles in the free jet. Bubble interaction and turbulent motion in the jet will cause departure from sphericity, but these effects are neglected.

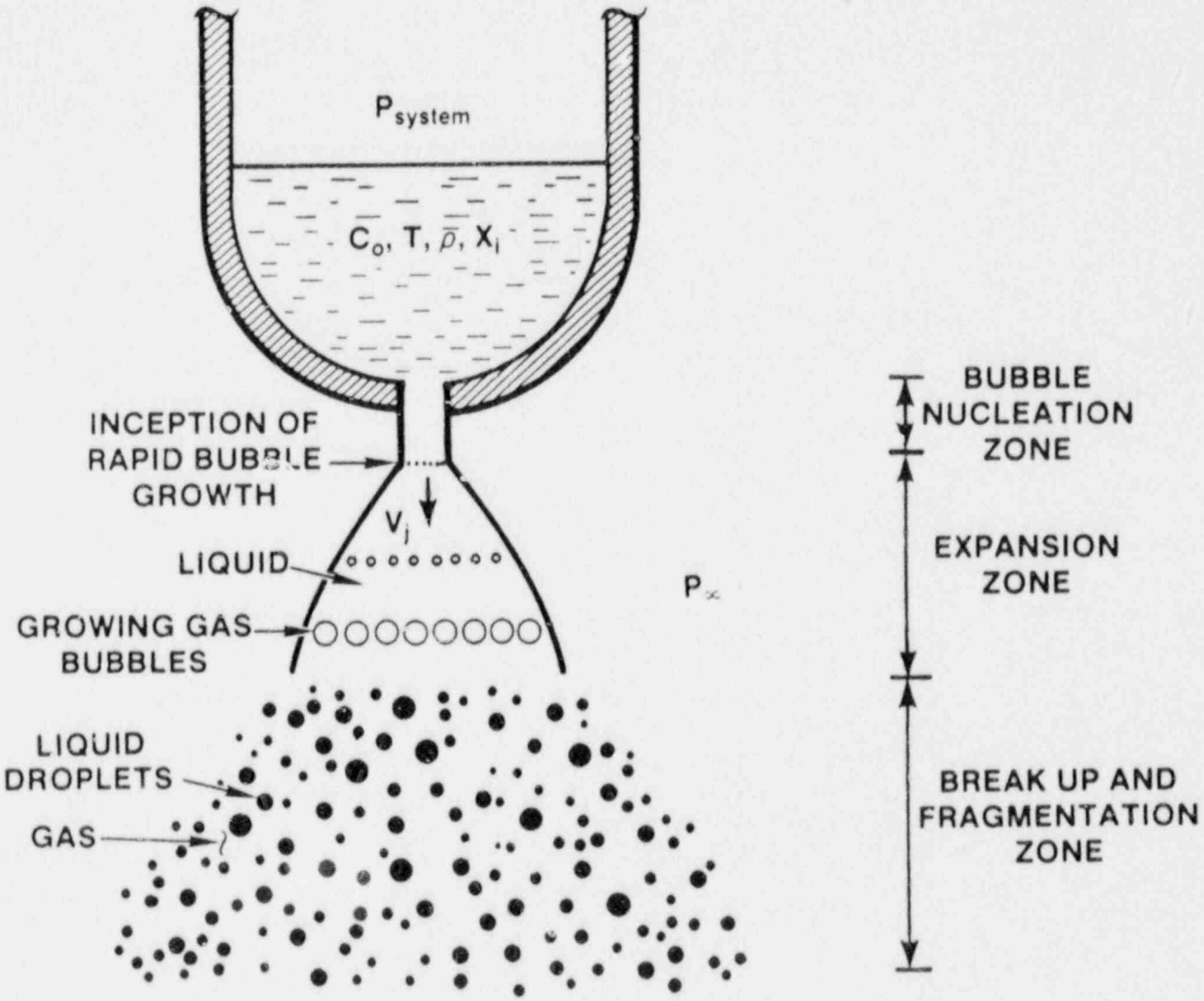

Figure 8. Schematic of Jet Expansion and Breakup

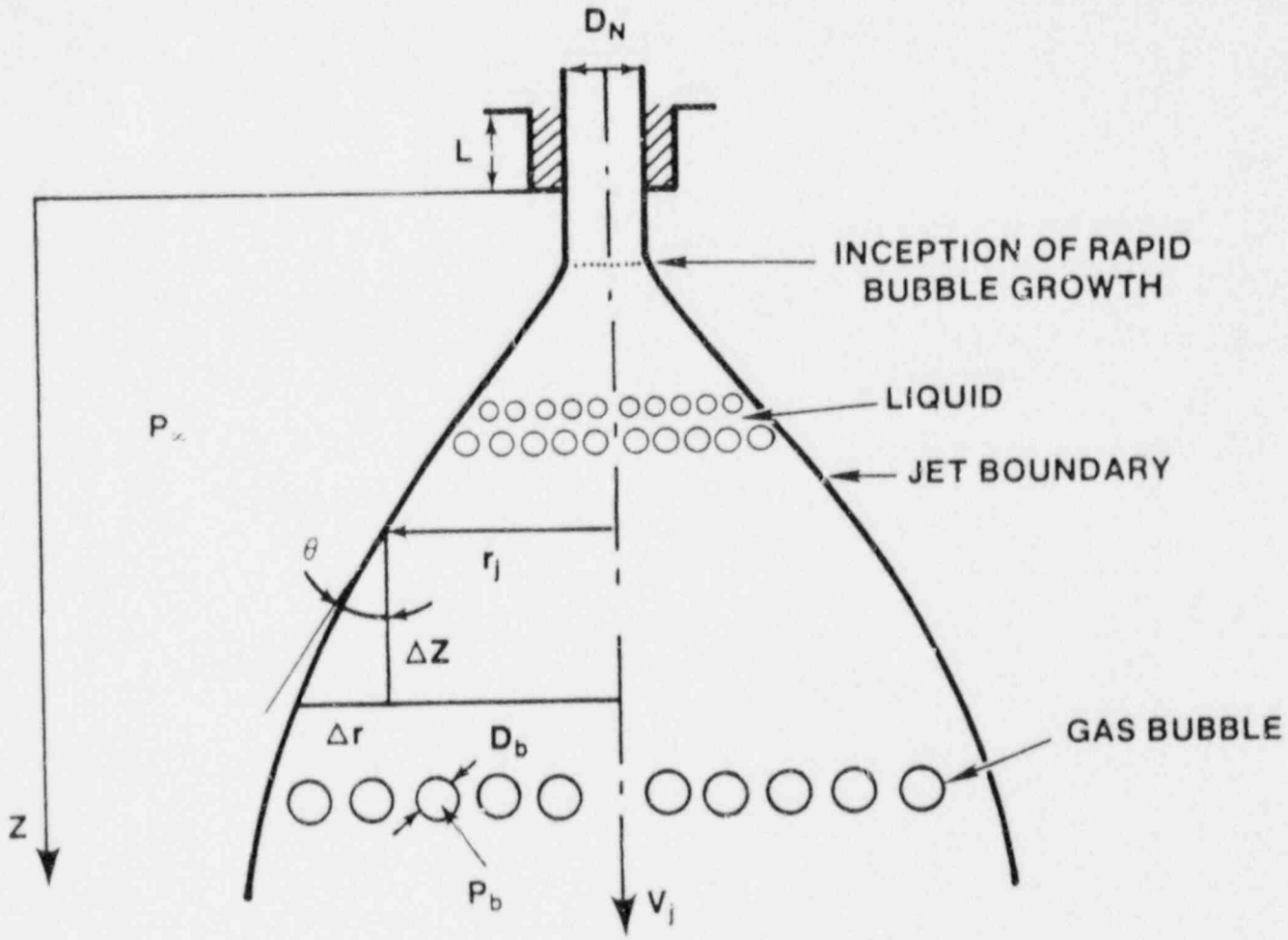

Figure 9. Sketch Showing the Jet Expansion Model

3. Bubble coalescence or bubble/bubble interactions are not accounted for.

4. Constant liquid properties are not assumed.

5. The jet velocity is assumed constant in the axial direction.

6. One-dimensional axial flow is assumed. The importance of changes in radial direction should be investigated and included in the more detailed model. For example, it is now assumed that the pressure across the jet is uniform and accordingly the void fraction is not a function of radius.

7. Steady-state, or at least quasi-steady conditions are assumed. We consider the jet to be a homogeneous, bubbly, two-phase flow with no relative velocity between liquid and gas phase (i.e., slip = 1).

Given these simplifying assumptions, the equation of continuity of mass takes the simple form of

$$\bar{\rho} v_j A = \text{const} \quad , \tag{37}$$

where ρ is the mixture (or mean) density, v_j is an axial jet velocity, and A is a jet cross-sectional area.

According to assumption 5,

$$v_j = \text{const} \quad . \tag{38}$$

The mixture density $\bar{\rho}$ is given by

$$\bar{\rho} = \rho_g \alpha + \rho_\ell (1-\alpha) \quad . \tag{39}$$

Here α is the void fraction; subscripts g and ℓ refer to gas and liquid phase, respectively.

In our case $\rho_\ell >> \rho_g$; hence

$$\bar{\rho} = \rho_\ell (1-\alpha) \quad . \tag{40}$$

Equation (37) can be written as

$$\bar{\rho} v_j A(z) = \bar{\rho}_o v_j A_o \quad , \tag{41}$$

where o refers to initial conditions inside the orifice. Combining Equations (40) and (41), we obtain

$$A(z) = \frac{1 - \alpha_o}{1 - \alpha} A_o \quad . \tag{42}$$

But

$$A(z) = \pi r_j^2(z) \quad ,$$

and

$$A_o = \pi r_N^2 \quad .$$

Thus we get

$$r_j(z) = \left(\frac{1-\alpha_o}{1-\alpha}\right)^{1/2} r_N \quad , \tag{43}$$

or

$$\frac{r_j}{r_N} = p = \left(\frac{1-\alpha_o}{1-\alpha}\right)^{1/2} \quad , \tag{44}$$

where p is the nondimensional jet radius and r_N is the nozzle radius.

The instantaneous jet spread angle (half-angle) is obtained from Equation (43):

$$\tan \Theta = \frac{dr_j}{dz} \quad . \tag{43a}$$

Neglecting the initial void fraction, α_o, since the initial bubble radius is negligibly small ($R_o \approx 10^{-7}$ m; see Section 2.6.3.1), we obtain by differentiation of Equation 43

$$\frac{dr_j}{dz} = \frac{1}{2} r_N \left|1-\alpha(z)\right|^{-3/2} \frac{d\alpha(z)}{dz} \quad . \tag{45}$$

The jet void fraction is determined as follows. From definition

$$\alpha = \frac{\text{gas volume}}{\text{total volume}} = \frac{V_g}{V_g + V_L} \quad . \tag{46}$$

Assuming that number density of nuclei is N, the bubble radius at the inception of jet expansion R_o, and the change in liquid volume as a result of gas evolution is negligible, we can write

$$V_g = \frac{4}{3} \pi R^3 NV \quad ,$$

and

$$V_L = V - \frac{4}{3} \pi R_o^3 NV = V\left(1 - \frac{4}{3} \pi R_o^3 N\right) \quad .$$

Here V is the total mixture volume and R the bubble radius. Substituting expressions for V_g and V_L into Equation (46), we obtain the general expression for void fraction:

$$\alpha = \frac{4/3\ \pi N R^3}{1 + 4/3\ \pi N(R^3 - R_o^3)} \quad . \tag{47}$$

Now, dr_j/dz can be obtained.

$$\frac{d\alpha}{dz} = \frac{d\alpha}{dt} \frac{dt}{dz} = \frac{1}{v_j} \frac{d\alpha}{dt} \tag{48}$$

and from Equation (47), assuming again that $R_o = 0$,

$$\frac{d\alpha}{dz} = \frac{4\pi NR^2}{\left[1 + 4/3\ \pi NR^3\right]^2} \frac{dR}{dt} \quad . \tag{47a}$$

Finally, combining Equations (43a), (45), (47a), and (48), we get

$$\tan\Theta = \frac{dr_j}{dz} = \frac{r_N}{2v_j}\left[1-\alpha(z)\right]^{-3/2} \frac{4\pi NR^2}{\left[1 + 4/3\ \pi NR^3\right]^2} \frac{dR}{dt} \quad , \tag{49}$$

where $\alpha(z) = f[R(t)]$ is given by Equation (47) and $R_o = 0$.

In order to calculate Θ, the jet velocity, v_j, number density of nuclei, N, and bubble radius as a function of time, R(t), must be known.

The primary jet breakup is expected to occur when the jet void fraction is about 50 percent because at this void fraction the gas bubbles are very close to each other (assuming that they are arranged on a simple cubic lattice).

Considering that the melt volume per bubble is approximately $V_f = 1/N$, the average size of the melt droplet, D, produced by the primary jet breakup can be obtained:

$$\frac{\pi D^3}{6} \approx \frac{1}{N} \quad .$$

Therefore $D \approx \left(\frac{6}{\pi N}\right)^{1/3}$.

The method of calculating bubble radius as a function of time is presented in the next section.

2.5 Dynamics of Bubble Growth in Supersaturated Liquid

2.5.1 Introduction

The rate of bubble growth is a major variable in the jet expansion model. We have found that in order to correctly model behavior of hydrogen supersaturated molten jet a general model of bubble growth, covering various growth stages, is required. Before presenting this model it will be useful to briefly review and discuss some elements of the bubble growth theory.

Bubble dynamics have been extensively studied because of the importance of this subject in understanding boiling and cavitation. Similarly as in the case of bubble nucleation

these studies are mainly concerned with superheated ordinary liquids. Investigations of bubble growth due to gas diffusion in the supersaturated liquids are rather scarce, especially in molten metals. Fortunately, the methods and results of studies of bubble problem in superheated liquids can be directly employed for gas supersaturated liquids, including molten metals.

Bankoff[63,64] has reviewed in detail theoretical and expermental works on bubble dynamics and also various applications as, for example, in nuclear reactor safety. In a general case the bubble growth is controlled by a rate at which the energy and/or mass is transported to the bubble wall, liquid inertia, and viscous and surface tension forces. The problem is very complex because of the coupling between transport equations and equations of motion (the position of the moving phase boundary is not known a priori) and the exact simultaneous solution of governing equations is not available. A number of approximate solutions are available that yield a reasonable agreement with experimental data and numerical solutions of the exact problem.

Analytical efforts have been concentrated on the early stage of bubble growth when the liquid inertia is a dominating factor and on the late, so-called asymptotic, stage when hydrodynamic effects are negligible and growth is controlled solely by energy and/or mass diffusion. Solutions that cover the entire growth process, except the very early stage in which the surface tension forces are important, based on an interpolation procedure between inertia controlled and asymptotic stage, have been proposed.

The problem of inertia controlled bubble dynamics was solved by Rayleigh.[65] Plesset and Zwick[66,67] Forster and Zuber,[68] Birkhoff et al.,[69] Scriven,[70] and Bankoff[71] have proposed solutions for the bubble growth due to heat diffusion in a uniformly superheated liquid. Interpolation solutions were obtained by Mikic, Rohsenhow, and Griffith,[72] and Theofanous and Patel.[73] Prosperetti and Plesset obtained a general, approximate solution using scaled variables.[74]

Most of the mentioned studies, and many others, were concerned with bubble growth in superheated liquids. We are, however, interested in the growth due to the mass diffusion in gas supersaturated liquid. This particular problem was investigated by Szekely and Martins,[75,76] Martins,[77] Szekely, Martins, and Fang,[78] Rosner and Epstein,[29] Szekely and Fang,[79] Barlow and Langlois,[80] and Langlois.[81] These studies are mainly an adaption of ideas and results originally developed by Plesset and Zwick, Birkhoff and Scriven.

In Sections 2.5.2 and 2.5.3, we briefly present the general and nondimensional formulation of the bubble growth problem

due to mass diffusion. The solutions to inertia and diffusion controlled growth stages are given in Section 2.5.4 and 2.5.5, respectively.

In Section 2.5.6 we develop an interpolation model of bubble growth due to mass diffusion. This bubble growth model is used in the jet expansion model presented in the previous section. Finally, in Section 2.5.7 we discuss some aspects of bubble interaction.

2.5.2 General Formulation

The model of spherical bubble growth in a gas supersaturated liquid is shown in Figure 10.

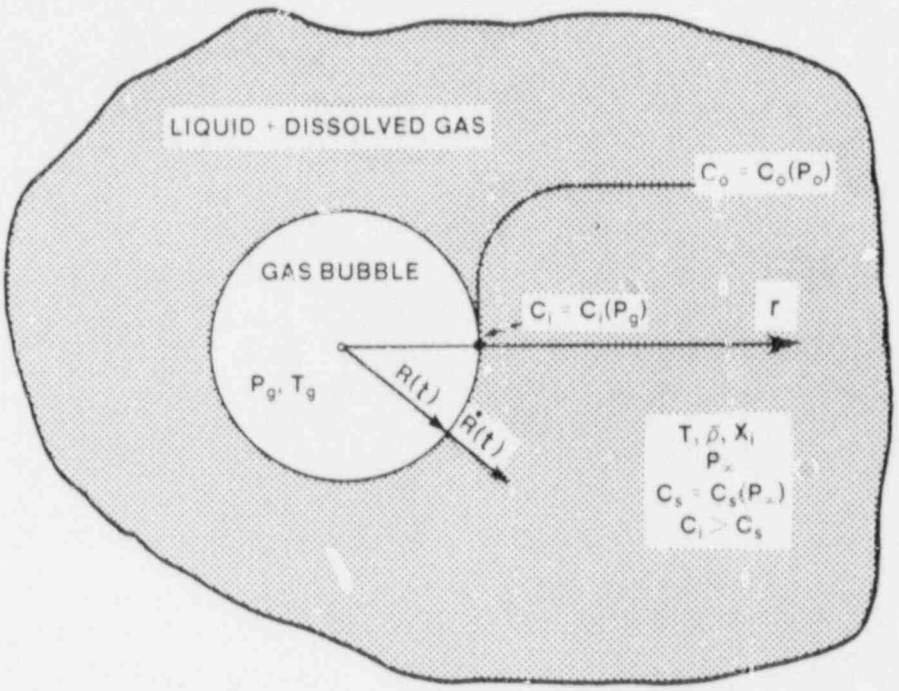

Figure 10. Model of Gas Bubble Growth in a Supersaturated Liquid

The following assumptions are made:

1. Spherical symmetry regarding bubble geometry and concentration field surrounding the bubble.

2. Single bubble in a quiescent, supersaturated liquid of infinite extent. This means that bubble spacing is large enough to avoid competition for solute and interaction of velocity fields. These assumptions are discussed in Section 2.5.7.

3. No relative motion between the bubble and liquid.

4. Chemical equilibrium at the bubble-liquid interface.

5. Thermodynamic equilibrium between the gas in the bubble and the liquid at the bubble wall.

6. Isothermal system.

7. Incompressible liquid.

8. Constant properties of the liquid.

9. Constant diffusion coefficient.

10. Newtonian fluid.

Additional assumptions will be introduced in the course of presentation.

- Equation of Continuity

Equation of mass continuity for spherical symmetry takes, in this case, the following form:[82]

$$\frac{\partial}{\partial r}\,(r^2 u) = 0 \quad . \tag{50}$$

Thus

$$r^2 u(r,t) = f(t) = R^2 u(R,t) \quad , \tag{51}$$

where $u(r,t)$ is the radial liquid velocity, R is the bubble radius, and $f(t)$ is a function of time. Since the term r^2u is not a function of the radial coordinate, it has been evaluated at the bubble wall. From mass balance at the bubble surface,[70]

$$\frac{d}{dt}\left(\frac{4}{3}\pi R^3 \rho_g\right) = 4\pi R^2 \rho_\ell [\dot{R} - u(R,t)] \quad . \tag{52}$$

The gas density varies slowly with time compared to the bubble volume and therefore one can write

$$u(R) = \frac{\rho_\ell - \rho_g}{\rho_\ell}\,\dot{R} = \varepsilon \dot{R} \quad , \tag{53}$$

where $\varepsilon = \frac{\rho_\ell - \rho_g}{\rho_\ell}$.

Hence Equations (51) and (53) give

$$u(r,t) = \frac{\varepsilon R \dot{R}^2}{r^2} \quad . \tag{54}$$

- Equation of Motion

The equation of motion (Navier-Stokes equation) for this case is[82]

$$\rho_\ell \left[\frac{\partial u}{\partial t} + u \frac{\partial u}{\partial r}\right] = - \frac{\partial p}{\partial r} + \mu \left[\nabla^2 u - \frac{2u}{r^2}\right] \quad . \tag{55}$$

It is interesting to note here that the term in the bracket on the right-hand side of Equation (55) vanishes when velocity, u, is substituted from Equation (51). Thus, it appears that there is no difference between viscous and nonviscous fluid. This "paradox" was discussed by Poritsky.[83] We will see in a moment that liquid viscosity does not disappear from the problem because of boundary conditions at the bubble wall.

Employing Equation (54) and integrating Equation (55) from the bubble wall to infinity, we obtain

$$R \ddot{R} + \left(2 - \frac{\varepsilon}{2}\right) \dot{R}^2 = \frac{p(R) - p_\infty}{\varepsilon \rho_\ell} \quad , \tag{56}$$

where $p(R)$ is the liquid pressure at the bubble wall.

It can be shown[84] that the balance of normal, radial stresses at the bubble wall yields

$$p(R) = p_g - \frac{2}{R}\left(\sigma + 2k\frac{\dot{R}}{R}\right) - 4\mu\varepsilon \frac{\dot{R}}{R} \quad . \tag{57}$$

Here p_g is the gas pressure in the bubble, σ is the surface tension, μ is the liquid dynamic viscosity and k is the effective surface-dilational viscosity.

The term $2k\dot{R}/R$, which accounts for the dynamic surface tension and may be important for very small bubbles,[84] is normally neglected and we get

$$p(R) = p_g - \frac{2\sigma}{R} - 4\mu\epsilon \frac{\dot{R}}{R} \quad . \tag{58}$$

Combining Equations (56) and (58), we obtain

$$\frac{p_g - p_\infty}{\epsilon\rho_\ell} = R\ddot{R} + \left(2 - \frac{\epsilon}{2}\right)\dot{R}^2 + \frac{1}{\rho_\ell}\frac{2\sigma}{R\epsilon} + 4\nu\frac{\dot{R}}{R} \quad , \tag{59}$$

where ν is the kinematic viscosity.

In our case $\epsilon \sim 1$ and we have

$$p_g - p_\infty = \rho_\ell R\ddot{R} + \frac{3}{2}\dot{R}^2 + \frac{2\sigma}{R} + 4\mu\frac{\dot{R}}{R} \quad . \tag{60}$$

- Diffusion Equation

The gas concentration in the liquid is given by Fick's law of diffusion:[82]

$$\frac{DC}{Dt} = D\nabla^2 C \quad , \tag{61}$$

where $\frac{D}{Dt}$ is the substantial derivative and D is the diffusion coefficient.

For spherical symmetry Equation (61) becomes

$$\frac{\partial C}{\partial t} + u\frac{\partial C}{\partial r} = D\left[\frac{\partial^2 C}{\partial r^2} + \frac{2}{r}\frac{\partial C}{\partial r}\right] \quad . \tag{62}$$

From Equation (54), $u = R\ R^2/r^2$, assuming $\epsilon = 1$, and we obtain

$$\frac{\partial C}{\partial t} = D\left[\frac{\partial^2 C}{\partial r^2} + \frac{2}{r}\frac{\partial C}{\partial r}\right] - \frac{\dot{R}\ R^2}{r^2}\frac{\partial C}{\partial r} \quad . \tag{63}$$

- Boundary Conditions

At the interface,

$$\frac{d}{dt}\left(\frac{4}{3}\pi R^3 \rho_g\right) = 4\pi R^2 D\left(\frac{\partial C}{\partial r}\right)_{r=R} \quad . \tag{64}$$

Again, because the gas density varies slowly with time compared to the bubble volume, this equation simplifies to

$$\rho_g \dot{R} = D\left(\frac{\partial C}{\partial r}\right)_{r=R} \quad . \tag{65}$$

At infinity ($r \rightarrow \infty$),

$$C(r,t) = C_o \quad , \tag{66}$$

where C_o is the initial, uniform gas concentration.

- Initial Conditions

$$R = R_o$$

$$\dot{R} = 0 \tag{67}$$

$$C(r,0) = C_o$$

Assuming local thermodynamic equilibrium at the bubble wall, we can write

$$C(R) = f(P_g, T) \quad . \tag{68}$$

If the gas solubility obeys Henry's or Sievert's law, we have

$$C(R) = K(P_g)^{1/n} \quad . \tag{69}$$

Here, K is the equilibrium constant and n = 1 for Henry's law, n = 2 for Sievert's law.

The mathematical formulation of the problem is completely described by Equations (60), (63), and (69), along with boundary and initial conditions.

As mentioned earlier, this system of differential equations has not been solved exactly.

Finally, we want to point out that because of the assumption of an isothermal system, the energy equation was not considered.

2.5.3 Nondimensional Formulation

The effects of liquid inertia, viscosity, and surface tension on bubble growth due to mass diffusion have been studied by Szekely and Martins[75] and Martins[77] using nondimensional formulation of governing equations and numerical calculations. Later, the effect of surface kinetics was also included by Szekely and Fang.[79] The following dimensionless parameters have been defined:

$$\bar{J}a = \frac{\Delta C}{\rho_{g(\rho_\infty)}} \quad \text{reference value of Jakob number}$$

$$G_I = \frac{R_o^2 \Delta p}{\rho_\ell D^2} \quad \text{pressure parameter, diffusion}$$

$$G_K = \frac{\alpha R_c \Delta C}{D\rho_{g(p_\infty)}} \quad \text{pressure parameter, surface reaction}$$

$$\bar{B}_I = \frac{(\bar{J}a)^2}{G_I^{1/2}} \quad \text{growth rate parameter, inertia}$$

$$\bar{B}_K = \frac{(\bar{J}a)^2}{G_K}$$ growth rate parameter, surface reaction

$$\bar{B}_{IK} = \frac{\bar{B}_I}{\bar{B}_K}$$ relative importance of inertia and surface kinetics effects,

where

$$\Delta C = C_o - C_{sat} = C_o - C(p_\infty) \quad ,$$

$$\Delta p = p(C_o) - p_\infty$$

and

α = interface mass transfer coefficient .

After solving numerically the general system of equations for different values of parameters B_I, B_K, and neglecting surface tension and viscous effects, Szekely and Fang[79] found that if

1. B_I, $B_K << 1$; growth is diffusion-controlled
2. $B_I >> 1$

   $B_K << 1$; growth is inertia-controlled
3. $B_K >> 1$

   $B_I << 1$; growth is controlled by surface kinetics
4. B_{IK} large; growth is inertia-controlled

   B_{IK} small; growth is limited by surface kinetics

These recommendations are useful as a first test of which effects may play a role in particular bubble growth case.

2.5.4 Inertia-Controlled Growth

For large liquid superheat or supersaturation and/or low ambient pressure (i.e., low gas density) the velocity of the

bubble wall will be high and growth will be inertia-controlled.

Normally, the effect of viscosity is neglected, except for polymeric or other highly viscous liquids, and Equation (60) becomes

$$\Delta p = \rho_\ell \left(R\ddot{R} + \frac{3}{2} \dot{R}^2 \right) + \frac{2\sigma}{R} \quad , \tag{70}$$

where $\Delta p = p_g - p_\infty$.

Multiplying by $\dot{R}^2 R$ and assuming that Δp is constant, Equation (70) may be integrated from R_o to R to give[85]

$$\dot{R}^2 = \frac{2}{3} \frac{\Delta p}{\rho_\ell} \left[1 - \left(\frac{R_o}{R} \right)^3 \right] - \frac{2\sigma}{\rho_\ell R} \left[1 - \left(\frac{R_o}{R} \right)^2 \right] + \left(\frac{R_o}{R} \right)^3 \dot{R}_o^2 \quad . \tag{71}$$

If growth begins at equilibrium, we have

$$\Delta p = \frac{2\sigma}{R_o} \quad \text{and} \quad \dot{R}_o = 0 \quad .$$

When $R >> R_o$, we obtain

$$\dot{R}^2 = \frac{2}{3} \frac{\Delta p}{\rho_\ell} \quad , \tag{72}$$

$$\dot{R} = \frac{2}{3} \left(\frac{\Delta p}{\rho_\ell} \right)^{1/2} \quad , \tag{73}$$

and

$$R = \left(\frac{2}{3} \frac{\Delta p}{\rho_\ell} \right)^{1/2} t \quad . \tag{74}$$

These are the results originally obtained by Rayleigh.[65]

Assuming that Δp is constant implies that the temperature or concentration gradient at the bubble wall is small. Initially, when the bubble is still relatively small this is a permissible assumption. However, considering that volume-to-surface ratio is proportional to the bubble radius, the requirement to supply enough heat or mass to the bubble wall in order to maintain initial pressure will eventually lead to the establishment of an appreciable temperature or concentration gradient. Thus, after the initial growth period, controlled practically by liquid inertia, the bubble will first enter the intermediate stage when inertia and diffusion controls occur and later the final stage in which diffusion effects practically control the growth rate.

We would like to note that, according to Equation (73), during inertia-controlled growth period the bubble wall velocity is constant.

2.5.5 Diffusion-Controlled Growth

The diffusion-controlled phase of bubble growth (also called asymptotic or late) has been thoroughly studied by many researchers. Two methods of solution have been most widely used; one is based on the assumption that temperature or concentration variation occurs in the thin boundary layer surrounding the bubble wall (Plesset and Zwick[67]) and the second employs self-similar solution (Birkhoff, Margulies, and Horning[69] and Scriven[70]).

The self-similar solutions are exact, but their drawback is that the following simplifying assumptions are required:

a. The initial bubble radius is zero.

b. Inertial and surface tension effects have to be neglected.

c. The vapor density in the bubble is constant.

Additionally, the bubble must grow in uniformly superheated or supersaturated liquid.

It will be shown later that, if the driving force is not small and the bubble radius is approximately 10 times greater than initial radius, the self-similar solution merges with the solution based on the thin boundary layer assumption.

Now, following Scriven,[70] we will outline the method and results of the self-similar solution. For details, the reader is referred to original works by Birkhoff et al. and Scriven or to Bankoff's review of diffusion-controlled bubble growth.[63]

It is assumed that the solution has a form

$$C^*(r,t) = C^*(s) \quad , \tag{75}$$

where

$$C^* = \frac{C_o - C(r,t)}{C_o - C_s}$$

and

$$s = \frac{r}{2\sqrt{Dt}} \quad , \tag{76}$$

where $C_s = C(p_\infty)$, i.e., equilibrium gas concentration at ambient pressure and s is the Boltzmann transformation variable. This implies that

$$R = 2\beta\sqrt{Dt} \quad , \tag{77}$$

where β is the growth constant.

Substituting Equations (75), (76), and (77) into Equation (63) we obtain

$$\frac{d^2C^*}{ds^2} = 2\frac{dC^*}{ds}\left(-s - s^{-1} + \beta^3 s^{-2}\right) \quad . \tag{78}$$

The growth constant β is evaluated by integrating this equation twice and applying boundary and initial conditions. The result is

$$\Phi(\beta) = 2\beta^3 \exp(3\beta^2) \int_\beta^\infty x^{-2} \exp\left(-x^2 - 2\beta^3 x^{-1}\right) dx \quad , \tag{79}$$

where

$$\Phi(\beta) = \frac{C_o - C_s}{\rho_g} = \frac{\Delta C}{\rho_g} \quad , \tag{80}$$

and x is a dummy variable.

Scriven has shown that if $\beta \to 0$, then

$$\Phi(\beta) \simeq 2\beta^2 \quad . \tag{81}$$

Hence

$$R = \left(2 \frac{\Delta C}{\rho_g}\right)^{1/2} (D \cdot t)^{1/2} \tag{82}$$

and

$$\dot{R} = 1/2 \left(2\frac{\Delta C}{\rho_g}\right)^{1/2} D^{1/2} \frac{1}{t^{1/2}} \quad . \tag{83}$$

If β is large (>10), then

$$\Phi(\beta) \simeq \sqrt{\frac{\pi}{3}}\, \beta \quad . \tag{84}$$

Hence

$$R = 2\sqrt{\frac{3}{\pi}} \frac{\Delta C}{\rho_g} (Dt)^{1/2} \tag{85}$$

and

$$\dot{R} = \sqrt{\frac{3}{\pi}} \frac{\Delta C}{\rho_g} D^{1/2} \frac{1}{t^{1/2}} \quad . \tag{86}$$

This result is identical with the leading term of the Plesset-Zwick solution, based on the thin concentration boundary layer approximation for the asymptotic growth phase.

This fact is not surprising considering the following. The thickness of diffusion boundary layer is approximately $\delta \sim 4\sqrt{Dt}$. Thin boundary layer assumption requires that

$$\frac{\delta}{R} << 1 \quad .$$

Taking R from Equation (85) we get

$$\frac{\delta}{R} \simeq \frac{4\sqrt{Dt}}{2\beta\sqrt{Dt}} = \frac{2}{\beta} \quad , \tag{87}$$

where $\beta = \frac{\Delta C}{\rho_g}$.

Thus if β is large, the assumption $\frac{\delta}{R} << 1$ is justified.

The parameter β is often called the Jakob number, Ja, for mass transfer by analogy with a similar dimensionless number describing the driving force for vapor bubble growth in superheated liquid.

Martins[77] has analytically and numerically investigated the relationship between self-similar solution and Plesset-Zwick type solutions. According to him, we can write

$$\tau_M = \frac{1}{3}\left[\xi^2 - 3 + \frac{2}{\xi}\right] \quad . \tag{88}$$

This is a result of Plesset-Zwick type solution applied to the mass-transfer case. Here

$$\tau_M = \frac{4}{\pi}\,\bar{Ja}^2\,\frac{D}{R_o^2}\,t \quad , \qquad \xi = \frac{R}{R_o} \quad ,$$

and $\bar{Ja} = \frac{\Delta C}{\rho_g(p_\infty)}$.

Scriven's solution [Equation (85)] may be written as

$$\xi = \sqrt{3\tau_M} \quad . \tag{89}$$

Thus, for large ξ, Equation (88) approaches Equation (89). Martins has compared results given by Equations (88) and(89) and the numerical solution for $\bar{J}a = 100$ and found good agreement. It was also shown that for $\bar{J}a = 100$ and $\xi > 10$ the difference between ξ predicted by Equation (88) and Equation (89) is negligibly small.

2.5.6 General Relation for Bubble Growth

In many cases of practical interest when large times are involved the diffusion-controlled solution agrees well with observations. For small times the inertial effects are always important. There are situations when both inertial and diffusional effects are important. The problem can be solved numerically or by approximation methods.

One of the approximative methods is based on the thin thermal boundary layer approximation, and solutions have been obtained by Plesset and Zwick,[67] using matched asymptotic expansions, and by Murdock,[86] using an integral technique.

The second method, the result of the work of Mikic, Rohsenhow, and Griffith,[72] is based on interpolation between two limiting solutions, inertia-controlled for small times and diffusion-controlled for large times. It was shown that the interpolation solution agrees well with numerical solutions and experimental observations of vapor bubbles growing in superheated liquids.

The method of Mikic et al. has not been used for bubble growth due to mass diffusion. We have found that their approach will suit our purpose, and therefore, the interpolation model has been developed and is presented next.

For inertia-controlled growth we have

$$\dot{R}_i = \left(\frac{2}{3}\,\frac{p_g - p_\infty}{\rho_\ell}\right)^{1/2} . \qquad (90)$$

For diffusion-controlled growth, when $\beta > 10$--Equation (86)--we have

$$\dot{R}_d = \frac{C_o - C_s}{\rho_g}\, D^{1/2}\, \frac{1}{t^{1/2}} , \qquad (91)$$

because $\sqrt{\frac{3}{\pi}} \sim 1$.

By assuming thermodynamic equilibrium at the bubble wall, one can see from equation of motion [Equation (60)] that the bubble growth rate is a function of concentration at the interface.

For Sievert's law of solubility, which nitrogen and hydrogen obey when in solution with iron, we have

$$C_{eq} = K \sqrt{p_g} \quad ,$$

or

$$p_g = K' C_{eq}^2 \quad , \tag{92}$$

where $K' = 1/K$.

The relationship between C and p for this particular case is depicted in Figure 11. The equilibrium concentration at the bubble wall changes from the initial concentration, C_o, to the final concentration, C_s, which corresponds to the ambient pressure, p_∞. Thus the bubble pressure changes from p_o to p_∞ according to Equation (92). Also, the gas density changes from $\rho_g(p_o)$ to $\rho_g(p_\infty)$ because, assuming ideal-gas behavior

$$\rho_g = \frac{p_g}{R_g T} \quad , \tag{93}$$

where R_g is the gas constant.

We can then say that the bubble growth is a function of normalized concentration driving force, Φ, given by

$$\Phi = \frac{C_i - C_s}{C_o - C_s} = \frac{C_i - C_s}{\Delta C} \quad . \tag{94}$$

Here, $C_i = C_i(t)$ is the interface concentration. Thus both $p_g = f(\Phi)$ and $\rho_g = f(\Phi)$.

We can see that for small times, $t \to 0$, $C_i \to C_o$, and $\Phi \to 1$; for large times, $t \to \infty$, $C_i \to C_s$, and $\Phi \to 0$.

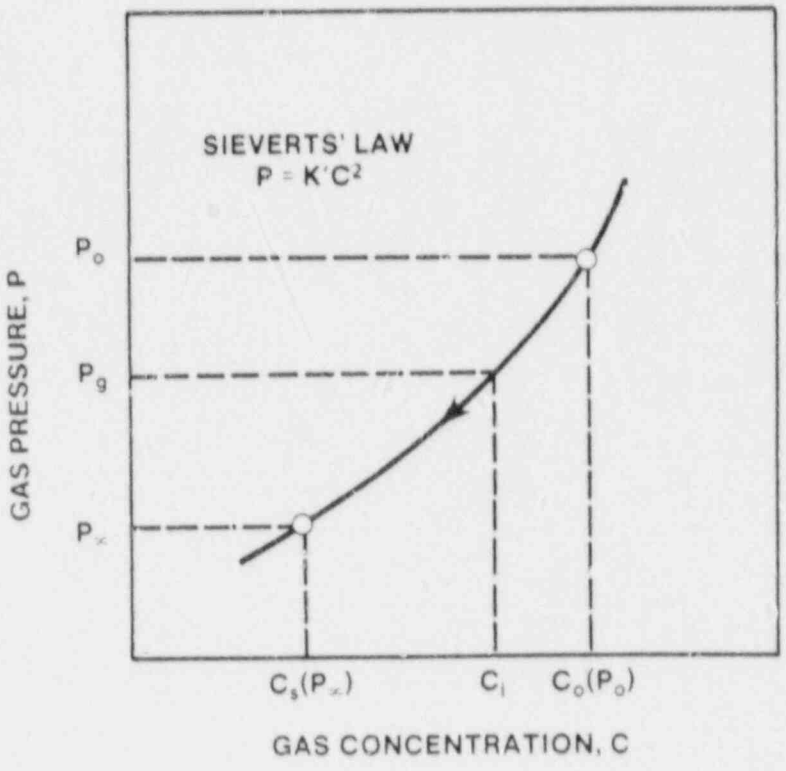

Figure 11. Bubble Pressure as a Function of Gas Concentration at the Bubble Wall for Equilibrium Conditions

In the following development we assume that ρ_g is constant and only $p_g = f(C_i)$. This makes an analytical solution possible, but introduces an error that we will correct later.

We can write Equation (86) in terms of ϕ as follows:

$$\dot{R} = \frac{C_o - C_i}{\rho_g} D^{1/2} \frac{1}{t^{1/2}} = \beta D^{1/2} \frac{1}{t^{1/2}} (1 - \phi) \quad , \qquad (95)$$

where $\beta = \dfrac{C_o - C_s}{\rho_g}$.

Putting $B = \beta D^{1/2}$, which is a constant, (it was assumed that ρ_g is constant) we have

$$\dot{R} = B \frac{1}{t^{1/2}}(1 - \Phi) \quad . \tag{96}$$

When $t \to \infty$, $\Phi \to 0$ and Equation (96) approaches Equation (91).

To express inertia-controlled growth rate in terms of Φ, we use Equation (92). We get

$$p_g = f(C_i) = K'C_i^2 \quad , \tag{97}$$

and

$$p_\infty = f(C_s) = K'C_s^2 \quad . \tag{98}$$

Therefore,

$$p_g - p_\infty = K'C_i^2 - K'C_s^2 = K'\left(C_i^2 - C_s^2\right) \quad . \tag{99}$$

From Equation (94), $C_i - C_s = \Phi\Delta C$, and we have

$$C_i^2 - C_s^2 = \left(C_i - C_s\right)\left(C_i + C_s\right) = \Phi\Delta C\left(C_i + C_s\right) \quad . \tag{100}$$

Since $C_i = \Phi\Delta C + C_s$, we obtain

$$C_i^2 - C_s^2 = \Phi^2(\Delta C)^2 + 2\Phi(\Delta C)C_s \quad . \tag{101}$$

Therefore,

$$p_g - p_\infty = K'(\Delta C)^2\left(\Phi^2 + 2\Phi\frac{C_s}{\Delta C}\right) \quad . \tag{102}$$

Finally, noting that $K' = \frac{p_\infty}{C_s^2}$, Equation (102) becomes after some manipulations

$$p_g - p_\infty = \left[\Delta p_o \quad (\gamma-1)\right] \quad \left\{\Phi^2 + \Phi\,\frac{2}{\gamma-1}\right\} \quad , \tag{103}$$

where

$$\Delta p_o = p_o - p_\infty = p_o(C_o) - p_\infty$$

and

$$\gamma = \frac{C_o}{C_s} = \text{initial supersaturation} \quad .$$

Equation (73) for inertia-controlled growth becomes

$$\dot{R} = A\left(\phi^2 + \phi\frac{2}{\gamma-1}\right)^{1/2} \quad , \tag{104}$$

where

$$A = \frac{2}{3}\left(\frac{\Delta p_o - 2p_\infty(\gamma-1)}{\rho}\right)^{1/2} \tag{105}$$

is a constant depending only on the initial conditions.

Now, consider Equations (95) and (104) as a system

$$\dot{R} = B\,\frac{1}{t^{1/2}}\,(1 - \phi) \tag{95}$$

and

$$\dot{R} = A\left(\phi^2 + \phi\frac{2}{\gamma-1}\right)^{1/2} \quad . \tag{104}$$

The interpolation between these two limiting solutions is carried out by eliminating ϕ from the above system.

By solving for ϕ from Equation (95), and substituting the result in Equation (104), we obtain the following result:

$$\left(\frac{A^2}{B^2}\,t-1\right)\dot{R}^2 - \frac{A^2}{B}t^{1/2}\left(2+\frac{2}{\gamma-1}\right)\dot{R} + A^2\left(1+\frac{2}{\gamma-1}\right) = 0 \quad . \tag{106}$$

Following Mikic et al.,[72] we introduce dimensionless time, t^+, and dimensionless radius, R^+,

$$t^+ = \frac{A^2}{B^2}\,t \quad , \tag{107}$$

and

$$R^+ = \frac{A}{B^2}\,R \quad . \tag{108}$$

In order to simplify the notation, we put

$$E = \frac{2}{\gamma-1} \quad .$$

After solving Equation (106) and expressing the result in a dimensionless form we obtain

$$\frac{dR^+}{dt^+} = \frac{(E+2)(t^+)^{1/2} - [(E+2)^2 t^+ - 4(E+1)(t^+-1)]^{1/2}}{2(t^+-1)} \quad . \tag{109}$$

It may be easily shown that for $t^+ << 1$ the above expression reduces to Equation (73) and for $t^+ >> 1$ to Equation (91).

Integration of Equation (109) yields

$$R^+ = \frac{1}{\gamma-1}\left[\gamma\left(2\sqrt{t^+}+\ln\right)\left|\frac{\sqrt{t^+}-1}{\sqrt{t^+}+1}\right| - 2\sqrt{(t^+-1)+\gamma^2}\right.$$
$$\left. - \gamma\ln\left|\frac{\sqrt{(t^+-1)+\gamma^2}-\gamma}{\sqrt{(t^+-1)+\gamma^2}+\gamma}\right| + C\right] \tag{110}$$

where C is the integration constant evaluated from condition $R^+ = 0$ at $t^+ = 0$

$$C = 2\gamma^2 - 1 + \gamma \ln \left| \frac{\sqrt{\gamma^2 - 1} - \gamma}{\sqrt{\gamma^2 - 1} + \gamma} \right| . \qquad (111)$$

Equation (110) is shown in Figure 12 for three values of γ.

Acceleration of the bubble wall has been calculated by differentiating Equation (109) with a rather lengthy and complicated result. For a rapidly growing hydrogen bubble, the bubble radius is smaller by about 10 percent when the acceleration term is disregarded. In analyses of experiments and reactor accidents, presented in Section 2.6, the acceleration term was not included.

The derivation of the general relation for bubble growth was carried out with the assumption that ρ_g is constant. The gas density is a pertinent factor in growth analysis of diffusion-controlled stage because $\beta = \Delta C/\rho_g$.

As stated earlier, the gas density may be expressed as a function of normalized concentration driving force, Φ, i.e.,

$$\rho_g = f(\Phi) \quad .$$

It was pointed out by Theofanous and Patel,[73] that using growth constant evaluated at ambient pressure leads to significant error for large superheats. They showed, by comparison with experimental data and numerical simulations of vapor bubble growth in superheated liquid, that the method of Mikic et al. is acceptable if changes of gas density during growth period are accounted for. For small superheats, the Mikic et al. solution is satisfactory. Therefore, the general relation for gas bubble growth, given by Equation (110), is useful in cases when changes of gas density during growth period are not too large.

For large changes of gas density, which is the case here, one can easily correct the previous solution in the following way:

The diffusion-controlled growth rate is given by Equation (95)

$$\dot{R} = \beta D^{1/2} t^{-1/2} (1-\Phi)$$

where

$$\beta = \frac{\Delta C}{\rho_g}$$

with

$$\rho_g = \frac{p_g}{RT} \quad ,$$

where p_g is the bubble pressure.

Thus

$$\beta = \frac{\Delta C}{p_g} RT \quad .$$

Using Sievert's law for solubility, $C = Kp^{1/2}$, and relation

$$\Phi = \frac{C_i - C_s}{\Delta C} \quad ,$$

we obtain, after some manipulations,

$$\beta = \frac{C_s^2 \, \Delta C}{\rho_g(p_\infty)(\Phi \Delta C + C_s)^2} \quad .$$

Hence the diffusion-controlled growth rate is given by

$$\dot{R} = B' \frac{1 - \Phi}{(\Phi \Delta C + C_s)^2} \, t^{-1/2}$$

where

$$B' = \frac{C_s^2 \, \Delta C}{\rho_g(p_\infty)} D^{1/2} \quad .$$

The general relation for bubble growth is obtained by eliminating Φ between equations for diffusion- and inertia-controlled growth, i.e., from the following system:

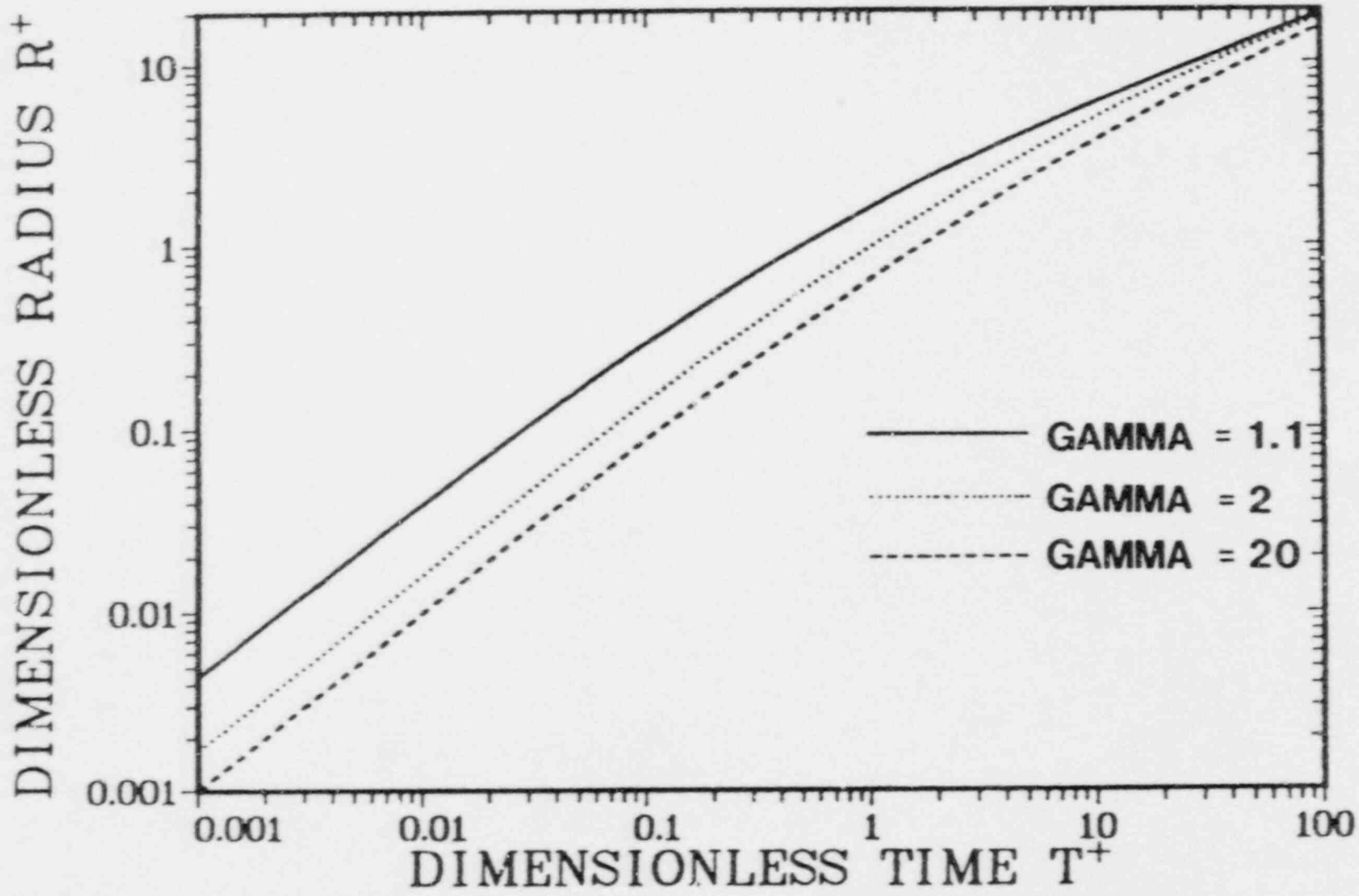

Figure 12. General Relation for Bubble Growth. The bubble growth constant, β, is evaluated for ρ_g = const.

$$\dot{R} = B' \frac{1 - \Phi}{(\Phi \Delta C + C_s)^2} t^{-1/2}$$

and

$$\dot{R} = A \left(\Phi^2 + \Phi \frac{2}{\gamma - 1} \right) t \quad .$$

This system is solved numerically.

We have used, however, a different procedure to account for changes in gas density. This procedure is somewhat faster and gives results that are virtually identical with those obtained by the method outlined above.

We start calculations with $\rho_g = \rho_g(p_\infty) = \rho_g^0$, and the initial growth constant is calculated using this value, i.e., $\beta^0 = \Delta C / \rho_g^0$.

When R_0 has been calculated from Equation (110), the bubble pressure p_g^0 is evaluated from the equation of motion and finally $\rho_g^1 = p_g^0 / R_g T$ is obtained. Then the new growth constant β is calculated based on p_g^1 and the cycle is repeated until

$$\frac{\rho_g i+1 - \rho_c i}{\rho_g i} \leq \epsilon \quad , \tag{112}$$

where ϵ is required accuracy.

The last calculated growth constant is thus the effective growth constant for the entire bubble growth period.

To summarize, a model of bubble growth due to mass diffusion has been developed that covers the entire range of bubble growth, including inertia-controlled and diffusion-controlled stages. An important feature of the model is that it allows us to calculate the bubble pressure as a function of time. This information is needed for fragmentation analysis.

In Section 2.6, we will see that predictions for the nitrogen bubble growth under experimental conditions differ very little from predictions based on Scriven's relation, i.e., for purely diffusion-controlled growth. The situation is,

however, different in the case of the hydrogen bubble growth where inertial effects are important.

2.5.7 Bubble Interaction

When the bubble density in the liquid is large, the bubble interaction during growth process is possible. The assumption that the liquid pressure far from the bubble wall is constant and equal to ambient pressure may not be fulfilled due to the interaction of velocity fields. Also, the assumption that solute concentration far from the bubble is constant and uniform in time may be violated leading to competition among bubbles for available solute. These problems are very difficult and this author is not aware of any studies in this connection except the works of Reiss and La Mer,[87] concerning growth of colloidal particles, and Chahine and Liu,[88] concerning growth of a bubble cluster in a superheated liquid. The latter work is more relevant to our problem. Chahine and Liu developed a singular-perturbation theory for the growth of a cloud of interacting bubbles (under an assumption of low void fraction) in a superheated liquid following a sudden depressurization. It was found that the bubble growth rate is reduced somewhat due to the bubble interaction. This result was expected to remain valid and become more significant for larger void fraction. Thus, it is possible that the present model over-predicts the expansion of the molten jet which in turn would mean that the experimentally determined number density of gas bubbles is underpredicted. We believe, however, that the deviation is not significant since the drop fragmentation calculations (Section 3), in which the number density of gas bubbles is an important parameter, give results which are in reasonably good agreement with experimental data.

The possible reduction of the bubble growth rate in our case would most likely be a result of interaction of velocity fields rather than concentration fields. To show this we propose the following simple method which provides an indication when completion for the solute becomes important.

We assume that the number density of bubbles is N and that the bubbles are uniformly distributed in the liquid. Then the liquid volume per bubble is

$$V_f = \frac{1}{N} \tag{113}$$

and the thickness of the liquid film surrounding the bubble is given by

$$h_f = \frac{V_f}{4\pi R^2} = \frac{1}{4\pi R^2 N} \quad , \tag{114}$$

where R is the bubble radius.

We may say that the competition for the solute is negligible if, for all time, h_f is much larger than the thickness of diffusion boundary layer in which significant concentration gradient takes place.

The thickness of the diffusion boundary layer is

$$\delta \approx \sqrt{D \cdot t} \quad , \tag{115}$$

and we have

$$\frac{\delta}{h_f} << 1 \quad . \tag{116}$$

Substituting Equations (114) and (115) into Equation (116) we get

$$4\pi R^2 N \sqrt{Dt} << 1 \quad . \tag{117}$$

Employing Scriven's formula for R, if $\beta > 10$,

$$R = 2\beta\sqrt{Dt}$$

and we can write

$$4\pi(2\beta)^2 N (Dt)^{3/2} << 1 \quad . \tag{118}$$

The expression for void fraction α [Equation (47), assuming $R_o = 0$] is

$$\alpha = \frac{\frac{4}{3}\pi N R^3}{1 + \frac{4}{3}\pi N R^3} \quad . \tag{119}$$

Upon substituting Equation (85) into Equation (119) we obtain

$$\alpha = \frac{\frac{4}{3}\pi N(2\beta)^3(Dt)^{3/2}}{1 + \frac{4}{3}\pi N(2\beta)^3(Dt)^{3/2}} \quad . \tag{120}$$

Combining Equations (118) and (120) we obtain the simple expression

$$\alpha << \frac{\beta}{1.5 + \beta} \text{ if } \beta > 10 \quad . \tag{121}$$

For small β we have, according to Equation (82)

$$R = (2\beta)^{1/2}\sqrt{Dt} \quad . \tag{87}$$

Proceeding as above, we obtain

$$\alpha << \frac{\sqrt{\beta}}{2 + \sqrt{\beta}} \text{ if } \beta < 10 \quad . \tag{122}$$

The growth constant β, evaluated at 1 atm, is for experiments and reactor conditions about 200 or larger.

Thus from Equation (118) we get

$$\alpha << \frac{200}{200 + 1.5} = 0.99 \quad .$$

The maximum void fraction we expect is $\alpha \sim 0.5$ because at this value the bubbles are very close to each other (assuming that they are arranged on a simple cubic lattice) and breakup of the jet will occur. Therefore, the competition among the bubbles for solute should not be a problem in our case.

Even if it is not relevant to our problem it is interesting to see what happens for small β. Let us consider the following case taken from an article by Birkhoff et al.[69] For water saturated with N_2 at 20°C and heated suddenly to just below the boiling point the growth constant β is equal to 0.021.

From Equation (122)

$$\alpha << \frac{\sqrt{0.021}}{2 + \sqrt{0.021}} = 0.07$$

Thus, for void fractions on the order of a few percent the concentration fields around the bubbles start to interact.

2.6 Experimental Results and Analyses

2.6.1 Introduction

In this section experimental results and analyses are presented for three jet characterization experiments: SPIT-8, JETA-B2 and JETA-B3. Several SPIT and four JETA-B tests have been performed but only relevant tests are used here. Some important observations from the SPIT-8 test were described in Section 1 of this work. In the SPIT-8 test, where nitrogen was used to pressurize the melt generator, the aerosol particle size distribution was measured using samples taken from the aerosol cloud as it drifted over the samples. The debris was not, however, collected and therefore the debris size distribution is not available. The JETA-B tests have been designed to investigate hydrogen supersaturated molten jet and aid in the validation of the jet expansion and fragmentation model. Therefore the debris was collected and size distribution data were obtained by sieve analysis. On the other hand, the aerosol particle size distribution was not measured in the JETA-B tests. The debris and aerosol size distribution data will be described and used in Sections 3.2 and 3.3.

2.6.2 Experimental Results

- Test Apparatus

  The melt generators used in the SPIT and JETA-B tests have been designed to create a high-temperature melt within a pressurized confined volume. A schematic description of the melt generator used for the SPIT series tests is shown in Figure 13. The gas line was connected to an accumulator vessel in order to mitigate the pressure increase during the thermite reaction. The melt crucible was a mild steel pipe section (9-cm inner diameter and about 90 cm long) capped by graphite plates on each end and placed inside the pressure vessel. More detailed information on the melt generator and instrumentation is given by Tarbell et al. in Reference 5.

  The melt generator used in the JETA-B tests was practically identical to that used in the SPIT tests except that the additional gas volume was created between the crucible and the pressure vessel. This modification was

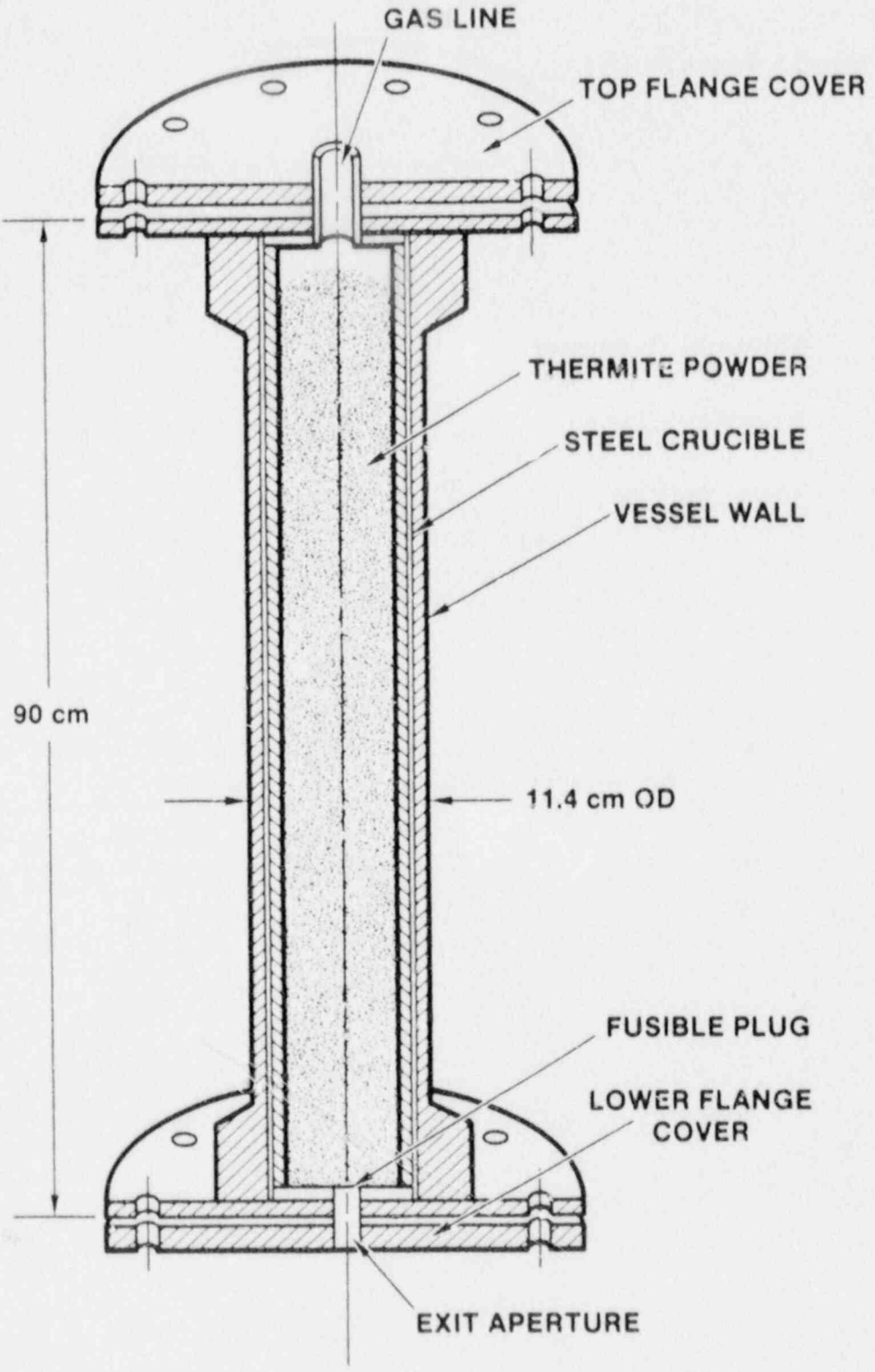

Figure 13. Schematic of Melt Generator

necessary since the accumulator was not used in the JETA-B tests. The total gas volume in the JETA-B melt generator was, however, smaller than in the SPIT generator.

- Instrumentation

Instrumentation used to study the jet behavior and the aerosol and debris size distribution included the pressure transducer, high-speed video camera, flash X-ray, aerosol samplers in the SPIT tests, and a large aluminum pan in the JETA-B tests.

The pressure gauge inserted into the expansion volume of the melt generator measured the gas pressure in the free space above the melt pool. The location and protection of the pressure gauge made it possible to measure the initial gas pressure, the pressure increase during the thermite reaction, and the blowdown history following melt ejection.

The high-speed video camera was used to monitor the appearance and general behavior of the melt stream. However, the brightness of the aerosol cloud around the melt stream prevents resolution of any details other than the outer shape. The behavior within the cloud is not discernable and therefore the X-ray photography was used to characterize the melt stream. The flash X-ray photography was particularly useful because the short exposure time (70 ns) froze the motion of the molten jet. The X-ray units were triggered by means of a breakwire located across the bottom of the fusible plug. Figure 14 shows a schematic of the melt generator and test diagnostics used in the SPIT tests.

The instrumentation used in the SPIT tests for aerosol measurement included a number of cascade impactors and filters.

A large aluminum pan was placed beneath the JETA-B melt generator to collect the debris particles. The pan contained a mixture of water and a water soluble gelatinous material, so that the debris particles could be recovered by dissolving the matrix material. Debris size distribution was determined by sieve analysis.

- Initial Conditions

The melt in the tests was generated by an iron oxide - aluminum metalothermic reaction that yielded iron - aluminum oxide melt, (55 wt percent iron to 45 wt percent aluminum oxide).

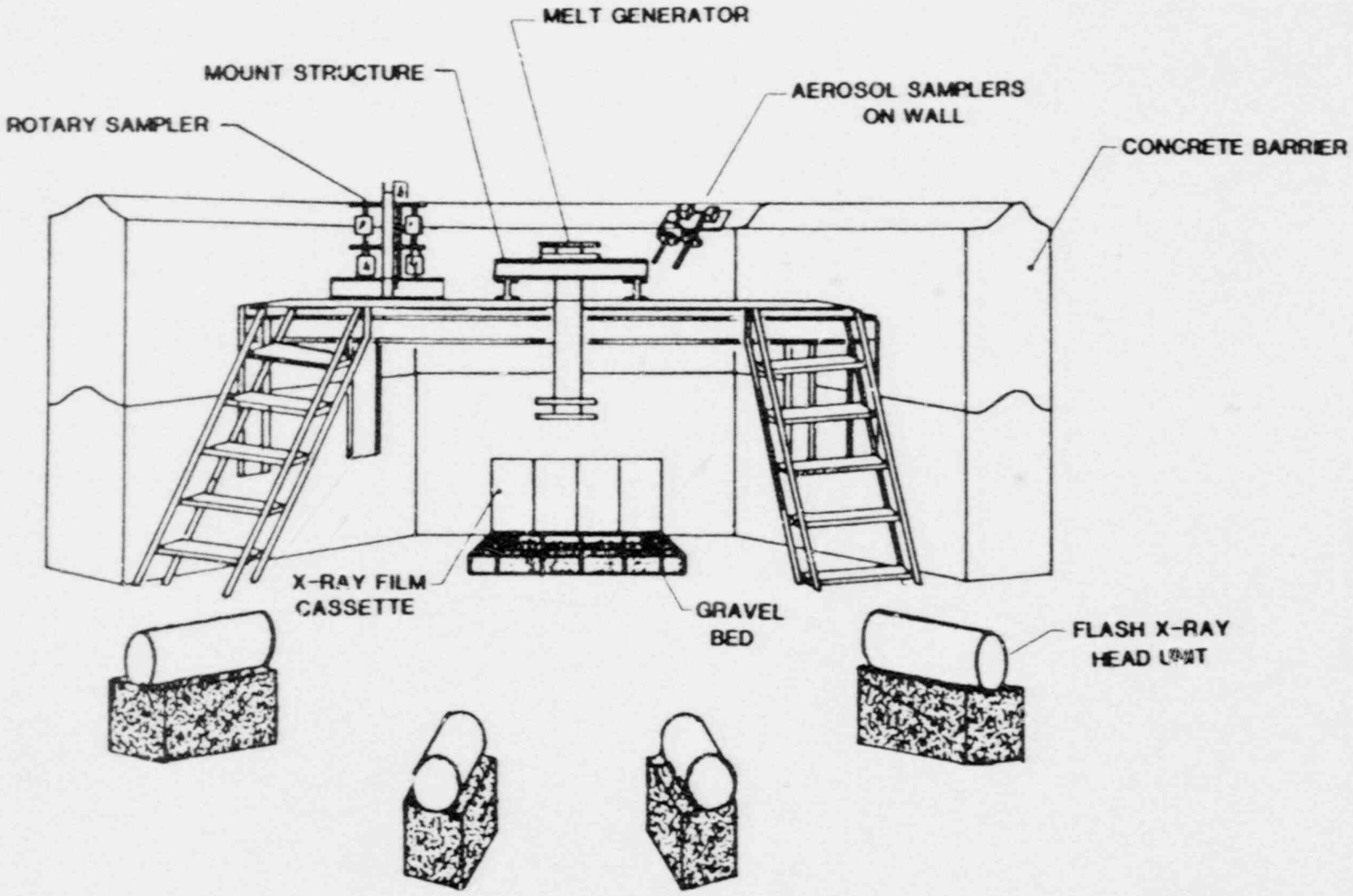

Figure 14. Schematic of Test Facility Showing Relationship of Melt Generator and Test Diagnostics

The initial test conditions for the SPIT-8, JETA-B2 and JETA-B3 tests are summarized in Table 6.

Table 6

Initial Conditions for the SPIT-8, JETA-B2, and JETA-B3 Tests

	SPIT-8	JETA-B2	JETA-B3
Melt Mass [kg]	10,3	10,3	10,3
Thermite Composition	Iron Oxide (Fe_3O_4) - 7.63 kg plus Aluminum (Al) - 2.37 kg		
Melt Composition	Iron (Fe) - 5.66 kg plus Aluminum (Al_2O_3) - 4.64 kg		
Gas	Nitrogen	Hydrogen	Hydrogen
Gas Volume [m^3]	3.0×10^{-2}	1.44×10^{-2}	1.44×10^{-2}
Initial Pressure [MPa]	7.5	0.98	7.2
Fusible Plug Diameter [cm]	2.5	2.5	2.5

The iron oxide and aluminum were obtained in powder form and mixed just prior to the experiments. The iron oxide powder was heated in an oven for about 12 hours at 600°C to drive off absorbed water. This process was designed to minimize gas generation and associated flaring during the thermite reaction.

- Test Procedure

The test procedure is, in summary, the following. The thermite powder is gradually poured into the melt crucible and lightly tamped to improve settling. When the thermite powder is in place, an igniter wire is embedded into the top surface of the powder. After the top flange cover is bolted onto the pressure vessel the melt generator is charged to the desired pressure. Then the thermite reaction is initiated by the igniter. The burn front propagates downward with a typical velocity of 2.5 cm/s.

When the reaction front reaches the bottom of the crucible the fusible plug, located in the lower flange cover of the melt generator, quickly fails and the melt is ejected under pressure. The time period between

ignition of thermite to melt ejection is typically 15 to 30 s.

- Experimental Observations

Figure 15 is a series of photographs taken during a typical melt ejection test (pressurized with nitrogen at 4.1 MPa). The times stated are from the first appearance of the melt stream. The melt jet at 0.05 s is highly luminous, divergent cone (about 40° half angle) emanating from the vessel. The material within the cloud appears to be vaporized melt. On the following photographs the vapor cloud expands, darkens, and finally the aerosol cloud completely obscures the test apparatus.

The flash X-ray photographs of the melt jets of the SPIT-8, JETA-B2 and JETA-B3 tests are shown in Figures 2, 6, and 7, respectively.

The X-ray photograph of the SPIT-8 test shows slightly over half of the melt jet 30 ms after start of ejection. The length of the jet portion shown on the photograph is 20 cm. The half-angle of the jet stream is about 10°. A small area, 71 x 71 mm, of the X-ray image 15 cm downstream the orifice was computer processed.

Figure 16 shows some results of this process. An average calculated area of gas "bubble" is 2.1 mm^2. Assuming that the disrupted jet consists of spherical melt droplets, their average size is estimated to be five to seven times the average "bubble" size. This gives the average size of the melt droplet on the order of 2 mm.

The X-ray photographs of the JETA-B2 and JETA-B3 tests, shown in Figures 6 and 7, were taken 15 ms after start of ejection. The length of the portion of the jets shown in the photographs is 30 cm. The distance from the top edge of the photographs to the melt generator exit is 8 cm. Only about half of the JETA-B2 melt jet is shown (the jet axis is parallel to the right edge of the page). The half-angle of the jets is 20° and 28° for JETA-B2 and JETA-B3, respectively. Not surprising, expansion and disruption of molten jets in JETA-B2 and JETA-B3 tests are larger than in SPIT-8 test. This is in agreement with observations from stream degassing of liquid metals and with calculations presented in Section 2.6.3. The estimated (from the photograph) size of the melt fragments 20 cm from the orifice is on the same order for both JETA-B2 and SPIT-8 tests. The fragments seem to be smaller in the JETA-B3 test. As mentioned earlier, the debris size distribution data for the JETA-B tests is presented in Section 3.2.

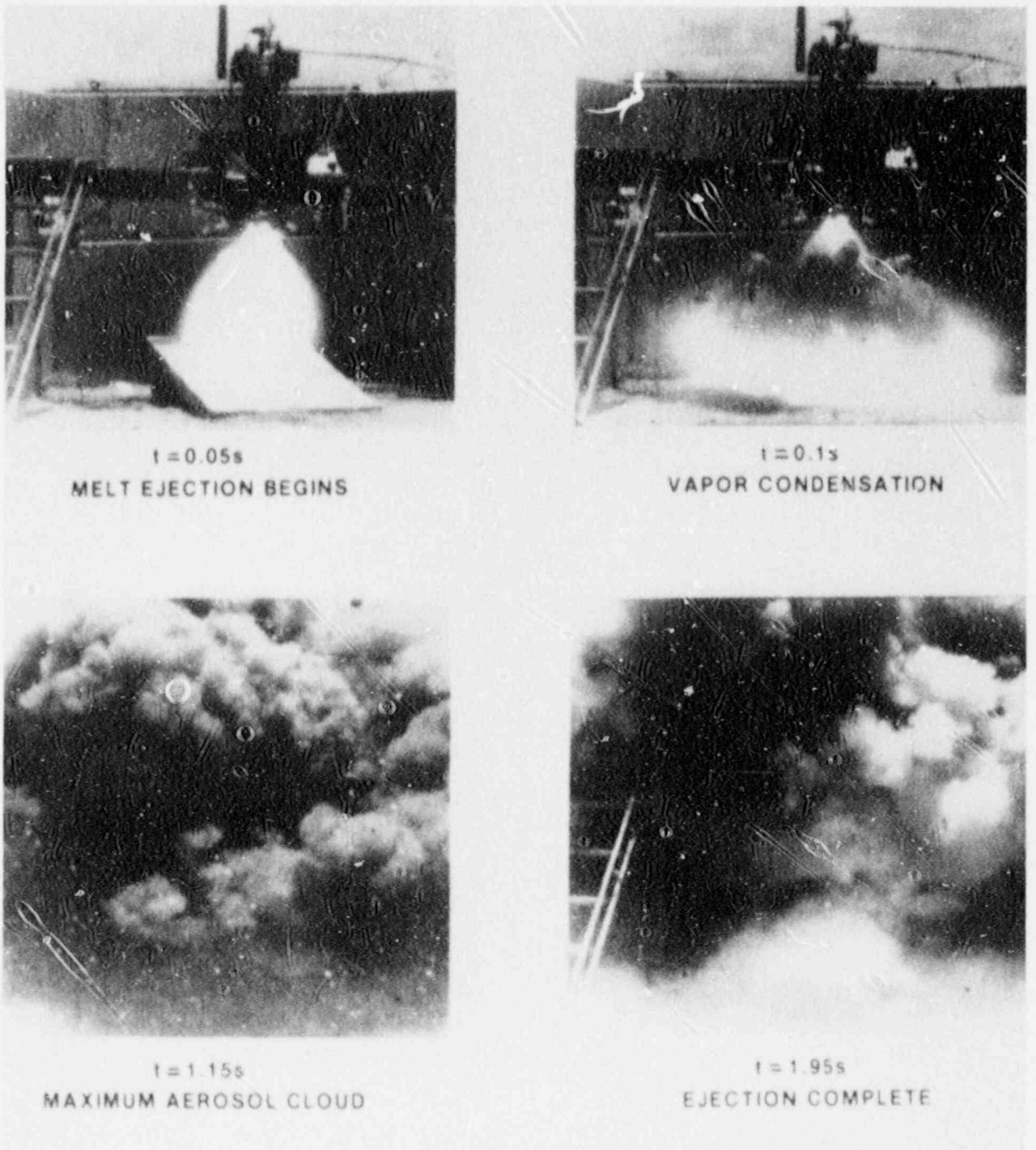

Figure 15. Sequential Photographs of the Events of a Typical Melt Ejection Experiment

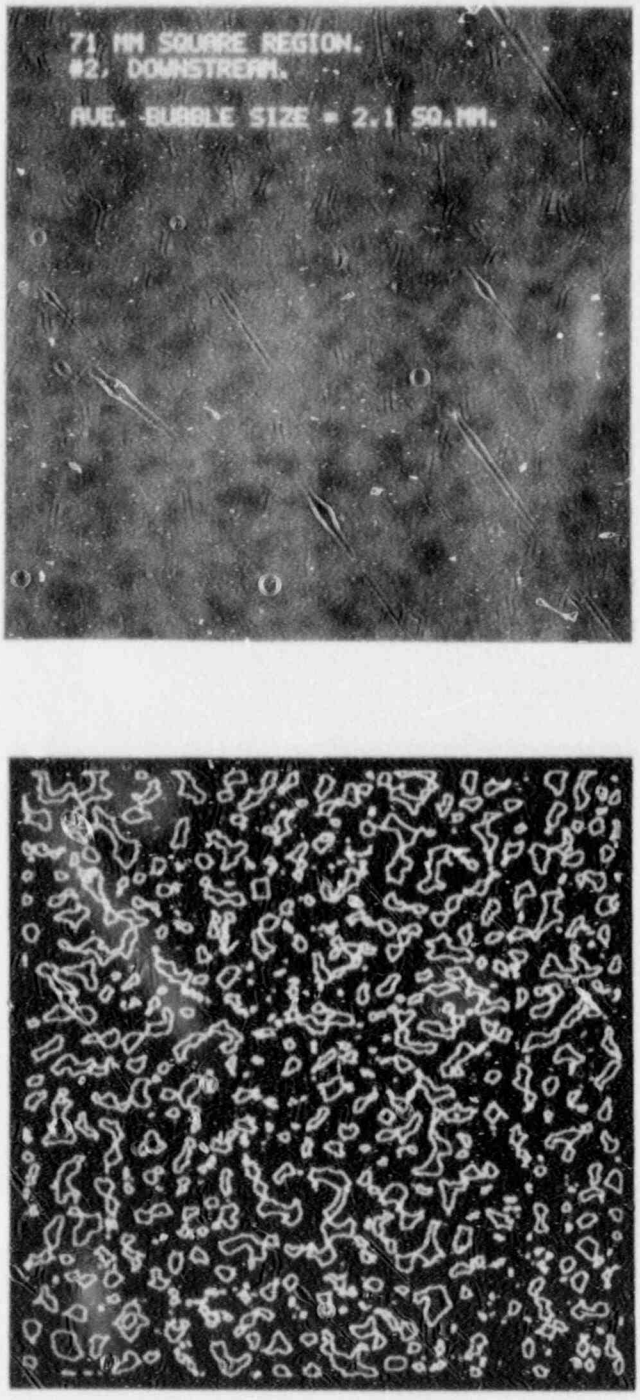

Figure 16. Computer Processed Image of the SPIT-8 Melt Jet 15 cm Downstream From the Orifice

2.6.3 Analyses

2.6.3.1 Introduction

The experimental observation described in the preceding section will be used to determine the number density of gas bubbles in the melt jet and to verify model predictions. The number density of gas bubbles will be determined for the SPIT-8, JETA-B2 and JETA-B3 tests. Calculations of the jet void fraction and the jet radius are presented only for the SPIT-8 test. Predictions for the JETA-B tests are qualitatively the same and very similar to predictions for the reactor accidents which are presented in Section 2.7.

We will assume that the initial jet void fraction, α_o, is negligible, because the equilibrium bubble radius is very small for the experimental and reactor conditions. For example, when the equilibrium gas pressure is 7.5 MPa, we get

$$R_o = \frac{2\sigma}{\Delta p} = \frac{2 \times 1.0}{74 \times 10^5} = \sim 3 \times 10^{-7} \text{ m}$$

Here the surface tension of liquid iron at 1550°C containing a small amount of oxygen was used.[52]

The mixture density, $\bar{\rho}$, and the volume fractions of melt components, z_i, are calculated from the following formulas:

$$\bar{\rho} = \frac{1}{\sum_i x_i / \rho_i} \qquad (123)$$

and

$$z_i = \frac{\bar{\rho}}{\rho_i} x_i \quad . \qquad (124)$$

Here x_i is the mass fraction and ρ_i the density of component i.

The solubility of hydrogen and nitrogen in liquid iron obeys Sievert's law[89] and their solutions are described by the following expressions:

$$H_2 \rightleftarrows [H] + [H]$$

$$N_2 \rightleftarrows [N] + [N] \quad .$$

The reaction constant is given by

$$K' = \frac{a_{H_2}^2}{p_{H_2}} \quad ,$$

where a_{H_2} is the activity of hydrogen in iron and P_{H_2} is the hydrogen partial pressure above the melt. Assuming that activity is proportional to concentration we can write

$$[\%H]^2 = K' p_{H_2} \quad ,$$

that is,

$$[\%H] = K\sqrt{p_{H_2}} \quad , \tag{125}$$

where $K = (K')^{1/2}$.

The identical expression is obtained for nitrogen:

$$[\%N] = K\sqrt{p_{N_2}} \quad . \tag{126}$$

The solubility is also a function of temperature. According to Reference 6, we have

$$\log [10^4 \%H] = - \frac{1637}{T} + 2.3126 + \frac{1}{2} \log p_{H_2} \tag{127}$$

and

$$\log [\%N] = - \left[\frac{188}{T} + 1.246\right] + \frac{1}{2} \log p_{N_2} \quad . \tag{128}$$

Here P is in atms, T in Kelvin, and concentration in weight percent. Equations (127) and (128) are used in the model.

Powers[6] has shown that gas content in iron melts approaches equilibrium concentrations in a few seconds under experimental conditions, see Figure 17.

The melt is assumed to be an inhomogeneous mixture of pure iron and in experiments, aluminum oxide or in the reactor case, other components of the corium. This assumption is an extrapolation of the results of the elemental analyses of the particles from the SPIT tests.

The dependence of gas diffusivity on the temperature has been accounted for in the following way. According to Richardson,[40]

$$D = D_o e^{-\frac{E_o}{RT}} , \qquad (129)$$

where E_o is the activation energy for the diffusion step and D_o is independent of temperature.

For hydrogen in liquid iron at 1600°C, the following values are reported:[40]

$$D_o = 3.2 \times 10^{-3} \frac{cm^2}{s}$$

$$E_o = 3.3 \frac{kcal}{mol} .$$

Values of D_o and E_o for nitrogen in the liquid iron have not been found. Therefore, it was assumed that an increase of nitrogen diffusivity with temperature is proportionally the same as for hydrogen.

It was shown in Reference 5 that the adequate estimate of the jet velocity is obtained using Bernoulli's equation with assumption that the discharge coefficient of the orifice is unity.

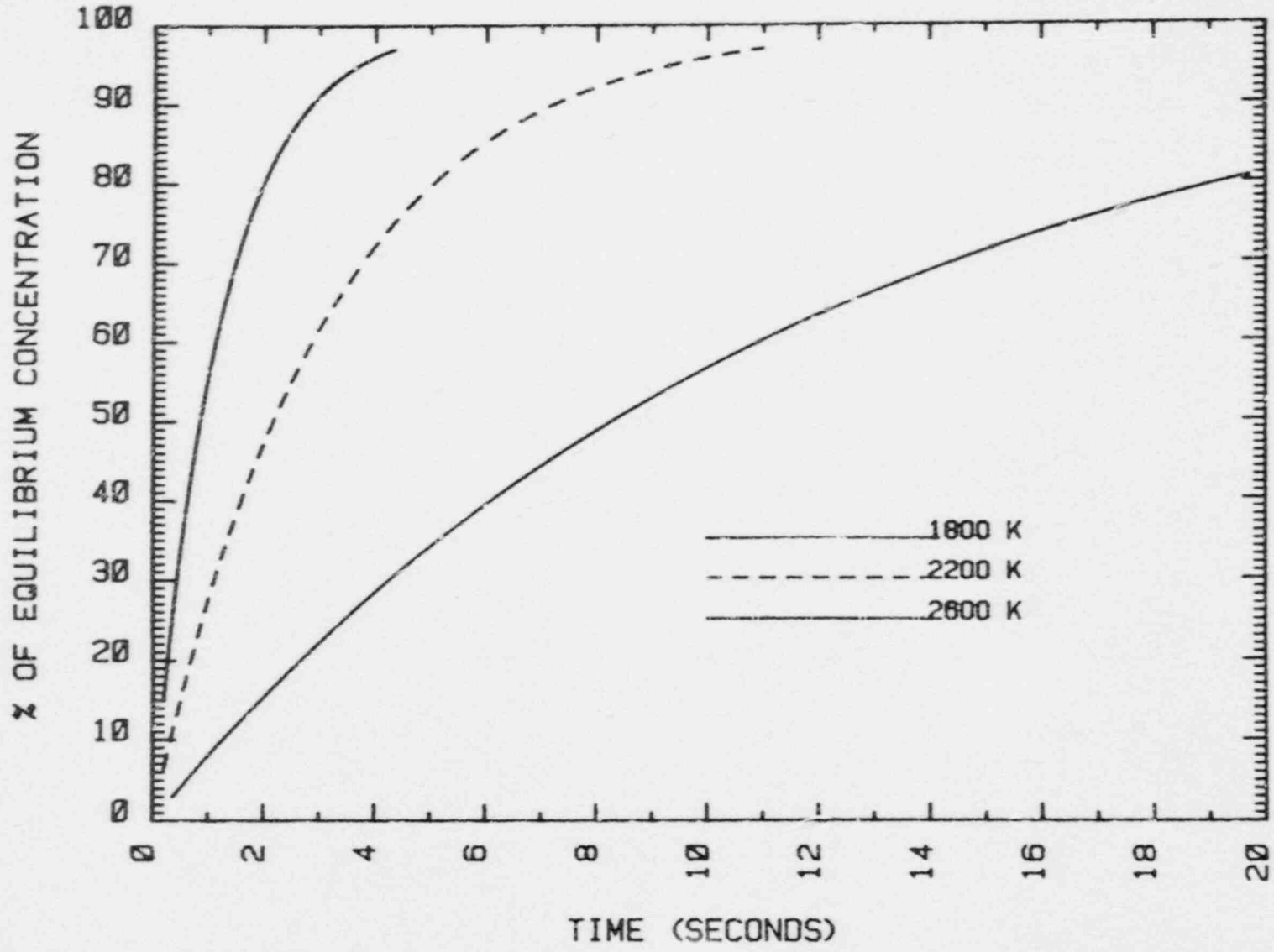

Figure 17. Approach to Equilibrium Nitrogen Content in Iron Melts of Various Temperatures [Reference 6]

Thus

$$V = \left[\frac{2\,(p_o - p_\infty)}{\bar{\rho}}\right]^{1/2} , \qquad (130)$$

where p_o = pressure in the melt generator at the moment of melt ejection,

p_∞ = ambient pressure (0.086 MPa in Albuquerque),

$\bar{\rho}$ = mixture density.

The contribution of iron vapor pressure to the bubble pressure was neglected in the bubble growth calculations.

2.6.3.2 Model Results

The melt composition and some of its properties are given in Table 7. Table 8 contains some important parameters and dimensionless numbers for the conditions of the SPIT-8 test. Corresponding data for the conditions of the JETA-B tests are not given here; they are very similar to the data for the reactor cases presented in Section 2.7.

The effect of surface kinetics on nitrogen bubble growth was estimated by the method proposed by Szekely and Fang.[79] The surface kinetics effects are important when the bubble is small, and therefore should be compared with inertial effects. This comparison is made by calculating the dimensionless parameter $\bar{B}_{IK}$. In order to do this, we have to determine the interface mass transfer coefficient, α. According to Reference 29, the rate constant for the iron-nitrogen system, when the oxygen mass fraction in iron is below 10^{-4}, is

$$k(T) = 3.52 \times 10^5 \exp(-31900/RT)\ [cm/s] ,$$

where R, the universal gas constant, is 1.99 cal/mol K.

For T = 2800 K, we obtain k = 11.5 m/s. Hence

$$\alpha = k\rho_\ell = 11.5 \times 6156 = 7.0 \times 10^4\ kg/m^2s$$

Table 7

Composition and Properties of the Thermite Melt at 2800 K

		Component		
		Fe		Al_2O_3
Mass fraction	[%]	55		45
Volume fraction	[%]	34		66
Density	[kg/m^3]	6156		2627
Mixture density	[kg/m^3]		3843	
Coefficient of diffusivity	[m^2/s]			
Nitrogen		1.4×10^{-8}		
Hydrogen		1.7×10^{-7}		
Surface tension	[N/m]	1.2		0.36
Viscosity	[cP]	2.0		4.6

The parameters $\bar{B}_{IK}$ (also $\bar{B}_I$ and $\bar{B}_K$) are given in Table 8. Since $\bar{B}_{IK}$ is very large, the surface kinetics effects may be neglected when compared to the inertial effects.

It was assumed that the oxygen concentration was very low, which is probably not the case for the SPIT melts. According to Reference 29, the nitrogen removal rate constant, k, decreases with increasing oxygen concentration. Thus the "real" $\bar{B}_{IK}$ may be smaller but still, we believe, large enough to disregard surface kinetics effects for the SPIT conditions.

The growth of nitrogen bubbles in the SPIT tests is mainly diffusion controlled, as illustrated in Table 9.

Table 8

Values of Some Relevant Parameters and Dimensionless Numbers From the SPIT-8 Test

P_{system}	[Pa]	75×10^5
T_{melt}	[°K]	2800
$p_o(C_o)$	[Pa]	75×10^5
p_∞	[Pa]	0.86×10^5
$R_o = \frac{2\sigma}{\Delta p}$	[m]	2.7×10^{-7}
$C_o = C(p_o)$	[kgN/m^{3}Fe]	26.0
$C_s = C(p_\infty)$	[kgN/m^{3}Fe]	2.8
$\Delta C = C_o - C_s$		23.2
$\gamma = C_o/C_s$		9.3
$\bar{\beta} = \bar{J}a = \frac{\Delta C}{\rho_g(p_\infty)}$		223
$G_I = \frac{R_o^2 \Delta p}{\rho_\ell D^2}$		4.5×10^5
$\bar{B}_I = \frac{\bar{J}a^2}{(G_I)^{1/2}}$		59
$G_K = \frac{\alpha R_o \Delta C}{D \rho_g(p_\infty)}$		3.1×10^8
$\bar{B}_K = \frac{\bar{J}a^2}{G_K}$		1.6×10^{-4}
$\bar{B}_{IK} = \frac{\bar{B}_I}{\bar{B}_K}$		3.7×10^5

Where $\Delta p = p_o - p_\infty$

Table 9

Comparison Between Diffusion-Controlled and General Relation Models of Nitrogen Bubble Growth in Molten Iron for the SPIT-8 Conditions, 1 ms After Start of Rapid Growth. Ambient pressure is 0.086 MPa.

			General Relation $R^+ = f(t^+)$			
	Diffusion Controlled		Based on $\rho_g(p_\infty)$		Based on $\rho_g = f(\phi)$	
	p_{N_2} (MPa)		p_{N_2} (MPa)			
Bubble Parameter	7.5	16	7.5	16	7.5	16
R [mm]	1.70	2.55	1.59	2.40	1.51	2.15
dR/dt [m/s]	0.84	1.20			0.87	1.20
p [MPa]	0.08	0.086			0.090	0.094
ρ [kg/m^3]	0.104	0.104			0.11	0.12

In the case of hydrogen bubble growth in the JETA-B tests, the inertia effects are very important. If they were neglected, the jet expansion would be significantly overpredicted and the bubble overpressure could not be calculated. The importance of the inertia effects for hydrogen bubble growth is illustrated in the next section.

The half-angle of the melt jet was calculated as a function of number density of gas bubbles for the SPIT-8, JETA-B2 and JETA-B3 tests. The result is presented in Figure 18. Taking the observed half-angle of the jets we obtain the interesting result that the number density of gas bubbles in all three tests is approximately 10^8.

This result could imply that the nucleation rate is very high approaching, practically the same in all cases, maximum rate determined by pre-exponential factor in expression for nucleation rate [see Equation (27)]. In this case the density of microbubbles is so high that they coalesce and form a population of larger bubbles. The number of bubbles in this population would then correspond to the number density of bubbles obtained from experiments.

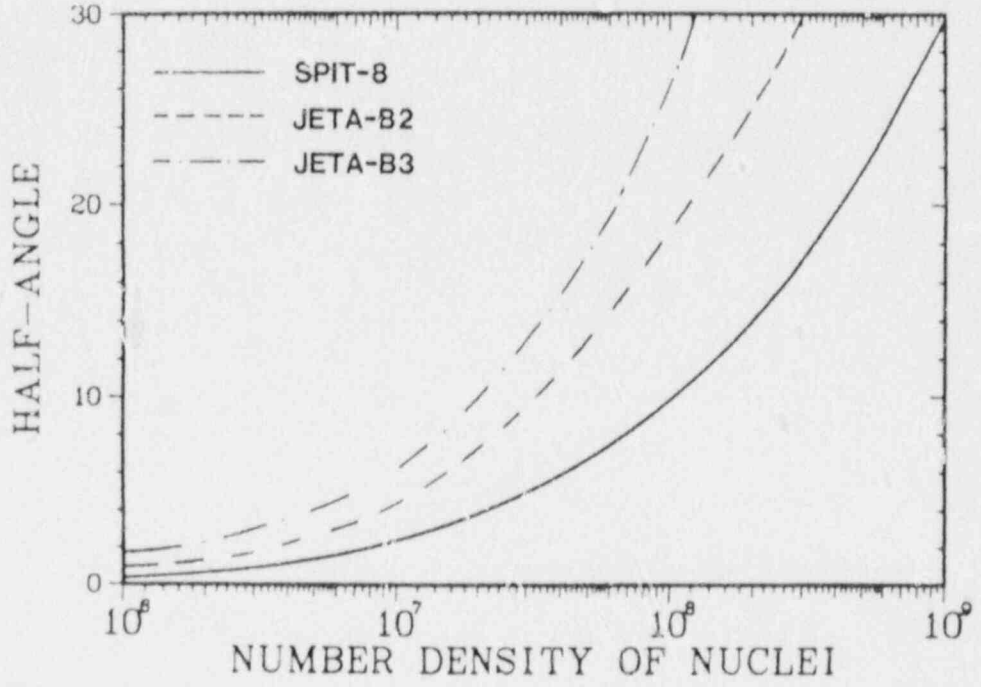

Figure 18. The Half-Angle of the Jet as a Function of Number Density of Nuclei

Considering that gas solubility in aluminum oxide is very small,[6] the number density of gas bubbles per m^3 of liquid iron is

$$N_{Fe} = \frac{N}{Z_{Fe}} \tag{131}$$

where Z_{Fe} is the volume fraction of iron in the melt. Thus, N_{Fe} is approximately 3×10^8. This number is of the same order of magnitude as that reported by Mizoguchi et al.,[35] for oxygen bubble nucleation in molten silver under stream degassing conditions.

Fragmentation calculations performed for another stream degassing experiment,[36] in which the fragment size (but not the jet spread angle) was reported, indicate that N lies in the neighborhood of $10^9/m^3$.

Figures 19 and 20 show the jet void fraction and the nondimensional jet radius for the SPIT-8 test as a function of the distance from the point of inception of rapid bubble growth. For our purpose this distance may be considered as

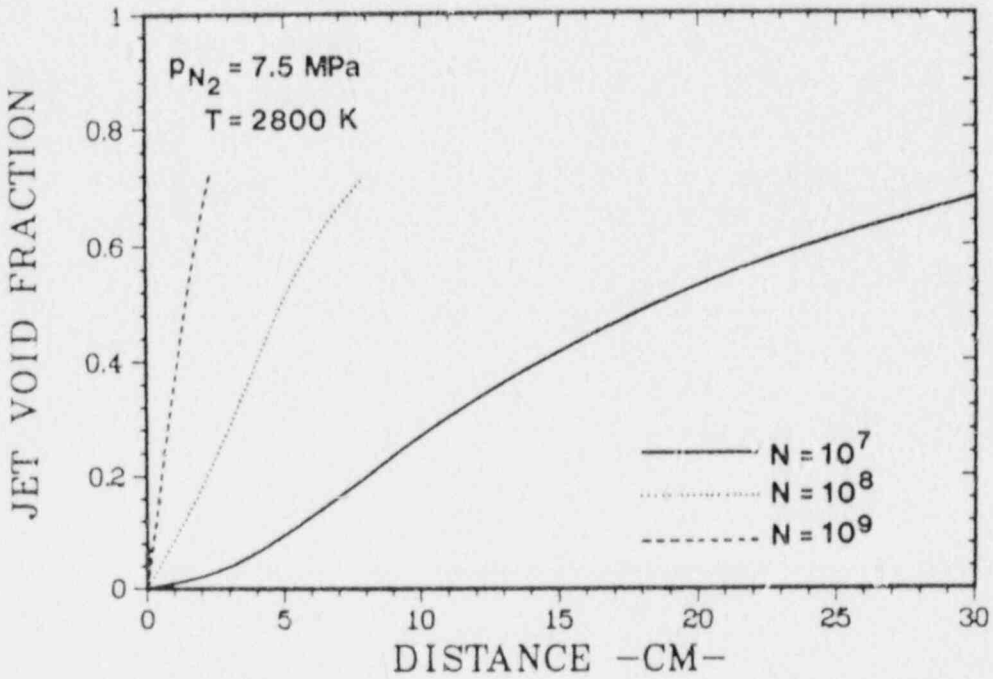

Figure 19. SPIT-8 Test. Jet void fraction as a function of the distance from the point of inception of rapid bubble growth.

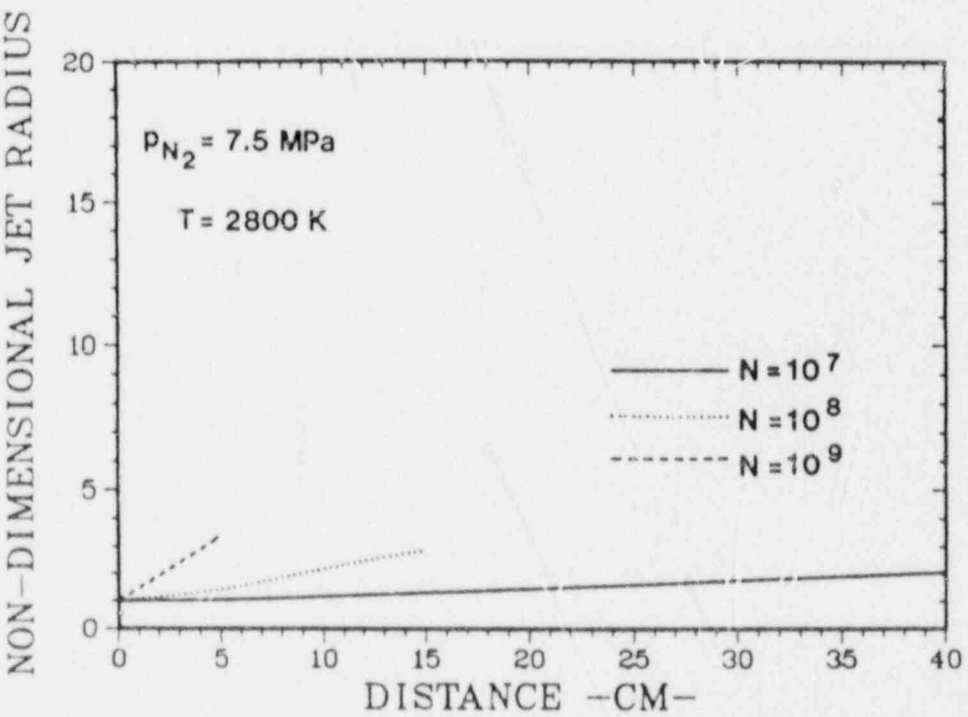

Figure 20. SPIT-8 Test. Nondimensional jet radius as a function of the distance from the point of inception of rapid bubble growth.

a distance from the melt generator exit. We see that void fraction is significant 20 cm from the orifice which is in qualitative agreement with observations. The jet radius is about three times the initial radius at 15 cm from the orifice (for $N = 10^8$). The curves in Figure 19 are truncated at the distance where void fraction is approximately 50 percent.

Having determined the number density of gas bubbles, the average size of the molten droplet produced by the primary jet breakup may be calculated:

$$\frac{\pi}{6} D^3 \approx \frac{1}{N} \quad . \tag{132}$$

Therefore

$$D \sim \left(\frac{6}{\pi N} \right)^{1/3} \quad , \tag{133}$$

where D is the droplet diameter.

Taking $N = 10^8$ we obtain $D = 2.7$ mm. This result is in reasonable agreement with observations.

2.7 Model Predictions for Reactor Case

Extrapolation of the experimental results to reactor accident conditions requires consideration of only hydrogen solubility in the iron component of the corium melt. Neglecting other gases and other melt components could result in the underprediction of jet expansion and breakup. However, this underprediction should be negligible considering that solubility of other gases in iron and other melt components is two to three orders of magnitude smaller than solubility of hydrogen in liquid iron.[6] Furthermore, the diffusivity of hydrogen in liquid iron is at least 1 order of magnitude larger than diffusivity of other gases in liquid metals.

The melt composition and some of its properties are given in Table 10.

Parametric calculations have been performed for a high pressure reactor accident scenario. It is assumed that the primary system pressure is 16 MPa and the containment pressure is 0.1, 0.2, or 0.4 MPa. The number of gas bubbles in the core melt mixture was assumed to be $6 \times 10^7/m^3$. This number was obtained by extrapolation of experimental results to reactor conditions assuming that the number of nuclei in the iron component of the melt is the same as in the experiments and accounting for the fact that the volume fraction of iron phase in the melt is different for each

Table 10

Corium Composition and Properties at 2500 K

	Component			
	UO_2	Fe	Zr	ZrO_2
Mass fraction [%]	67.2	16.4	8.2	8.2
Volume fraction [%]	56	21	11	12
Density (kg/m^3]	$10.0x10^3$	$6.4x10^3$	$6.5x10^3$	$5.8x10^3$
Mixture density		8365		
Coefficient of hydrogen diffusivity [m^2/s]		$1.7x10^{-7}$		
Surface tension [N/m]	0.5	1.2	1.4	
Viscosity [cP]	4.6	2.0		

case. The gas concentration in the melt is determined by the equilibrium hydrogen partial pressure above the melt, chosen to be 3.2, 6.4, 9.6, or 16 MPa. These hydrogen pressures can exist locally (at the melt surface) due to the reaction of various metallic components of the melt with the steam. The hydrogen pressure may be written as

$$p(H_2) = \frac{p_{tot}}{1 + 1/k} ,$$

where p_{tot} is the total system pressure [$p_{tot} = p(H_2) + p(H_2O)$] and k is the ratio between the partial pressures of hydrogen and water vapor, $p(H_2)/p(H_2O)$. This ratio is obtained from the chemical equilibrium equation at the given temperature. The evaluation is simple for the reactions that involve only pure condensed phases. For instance when Zr, Fe, or Ni react with H_2O at 2500 K, the values of k are, approximately, 10^4, 2, and 0.01, respectively. This covers the range of hydrogen pressures used in the parametric study. The situation is more complicated if the reacting components are in solution. It should be

pointed out here that substantial hydrogen pressures may exist globally in the primary system due to the oxidation of Zr and Fe.

Some important parameters and dimensionless numbers pertinent to the problem here considered are given in Table 11. Table 12 shows some bubble parameters calculated with Scriven's formula and general relation for the bubble growth. We see that, as mentioned earlier, inertial effects are very important.

Model predictions for the reactor case are presented in Figures 21 through 25. Figures 21 and 22 show the jet void fraction and nondimensional radius as a function of the distance from the point of inception of rapid bubble growth. For our purpose this distance may be considered as a distance from the reactor pressure vessel. Containment pressure is 0.2 MPa, which is a pressure expected prior to reactor vessel meltthrough for a TMLB' sequence in a large, dry PWR containment.[90]

The expansion of the jet is much more vigorous than in the SPIT-8 case because of the significantly higher diffusivity of hydrogen in liquid iron and lower density compared to nitrogen. The jet void fraction reaches about 50 percent within a few centimeters from the point of inception of rapid bubble growth. Thus, bubble bursting and jet fragmentation are expected to occur within a very short distance from the reactor pressure vessel.

The containment pressure, which is a pertinent parameter, has a strong effect on the jet expansion via its role in the bubble dynamics.

Figures 23 and 24 show the effect of containment pressure on jet behavior. The number density of nuclei is again 6×10^7. The equilibrium partial pressure of hydrogen is 6.4 MPa and containment pressures are 0.1, 0.2, and 0.4 MPa.

The jet expansion is significantly hampered at the elevated containment pressures, because the bubble growth constant decreases as gas density increases. However, even at the containment pressure of 0.4 MPa the void fraction reaches 50 percent about 15 cm from the point of inception of rapid bubble growth.

In reactor safety considerations it is important to inquire what is the jet radius when the jet contacts the reactor cavity floor. We cannot use the present model for more exact predictions of the jet, or spray, behavior in the breakup and fragmentation zone.

It is possible, however, to estimate the jet radius after the breakup point using the present model. The spread angle

Table 11

Reactor Case.
Values of some parameters and dimensionless numbers.
Containment pressure is 0.1 MPa.

	Hydrogen Partial Pressure (MPa) 3.2	6.4	16.0
$p_o(C_o)$ [MPa]	3.2	6.4	16
$R_o = \frac{2\sigma}{\Delta p}$ [m]	6.5×10^{-7}	3.2×10^{-7}	1.3×10^{-7}
C_o [kgH/m^{3}Fe]	1.59	2.25	3.56
C_s [kgH/m^{3}Fe]	0.28	0.28	0.28
$\Delta c = C_o - C_s$ [kgH/m^{3}Fe]	1.31	1.97	3.28
$\gamma = C_o/C_s$	5.66	8.00	12.60
$\bar{\beta} = \bar{J}a = \frac{\Delta C}{\rho_g(p_\infty)}$	135	203	338
$G_I = \frac{R_c^2 \Delta p}{\rho_\ell D^2}$	5420	2669	1112
$\bar{B}_I = \frac{\bar{J}a^2}{G^{1/2}}$	248	798	3430

where $\Delta p = p_o(C_o) - p_\infty$

Table 12

Comparison Between Diffusion-Controlled and General Relation Models of Hydrogen Bubble Growth in Molten Iron for the Reactor Accident Conditions, 1 ms After Start of Rapid Growth. Containment pressure is 0.1 MPa.

			General Relation $R^+ = f(t^+)$			
	Diffusion Controlled		Based on $\rho_g(p_\infty)$		Based on $\rho_g = f(\Phi)$	
	P_{H_2} (MPa)		P_{H_2} (MPa)			
Bubble Parameter	3.2	16	3.2	16	3.2	16
R [mm]	3.52	8.81	2.85	6.76	2.30	4.34
dR/dt [m/s]	1.76	4.41			1.50	2.59
p [MPa]	9.7×10^{-3}	9.7×10^{-3}			0.13	0.18
ρ [kg/m^3]	9.7×10^{-3}	9.7×10^{-3}			1.26×10^{-2}	1.67×10^{-2}

of the fragmented jet is assumed to be equal to the spread angle at the moment of jet breakup and this angle can be calculated with the present model. The actual spray angle may be larger due to the radial velocity that jet fragments will acquire after bubble bursting.

The extrapolated nondimensional jet radius, based on the jet spread angle at the point where void fraction is 50 percent, is shown in Figure 25. The number density of bubbles is again 6×10^7, the containment pressure is 0.2 MPa, and the equilibrium partial pressures of hydrogen are 3.2, 6.4, 9.6, and 16 MPa. The distance between the bottom of the reactor pressure vessel and the cavity floor is, for Zion containment, about 4.5 m. The spray radius is in the range of 0.8 m to 2.6 m for the hydrogen equilibrium pressures here considered. Hence, the diameter of the fragmented jet at the level of the reactor cavity floor is predicted to be 40 to 130 times the discharge diameter.

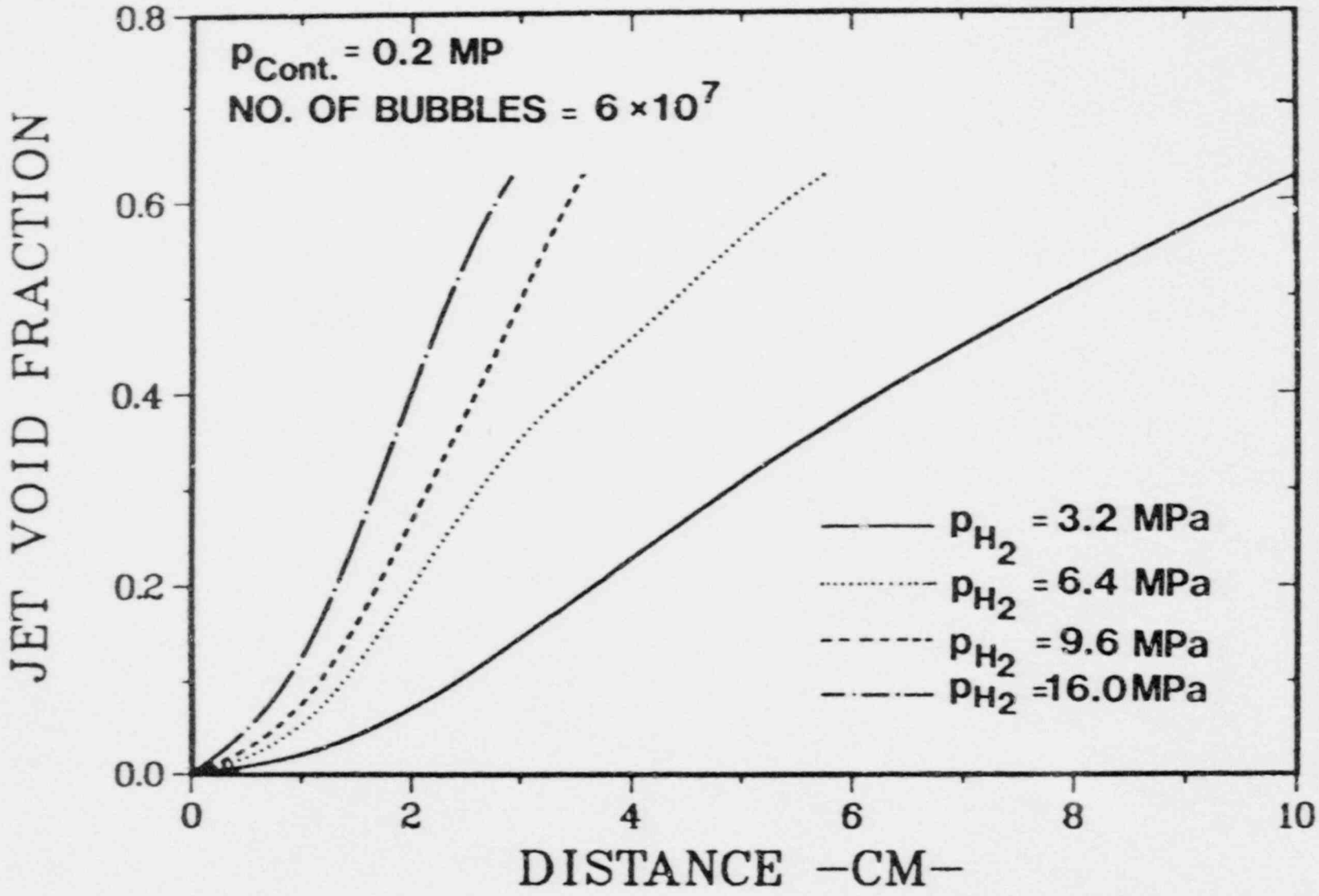

Figure 21. Reactor Case. Jet void fraction as a function of the distance from the point of inception of rapid bubble growth. Hydrogen equilibrium pressure is a parameter.

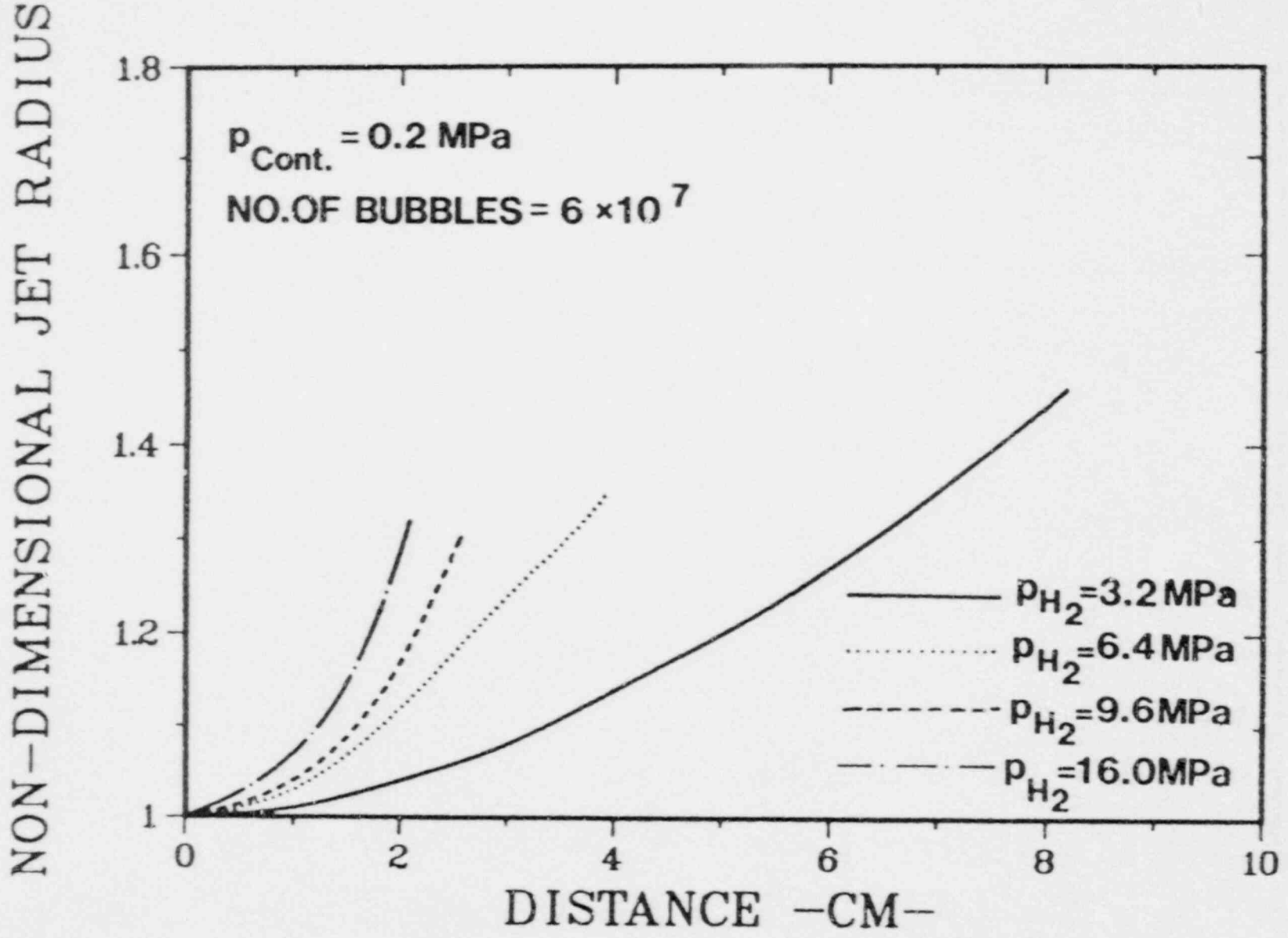

Figure 22. Reactor Case. Nondimensional jet radius as a function of the distance from the point of inception of rapid bubble growth. Hydrogen equilibrium pressure is a parameter.

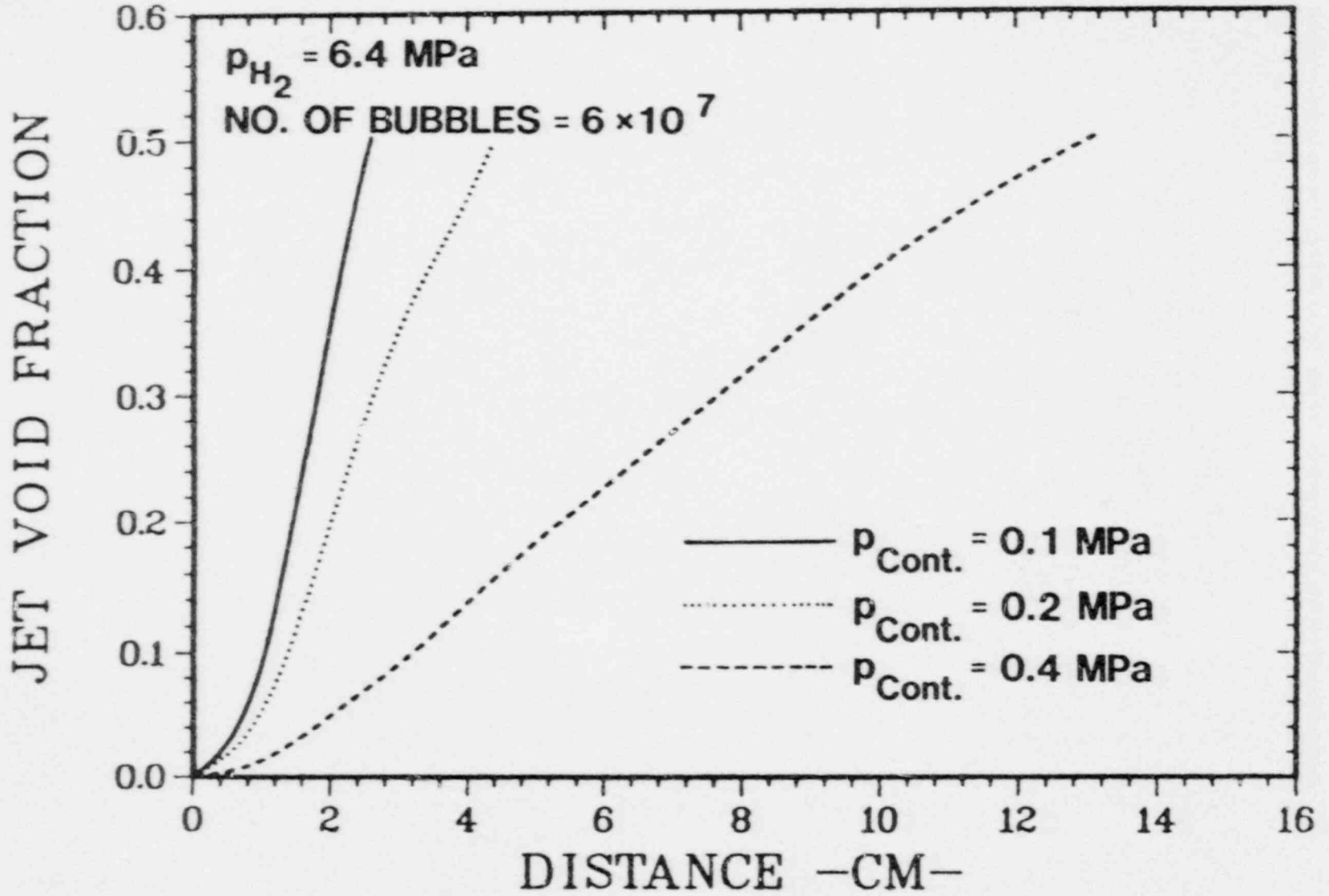

Figure 23. Reactor Case. jet void fraction as a function of the distance from the point of inception of rapid bubble growth. Containment pressure is a parameter.

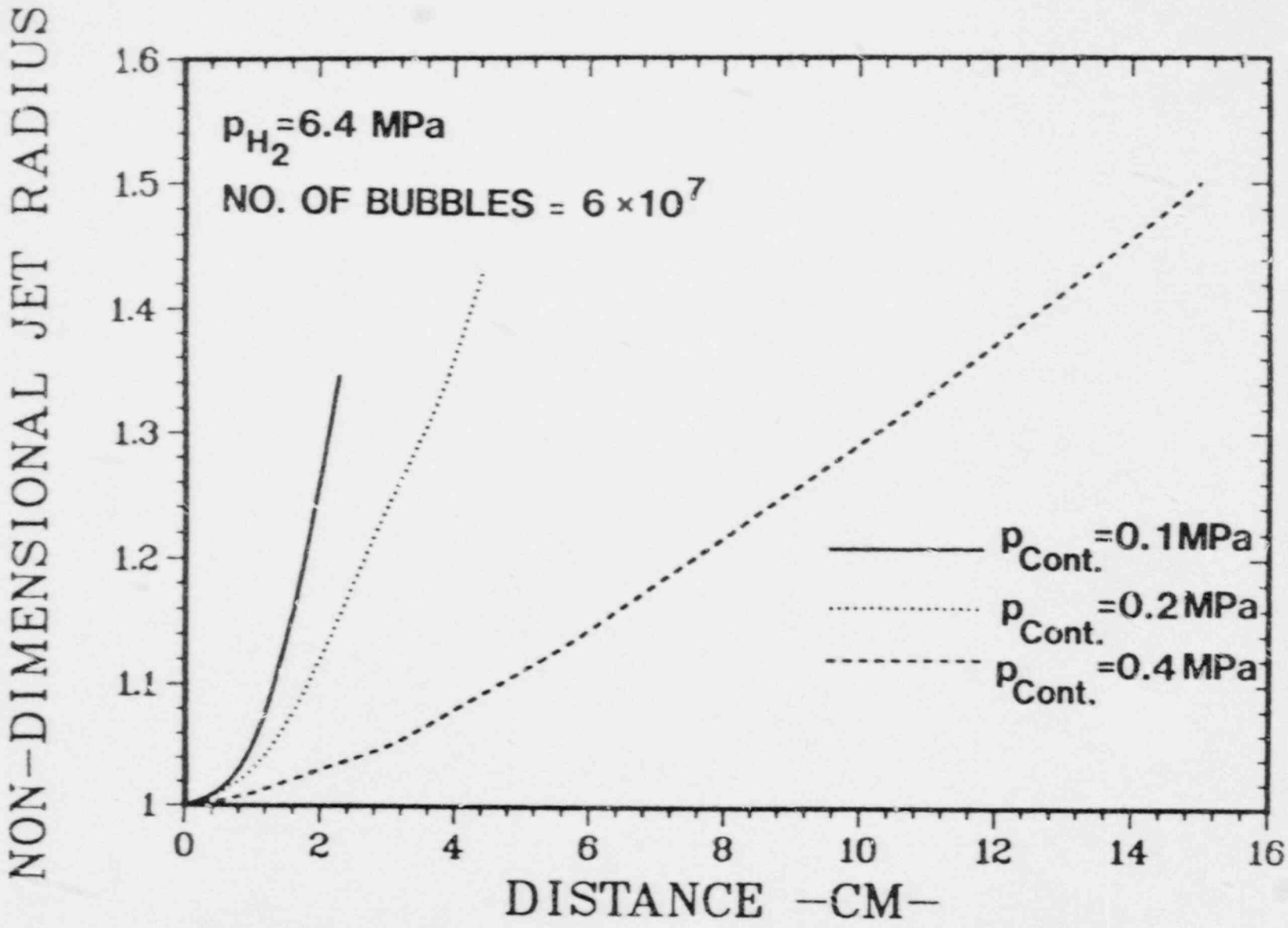

Figure 24. Reactor Case. Nondimensional jet radius as a function of the distance from the point of inception of rapid bubble growth. Containment pressure is a parameter.

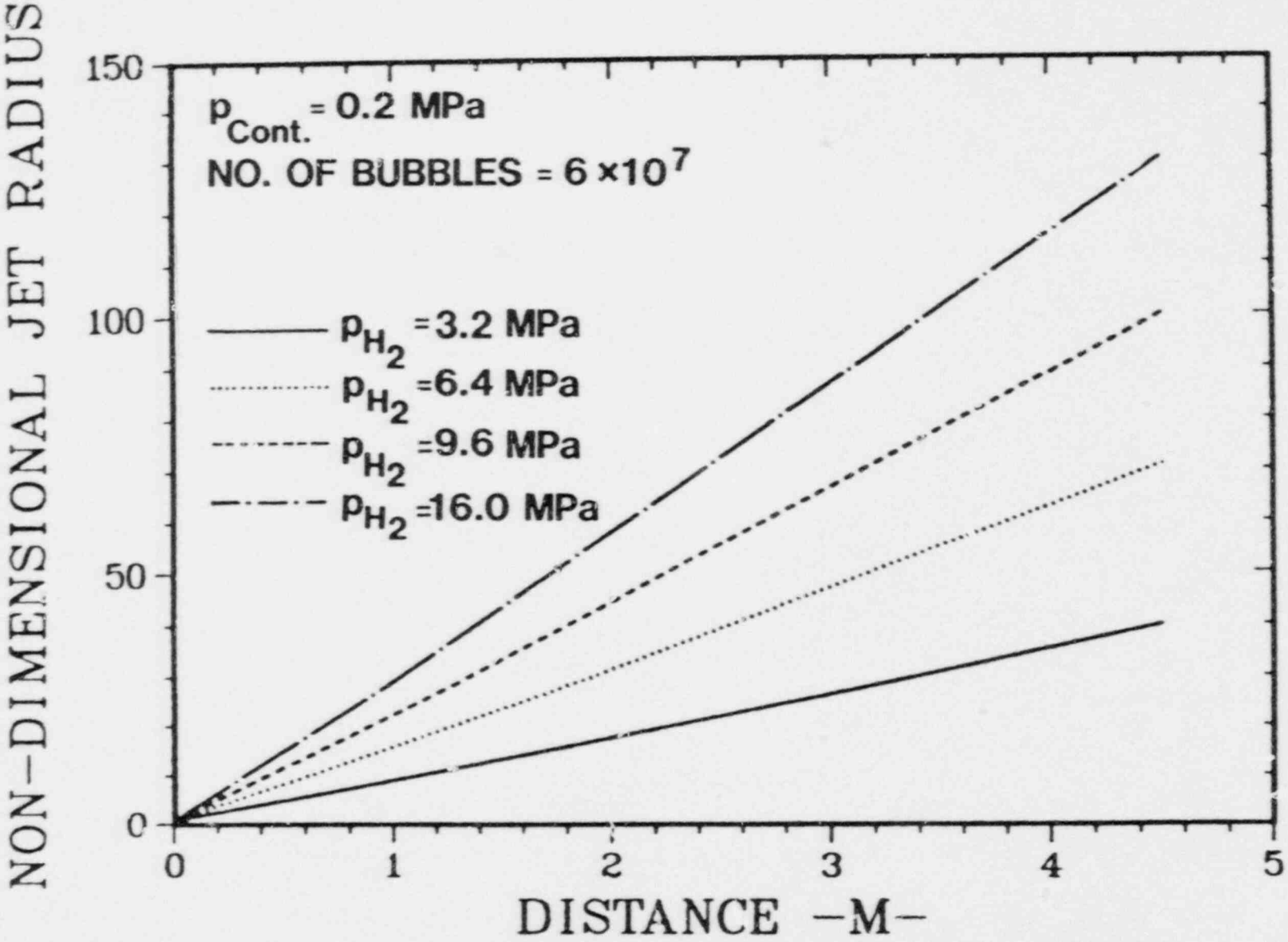

Figure 25. Reactor Case. Extrapolated nondimensional jet radius as a function of the distance from the point of inception of rapid bubble growth. Hydrogen equilibrium pressure is a parameter.

3. SECONDARY FRAGMENTATION, PARTICLE SIZE DISTRIBUTION, AND AEROSOL GENERATION

3.1 Models of Secondary Fragmentation of Melt Droplets

3.1.1 Introduction

In Section 2 of this work we showed that breakup of the molten jet resulting from effervescence of dissolved gas produces a spray of droplets. The size of the droplets is determined by the number density of gas bubbles, N, in the expanding jet and is approximately 2 to 3 mm, both in the experiments and reactor accident, for N $\sim 10^8$ m^{-3}. These droplets may undergo breakup into smaller particles - a process which we call secondary fragmentation.

The process of so-called Weber breakup, resulting from the action of the ambient gas on the droplets produced by primary jet breakup, is not likely to produce the fragment sizes observed in the experiments. An estimate of the stable droplet size can be made using concept of the critical Weber number. According to Pilch,[18] the critical Weber number is the Weber number below which breakup does not occur by acceleration of the liquid globule. For gas-liquid systems, the critical Weber number is 12 when the viscosity effect is small as in the situations considered here (see next section). The Weber number, We, is

$$We = \frac{\rho_g V^2 d}{\sigma} \quad ,$$

where ρ_g is the gas density, V is the relative velocity between droplet and gas, d is the droplet size, and σ is the liquid surface tension.

The stable droplet size is therefore

$$d = 12 \frac{\sigma}{\rho_g V^2} \quad .$$

Assuming that V is equal to jet velocity, ρ_g = 1 kg/m^3 and σ = 1 N/m and 0.5 N/m for experiments and reactor case, respectively, we obtain for the lowest and highest jet velocity.

Experiments:

$$V = 23 \text{ m/s} \quad , \quad d = 22.70 \text{ mm}$$

V = 91 m/s , d = 1.45 mm

Reactor case:

V = 15 m/s , d = 26.70 mm

V = 63 m/s , d = 1.51 mm

We will see later that the average observed fragment size is a few hundred micrometers.

In this section we will investigate three fragmentation mechanisms that are likely to be operative in the experiments and reactor accidents (pneumatic atomization, which is an important fragmentation mechanism when most of the melt has been ejected, has been studied by Pilch and Tarbell[91]). Relatively simple, and essentially mechanistic, fragmentation models will be developed and predictions for experiments and reactor conditions presented. In Section 3.1.2 we present a model describing acceleration induced fragmentation of melt droplets in a rapidly expanding gas flow field resulting from bursting gas bubbles. In Section 3.1.3 a fragmentation process due to droplet explosion is analyzed. Finally, in Section 3.1.4 we study droplet fragmentation resulting from collapse of liquid layer.

3.1.2 Acceleration Induced Fragmentation Resulting From Gas Expansion

3.1.2.1 Introduction

As stated in Section 2 of this report, the bubble pressure at the moment of primary jet breakup is above the ambient pressure. In general, this overpressure is a function of the initial gas supersaturation, gas density, gas diffusivity in the melt, melt density, and the number density of gas bubbles. However, we will restrict ourselves to consider only hydrogen gas and then the bubble overpressure in cases here analyzed is mainly a function of the initial supersaturation.

The calculations have been performed for JETA-B2 and JETA-B3 tests and for two reactor cases assuming that the primary system pressure is 16 MPa, containment pressure is 0.1 MPa and the equilibrium hydrogen partial pressure above the melt is 3.2 MPa and 16 MPa, respectively. These two reactor cases may be considered as an envelope to particle sizes produced by gas expansion during jet breakup in High Pressure Melt Ejection.

Calculated hydrogen bubble pressures, p_b, at the moment of primary breakup of the jet are:

JETA-B2:	p_b = 0.11 MPa
JETA-B3:	p_b = 0.16 MPa
Reactor Case (P_{H_2} = 3.2 MPa):	p_b = 0.14 MPa
Reactor Case (P_{H_2} = 16.0 MPa):	p_b = 0.20 MPa

In this section (3.1.2) we present a simple mechanistic model describing acceleration induced fragmentation of melt droplets in rapidly expanding gas flow field resulting from bursting of gas bubbles.

In Section 3.1.2.2 the gas field parameters and the initial Weber number are obtained from the one-dimensional shock tube model. In Section 3.1.2.3 the maximum stable fragment diameter is calculated using theory for acceleration induced droplet fragmentation.

3.1.2.2 Shock Tube Model

A schematic of the model is presented in Figure 26. An interstitial droplet is subject to a dynamic gas pressure when the gas bubbles burst. The parameters of the gas flow field are obtained from the relations for the shock tube assuming that the pressure on the left-hand side of the diaphragm is equal to the hydrogen bubble pressure and on the right-hand side of the diaphragm to the ambient pressure. We assume that the gas on the right-hand side of the diaphragm is hydrogen and that the gas temperatures are alike on both sides of the diaphragm. We think that these assumptions are reasonable considering that hydrogen will evolve from the outer surface of the jet during expansion period.

The relevant shock tube relations are:[92]

$$\frac{p_\infty}{p_b} = \frac{p_\infty}{p_2}\left[1 - \frac{\gamma-1}{2\gamma}\,\frac{\frac{p_2}{p_\infty} - 1}{\sqrt{1 + \frac{\gamma+1}{2\gamma}\left(\frac{p_2}{p_\infty} - 1\right)}}\right]^{\frac{2\gamma}{\gamma-1}}, \quad (134)$$

$$\frac{\rho_2}{\rho_\infty} = \frac{2^\gamma + (\gamma+1)\left(\frac{p_2}{p_\infty} - 1\right)}{\left(\frac{p_2}{p_\infty} - 1\right)\left(\gamma - 1\right) + 2\gamma}, \text{ and} \quad (135)$$

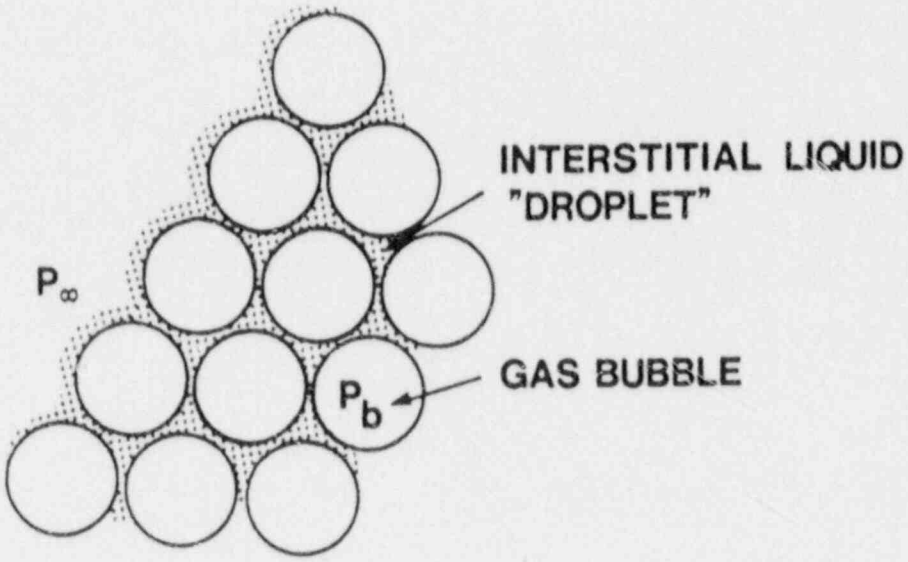

a. Interstitial Liquid Droplets

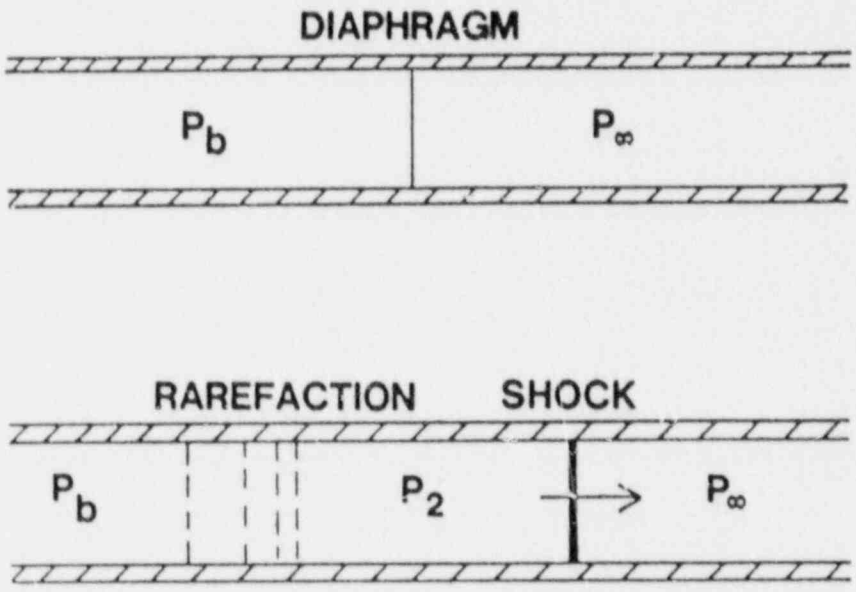

b. Shock Tube

Figure 26. Acceleration Induced Droplet Fragmentation

$$\frac{V_2}{c_\infty} = \frac{\frac{p_2}{p_\infty} - 1}{\gamma \sqrt{1 + \frac{\gamma + 1}{2\gamma} \left(\frac{p_2}{p_\infty} - 1 \right)}} \quad , \tag{136}$$

where γ is the isentropic exponent ($\gamma = 1.4$ for hydrogen), V_2 is the gas velocity and c_∞ is the sound velocity,

$$c_\infty = \sqrt{\gamma R_g T} \quad , \tag{137}$$

and ρ_∞ is obtained from perfect-gas law,

$$\rho_\infty = \frac{p_\infty}{R_g T} \quad . \tag{138}$$

First, the ratio p_2/p_∞ is calculated from Equation (134), then ρ_2 from Equation (135), and finally V_2 from Equations (136) and (137).

The initial Weber number, based on the initial diameter, D_o, of the interstitial droplet, is given by

$$We = \frac{\rho_2 V_2^2 D_o}{\sigma} \quad . \tag{139}$$

D_o is a function of the number density of gas bubbles, N, since droplet volume is approximately 1/N,

$$D_o = \left(\frac{6}{\pi N} \right)^{1/3} \quad . \tag{140}$$

3.1.2.3 Acceleration Induced Fragmentation

Having determined the initial Weber number, the maximum stable fragment size diameter may be calculated. We will use the fragmentation model proposed by Pilch,[18] who extensively studied acceleration induced fragmentation of liquid droplets. The diameter d of the largest stable fragment is given by the following expression:

$$\frac{d}{D_o} = \frac{We_c}{We} \left(1 - \frac{V_d}{V}\right)^{-2} \quad . \tag{141}$$

Here We_c is the critical Weber number, V is the free stream velocity, and V_d is the drop velocity when all breakup processes cease. The critical Weber number is the Weber number below which breakup does not occur. For gas-liquid systems,

$$We_c = 12 \left(1 + 1.077\ On^{1.6}\right) \quad , \tag{142}$$

where On is the Ohnesorge number,

$$On = \frac{\mu}{\left(\rho\sigma D_o\right)^{1/2}} \quad . \tag{5}$$

In our case the Ohnesorge number is very small ($\sim 10^{-3}$) and the critical Weber number is approximately 12.

For V_d, Pilch proposed the following expression,

$$V_d = V\epsilon^{1/2} \left(\frac{3}{4} C_d T + 3BT^3\right) \quad . \tag{143}$$

Here ϵ is the light to heavy density ratio, C_d is the drag coefficient, B is a constant, and T is the dimensionless total breakup time,

$$T = t \frac{V\epsilon^{1/2}}{D_o} \quad , \tag{144}$$

where t is the dimensional time.

For compressible flow $C_d = 1$ and $B = 0.116$.

The total breakup time is a function of Weber number. If $45 \leq We \leq 351$ then according to Pilch,

$$T = 14.1\ (We - 12)^{-1/4} \tag{145}$$

Knowing the We number, which is given by Equation (139), velocity V_d may be calculated and subsequently the maximum stable fragment size.

Pilch noted that the ratio of maximum to mass median fragment size has a constant value of 2.04 regardless of the Weber number.

Number median fragment size, d, is estimated by

$$\frac{d}{D_o} = 0.168\ We^{-1/2} \quad , \text{ for } We \geq 300. \tag{146}$$

3.1.2.4 Model Predictions and Discussion

Model predictions for JETA-B2 and JETA-B3 tests and two reactor cases are presented in Table 13. For JETA-B2 test no acceleration induced breakup is predicted since the initial Weber number is smaller than 12. The maximum stable particle sizes for the JETA-B3 test and for two reactor cases (P_{H_2} = 3.2 MPa and P_{H_2} = 16 MPa) are 561, 354, and 149 μm, respectively; the mass mean diameters are half of these values, i.e., 280, 177, and 75 μm, respectively.

Table 13

Acceleration Induced Fragmentation Resulting From Gas Expansion in JETA-B2 and JETA-B3 Tests and Reactor Accidents

Case	Initial Particle Diameter D_o (m)	Weber Number We	Maximum Stable Fragment Diameter d(m)	Total Breakup Time (s)
JETA-B2	2.7×10^{-3}	11	No breakup	
JETA-B3	2.7×10^{-3}	69	561×10^{-6}	5.3×10^{-3}
Reactor				
P_{H_2} = 3.2 MPa	3.0×10^{-3}	111	354×10^{-6}	8.6×10^{-3}
P_{H_2} = 16.0 MPa	3.0×10^{-3}	253	149×10^{-6}	4.7×10^{-3}

The total breakup time in a uniform flow field lies between 4.7 and 8.6 ms, as indicated in Table 13. A very crude estimate of the time scale during which the droplet is exposed to the flow field in experiments is the time it takes the sound wave to travel across the gas bubble or across the jet. In the former case, this time is significantly smaller than the predicted total breakup time. Therefore, the results presented here should be treated with caution. One could envisage that the droplet mass is reduced by boundary layer stripping, but that breakup is not complete. The size of the fragments produced by drop breakup as a result of the boundary layer stripping is estimated to be about 1 percent of the initial droplet diameter.[18] Hence, in our case, the fragment sizes would be in the range of 20 to 30 μm (i.e., 1 percent of 2 to 3 mm) and the mass mean diameters of the residual droplets between the mass mean diameters given above and 2 to 3 mm.

We should also mention that the droplet breakup times seem to be different in a dense droplet dispersion. There are studies, discussed in Reference 18, in which contradictory conclusions have been reached; that is, breakup times are longer or shorter when the droplet is part of a dense dispersion.

3.1.3 Fragmentation Due to Droplet Explosion

3.1.3.1 Introduction

The amount of gas evolved during jet expansion, up to the moment of jet breakup, is only on the order of a few percent of the initial gas content of the melt. Consider, for example, the reactor case with the hydrogen equilibrium pressure of 7 MPa. The corresponding hydrogen concentration in the iron component of the molten core debris is 2.36 kg-H/m^3Fe. Assume further that the containment pressure is 0.2 MPa and the number density of the gas bubbles is 10^8. The calculated bubble diameter and its internal pressure at the moment of bubble bursting (i.e., at void fraction of approximately 50 percent) are 2.6 mm and 0.23 MPa, respectively. The amount of liquid per bubble is

$$V = \frac{1}{N} \quad , \tag{147}$$

and the amount of gas per bubble in the iron phase of the corium is

$$m = 0.21 \frac{1}{N} C_o = 4.96 \times 10^{-9} \text{ kg-H}_2\text{/bubble} \quad ,$$

since the volume fraction of iron in corium is 21 percent.

The amount of gas in the bubble is

$$m = \frac{PV}{R_g T} = 2.0 \times 10^{-10} \text{ kg-}H_2\text{/bubble} \quad .$$

Thus the amount of gas evolved at primary breakup is only about four percent of the initial gas content of the melt. This means that the melt droplets generated at that moment will have practically the same degree of supersaturation as the original, coherent melt stream. Therefore, secondary fragmentation is possible, similar to the explosive disintegration of iron droplets observed during vacuum degassing and decarburization processes.[36,93,94] In both cases the explosive fragmentation is attributed to a very rapid growth of a gas bubble inside the melt droplet. An analogous mechanism has been used to explain the fragmentation of droplets of superheated water (so-called boiling fragmentation).[59,95] The mechanism of bubble nucleation in the interior of the droplet is, however, unclear. It is reasonable to assume that the bubble nucleates in the centrum of the droplet since the gas concentration should be highest there. It has been proposed,[96] as one of the explanations of melt fragmentation in vapor explosions, that homogeneous nucleation in the melt droplet could be impulse-initiated by the impulsive pressure transient. In our case the impulsive load on the drop is likely during the primary jet breakup when pressurized gas bubbles are bursting.

3.1.3.2 Rayleigh - Taylor Instability

Our model of melt droplet fragmentation is based on the observation that the interface between a growing gas bubble and the surrounding liquid shell should be subject to Rayleigh - Taylor instability since the acceleration of this interface is directed from the lighter to the heavier fluid.[97,98] A similar approach in principle, although considerably different in its treatment of the instability aspect of the problem, has been used by Kashiwa and Mjolsness in their study of the atomization of superheated water jets.[59]

The development of instability is characterized by the wave amplitude, η, and wavelength, λ, (see Figure 27). The basic idea of the model is to calculate the time at which the wave amplitude is approximately equal to the thickness of the liquid shell around the growing gas bubble, i.e., the time of fragmentation.

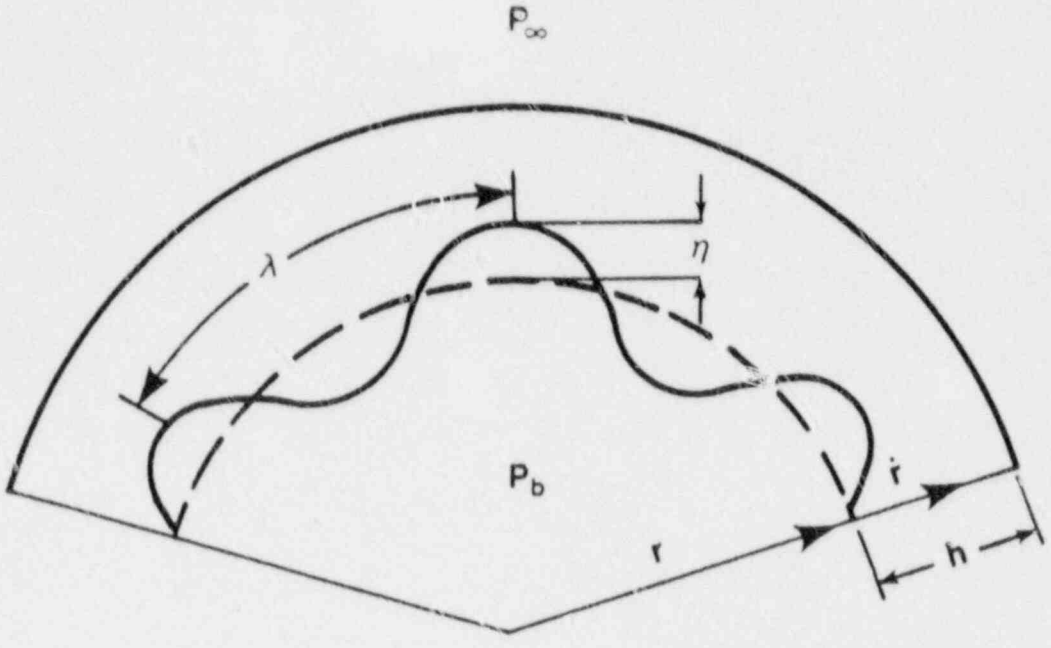

Figure 27. Schematic of Droplet Fragmentation Resulting From Rapid Expansion of Internal Gas Bubble

Given this time, the wavelength and bubble diameter at the instant of fragmentation may be calculated.

The diameter of the fragments is then given by

$$\frac{\pi d^3}{6} = \lambda^2 h \quad , \tag{148}$$

where d is the fragment size, λ is the wavelength of the wave that first penetrates the liquid shell, and h is the thickness of the liquid shell at penetration. The total number of fragments is obtained from mass balance. In order to calculate the thickness of the liquid shell, the wave amplitude and the wavelength as functions of time, the rate of bubble growth and acceleration of the liquid shell must be known. These are obtained by solving the equation of motion for the liquid shell.

We will neglect forces due to surface tension and ambient pressure and assume that bubble pressure is constant and equal to the equilibrium gas pressure. The equation of motion for the liquid shell becomes

$$m \frac{d^2 r}{dt^2} = 4\pi p_b r^2 \quad , \tag{149}$$

where m is the liquid mass, r is the bubble radius, p_b is the bubble pressure and t is time.

Putting

$$\frac{4\pi p_b}{m} = \alpha \tag{150}$$

we have

$$\frac{d^2 r}{dt^2} = \alpha r^2 \quad . \tag{151}$$

This differential equation is solved by multiplying both sides by $dr = \dot{r}\, dt$, i.e.,

$$\ddot{r}\, \dot{r}\, dt = \alpha r^2 dr \tag{152}$$

and

$$1/2\, d(\dot{r}^2) = \alpha r^2 dr \quad . \tag{153}$$

With initial conditions $r = r_0$ and $v = v_0$, the solution is

$$t = \int_{r_0}^{r} \frac{dz}{\left[v_0^2 + \Phi(z)\right]^{1/2}} \quad , \tag{154}$$

where

$$\Phi(z) = 2\alpha \int_{r_0}^{r} r^2 dr = \frac{2}{3} \alpha \left(r^3 - r_0^3\right) \quad . \tag{155}$$

Therefore,

$$t = \int_{r_o}^{r} \frac{dr}{\left[\left(v_o^2 - \frac{2}{3}\alpha r_o^3\right) + \frac{2}{3}\alpha r^3\right]^{1/2}} \quad . \tag{156}$$

This is an eliptic integral and in order to solve it analytically we assume that

$$v_o^2 - \frac{2}{3}\alpha r_o^3 = 0 \quad . \tag{157}$$

This assumption in discussed in Section 3.1.3.4. Solution of Equation (156), in terms of r(t), becomes

$$r(t) = \frac{r_o}{\left[1 - 1/2\left(\frac{2}{3}\alpha r_o\right)^{1/2} t\right]^2} \tag{158}$$

or, if we put $1/2\left(\frac{2}{3}\alpha r_o\right)^{1/2} = \gamma$,

$$r(t) = \frac{r_o}{(1 - \gamma t)^2} \tag{159}$$

Velocity and acceleration of the liquid shell are obtained by differentiating Equation (158) with respect to t, i.e.

$$\dot{r}(t) = \frac{2 r_o \gamma}{(1 - \gamma t)^3} \tag{160}$$

and

$$\ddot{r}(t) = \frac{6 r_o \gamma^2}{(1 - \gamma t)^4} \quad . \tag{161}$$

Equation (158) shows that $r(t) \to \infty$ when

$$1/2 \left(\frac{2}{3}\alpha r_o\right)^{1/2} t = 1 \quad . \tag{162}$$

Thus time when $r \to \infty$ is

$$t_c = \left(\frac{6}{\alpha r_o}\right)^{1/2} \quad . \tag{163}$$

Having determined r and $\ddot{r}$, we proceed as follows. Thickness of the liquid shell surrounding gas bubble is approximately

$$h = \frac{1}{4\pi N r^2} \quad , \tag{164}$$

since the liquid volume per bubble is 1/N, where N is the number density of gas bubbles.

As stated it is assumed that fragmentation takes place when liquid shell is penetrated by the fastest growing wave. In the linear growth phase of Rayleigh - Taylor instability, the amplitude of an initial disturbance of the form $\eta = \eta_o \cos(kx)$ is given by[97,98]

$$\eta = [\eta_o \cosh(nt) + \dot{\eta}_o/n \sinh(nt)]\cos(kx), \tag{165}$$

where η_o and $\dot{\eta}_o$ are the initial disturbance amplitude and velocity respectively, k is the wave number ($k = 2\pi/\lambda$), and n is the growth rate parameter.

The above equation is often simplified assuming $\dot{\eta}_o = 0$. Furthermore, since we are interested in the maximum wave amplitudes, the term $\cos(kx)$, which represents the spatial dependence, is omitted.

We have

$$\eta = \eta_o \cosh(nt) \tag{166}$$

Considering that $\cosh(nt) = 1/2(e^{nt} + e^{-nt})$ we can write for sufficiently large nt,

$$\eta = \eta_o e^{nt} \quad . \tag{167}$$

The growth rate parameter, n, is given by

$$n = \left[\frac{1 - \varepsilon}{1 + \varepsilon} ak - \frac{\sigma k^3}{\rho(1+\varepsilon)}\right]^{1/2} \quad , \tag{168}$$

where a is the acceleration of the interface, σ is the surface tension, and ε is given by $\varepsilon = \rho_g/\rho_\ell$.

The interface is unstable when n is a real number; thus, according to Equation (168), there is instability if

$$o < k < k_c \quad ,$$

where

$$k_c = \left[(1-\varepsilon) \frac{\rho_\ell a}{\sigma}\right]^{1/2} \tag{169}$$

The wave number k^* of the most unstable waves is

$$k^* = \frac{k_c}{\sqrt{3}} \tag{170}$$

Thus

$$k^* = \left[(1-\varepsilon) \frac{p_\ell a}{3\sigma}\right]^{1/2} \tag{171}$$

In our case $\varepsilon \to 0$ and we get

$$n = \left[ak - \frac{\sigma k^3}{\rho_\ell}\right]^{1/2} \tag{172}$$

and

$$n^* = \left[2\left(\frac{\rho_\ell}{\sigma}\right)^{1/2}\left(\frac{a}{3}\right)^{3/2}\right]^{1/2} , \qquad (173)$$

where n^* is the growth rate parameter of the most unstable, fastest growing waves.

It is reasonable to assume that the amplitude of initial disturbance η_o is given by[13]

$$\eta_o = 0.01\ \lambda_c , \qquad (174)$$

where

$$\lambda_c = \frac{2\pi}{k_c} = 2\pi\left[\frac{\sigma}{a\rho_\ell(1-\varepsilon)}\right]^{1/2} . \qquad (175)$$

Waves with wavelengths larger than λ_c are unstable.

Acceleration of the interface, a, given by Equation (161), is a function of time. Here, acceleration evaluated at $t = 0.5\ t_c$ has been used as an average.

Time when the fastest growing wave penetrates the liquid shell is obtained from the following equation by iteration:

$$\eta^* = \eta_o e^{n^* t} = \frac{1}{4\pi N r^2} , \qquad (176)$$

where $r = r(t)$ is given by Equation (157).

Knowing the time of penetration, the size of the fragments is obtained from Equation (147).

3.1.3.3 Model Predictions

Fragmentation calculations have been performed for the flashing jets of superheated water, vacuum degassing, carbon boil, JETA-B2 and JETA-B3 tests, and reactor case. The results are summarized in Tables 14, 15, and 16. In Table 14 the comparison between predicted and measured fragment size is given for flashing water jets (Brown[57] and

Gooderum and Bushnell[99], vacuum degassing (Ogunleye[36]) and carbon boil (Ellis and Glover[93] and Robertson and Jenkins[94]). The number density of gas bubbles is a parameter in all calculations, except carbon boil, since the initial droplet size depends on it.

The calculations for Table 14 were carried out with input data shown in Table 17.

Table 14 illustrates that for flashing water jets, the best-fit is obtained with a bubble density, N, of 10^9 to 10^{10}. This best-fit bubble density is in good agreement with the data obtained in some other studies of flashing phenomena.[62,100] For the vacuum degassing case, the best-fit is obtained with a bubble density close to 10^9 sites/m^3. We note also that variation in N by 1 order of magnitude changes fragment size by less than a factor of 2. Table 14 shows that the fragmentation model developed in this section gives reasonable results.

Model predictions for JETA-B2 and JETA-B3 tests are presented in Table 15. Assuming that bubble density is $10^8/m^3$ the predicted particle size for JETA-B2 is 149 μm and for JETA-B3, 109 μm. Table 16 shows that in the reactor accident, fragmentation of corium droplets is predicted to produce particles in the 50- to 150-μm-size range.

We can also see that the predicted fragment sizes are not a strong function of bubble pressure.

- Breakup efficiency

  It is interesting to estimate the efficiency of the breakup process. In our case, it is adequate to define efficiency as the ratio of the total surface energy of all fragments produced by droplet breakup to the work which could be performed in isentropic expansion of dissolved gas from the equilibrium to ambient pressure.

  The total surface energy of n particles with uniform diameter D is

$$E_S = n\pi D^2\sigma \quad , \tag{177}$$

  where n is obtained from mass balance,

$$n = \frac{6}{\pi N D^3} \quad . \tag{178}$$

Table 14

Fragmentation Due to Droplet Explosion.
Comparison of fragmentation calculations
with experimental data.

	Fragment Size (μm)				
	Predicted Number of Gas Bubbles (m^{-3})				
Reference	10^8	10^9	10^{10}	10^{11}	Measured
Flashing Water Jets					
Brown[57]		68	45	27	62
Gooderum & Bushnell[99]		170	96	56	100
Vacuum Degassing					
Ogunleye[36]	400	237	120		250
Carbon Boil					
Ellis & Glover[93]					
Robertson & Jenkins[94]		5-10			< 3

Table 15

Fragmentation Due to Droplet Explosion.
Predicted fragment size for
JETA-B2 and JETA-B3 tests.
(μm)

	Number of Gas Bubbles (m^{-3})		
Test	10^8	10^9	10^{10}
JETA-B2	149	85	49
JETA-B3	109	60	26

Table 16

Fragmentation Due to Droplet Explosion.
Predicted fragment size for reactor case.
(μm)
(Containment pressure = 0.2 MPa)

Case	Number of Gas Bubbles (m^{-3}) 10^8	10^9	10^{10}
$p(H_2)$ = 3.2 MPa	143	84	50
$p(H_2)$ = 16.0 MPa	64	50	30

Table 17

Fragmentation Due to Droplet Explosion
(Input Data to Fragmentation Calculations)

Reference	Liquid Temperature (k)	Bubble Pressure (MPa)	Ambient Pressure (MPa)	Liquid Density (kg/m^3)	Surface Tension (N/m)
Flashing Water Jets					
Brown[57]	417	0.4	0.1	1.0×10^3	0.07
Gooderum & Bushnell[99]	339	0.025	2.6×10^{-4}	1.0×10^3	0.07
Vacuum Degassing					
Ogunleye[36]	1900	0.1	2.6×10^{-4}	7.5×10^3	1.0
Carbon Boil					
Ellis & Glover[93] Robertson & Jenkins[94]	2000	10.0	0.1	5700-7500	0.5-1.0

Here N is the number density of gas bubbles.

Thus

$$E_s = \frac{6\sigma}{ND} \quad . \tag{179}$$

Isentropic expansion work per droplet is given by the following expression:

$$W = f \frac{C_o R_g T}{N(\gamma-1)} \left[1 - \left(\frac{p_\infty}{p_b} \right)^{(\gamma-1)/\gamma} \right] \quad . \tag{180}$$

Here f is the volume fraction of the melt component in which dissolved gas has concentration C_o.

Hence

$$\eta = \frac{E_s}{W} = \frac{6\sigma(\gamma-1)}{fC_o D R_g T} \left[1 - \left(\frac{p_\infty}{p_b} \right)^{(\gamma-1)/\gamma} \right]^{-1} \quad . \tag{181}$$

Breakup efficiency was calculated for JETA-B experiments and two reactor cases with hydrogen equilibrium pressure of 3.2 MPa and 16 MPa, respectively. We have determined that 0.4 percent $< \eta <$ 1 percent.

3.1.3.4 Discussion

The fragmentation mechanism described in this section cannot be operative in SPIT experiments where nitrogen has been used as driving gas. This is because the nitrogen dissolved in the melt droplet is not able to support the bubble pressure during fragmentation process. The situation is different in the case of hydrogen due to its low density.

We return now to the assumption stated in Equation (157) which imposes the following relation between the initial velocity and bubble radius:

$$r_o = \left(\frac{3}{2} \frac{v_o^2}{a} \right)^{1/3} \quad . \tag{182}$$

This relation is justified in the following way. The bubble growth prior to explosive escalation is mainly inertia controlled. It was shown in Section 2 that the Jakob number and parameter B_I for bubble growth are high, thus indicating inertia dominated growth.

Another way of determining which growth regime dominates is to calculate the time for transition between inertia- and diffusion-controlled growth. The transition occurs when growth rates for both regimes are approximately equal. Using Equations (73) and (86), we find that transition time is

$$t = \frac{6\beta^2 D\rho}{\Delta p} \tag{183}$$

and the transition radius is

$$R = 6\beta^2 D\left(\frac{2}{3}\frac{\rho}{\Delta p}\right)^{1/2} . \tag{184}$$

For JETA-B2 and JETA-B3 tests and reactor conditions, this radius is of an order of 1 mm. For the same conditions, the bubble radius at which acceleration of the liquid shell commences, i.e., r_o in Equation (158) (determined from the force balance) is approximately 0.1 mm. Therefore, the initial velocity may be obtained from inertia-controlled growth. Now the initial bubble radius, given by Equation (183), is also approximately 0.1 mm.

Therefore, the difference between r_o obtained from the force balance and from Equation (183) is small. This means, however, that our calculations of droplet explosion start from an initial bubble radius, which is not exactly the right one, but since we are interested here in an elementary investigation of a possible fragmentation mechanism the refined calculation is not necessary.

The same argument, i.e., our interest in an elementary investigation of a possible fragmentation mechanism, applies to the assumption that the bubble pressure is constant and equal to the equilibrium gas pressure thus neglecting diffusional limitations to mass transport. However, we have seen that bubble growth is dominated by liquid inertia, and furthermore, that predicted fragment size is not a strong function of bubble pressure.

Applying Rayleigh - Taylor instability theory the following assumptions have been made: (1) linear growth phase, (2) infinite fluid depth, (3) cosh(nt) may be approximated

by 0.5 e^{nt}, and (4) the theory for a plane interface is valid. To verify these assumptions we need to know acceleration of the interface, a, wavelength of the fastest growing wave, λ_c, the growth rate parameter, n, product nt, and the thickness of the liquid shell at the instant of fragmentation, h.

The values of these parameters for the most unstable wave differ little between analyzed cases - except carbon boil - and are on average: $a = 10^5$ g, $\lambda_c = 5 \times 10^{-5}$ m, $n^* = 10^5$ s^{-1}, $n^*t = 4$, and $h = 10^{-4}$m.

We see immediately that cosh(nt) can be approximated by 0.5 e^{nt}.

- Changeover from the linear phase to the nonlinear phase

  According to Pilch[18] it is reasonable to assume that changeover from the linear phase to the nonlinear phase occurs when the computed linear phase growth rate equals the computed nonlinear phase growth rate. This means that the lower of the two growth rates should be used.

  The growth rate in the linear phase is given by (spacial dependence is neglected):

$$\dot{\eta}_\ell = \eta_o \, n \sinh(nt) + \eta_o \cosh(nt) \tag{185}$$

  and for nonlinear growth phase we have[101]

$$\dot{\eta}_n = 0.24 \, ((1-\varepsilon)a\lambda)^{1/2} \tag{186}$$

  Taking $\eta_o = 0.01 \, \lambda_c$ and using above parameter values we obtain $\eta_\ell < \eta_n$, but difference is small.

- The effect of finite fluid depth

  The effect of finite fluid depth on the instability growth was investigated by Taylor.[97] Assuming that the thickness of a liquid sheet is h, he obtained the following expression describing behavior of the instability in case of the small amplitude waves:

$$\eta_\ell = \eta_o \left[\frac{\cosh(nt) - e^{-2kh}\cos(nt)}{1 - e^{-2kh}} \right] \cos(kx) \tag{187}$$

Thus the correction to the case when $h \to \infty$ is e^{-2kh}. The wave amplitude exceeds that predicted by the classic theory only by eight percent when $h = 0.2\lambda$. Therefore, it was justified to neglect the influence of finite fluid depth.

- Instability in spherical geometry

Acceleration induced instability of spherical interface was studied by Birkhoff,[102] Plesset and Mitchell,[103] and Plesset and Prosperetti.[104] It was shown that under certain circumstances the interface is stable when on the basis of the Rayleigh - Taylor theory for a plane interface it would be unstable. Also the opposite is possible but in this case the instability growth is algebraic and not exponential as in the plane case.

The stability of a small-amplitude distortion of a spherical interface is determined by the following equation:

$$\ddot{a}_n + 3\frac{\dot{R}}{R}\dot{a}_n - Aa_n = 0 \qquad (188)$$

Here a_n is the distortion amplitude of order n and if $\varepsilon \to 0$ then

$$A = (n-1)\left[\frac{\ddot{R}}{R} - \frac{(n+1)\,(n+2)\,\sigma}{\rho_\ell R^3}\right] \qquad (189)$$

The interface is unstable if $A > 0$ or, if $A < 0$, when $6A\dot{R} + \dot{A}R > 0$.

In all cases analyzed in this section $A > 0$ so that expanding spherical gas bubbles are unstable.

3.1.4 Fragmentation Resulting From Droplet Inflation Followed by Collapse of the Liquid Layer

3.1.4.1 Introduction

In studies on the disruptive burning of free droplets,[105] it has been observed (using a high-speed movie camera) that disintegration of the liquid droplet is the result of the following process. A short time after ignition the droplet diameter increases by about a factor of three until the outer liquid layer of the inflated droplet bursts with subsequent release of the interior gas and the outer layer collapse toward the center of the droplet resulting in the

fragmentation of the liquid into many small droplets. The size of the fragments is not reported and no fragmentation model was proposed.

It has been concluded that droplet inflation is the result of the homogeneous bubble nucleation within the interior of the droplet and the spontaneous formation, growth and bursting of a single vapor bubble.

The analogous mechanism of the secondary fragmentation to that described above is also possible in the case of gas supersaturated liquid droplet. A simple fragmentation model is proposed in Section 3.1.4.2.

3.1.4.2 Model

In the model describing fragmentation because of droplet explosion (Section 3.1.3), it was assumed that bubble growth in the interior of the melt droplet is intertia controlled and the bubble pressure was taken to be equal to the initial equilibrium gas pressure. Here, we will assume that bubble growth is diffusion controlled which means that the bubble pressure is close to the ambient pressure.

A schematic of the model is shown in Figure 28. The work of expanding gas is transformed into surface energy of the liquid layer surrounding the gas bubble. In order to calculate the fragment size it is assumed that during the fragmentation process the surface energy is conserved. This means that the efficiency of energy transformation is 100 percent and in consequence the calculated average fragment size is the smallest attainable by this fragmentation process.

The surface energy of the liquid layer is approximately

$$E_S = 2A\sigma = 2\pi D^2\sigma \quad . \tag{190}$$

Here D is the outer diameter of the inflated droplet and σ is the liquid surface tension.

Assuming that the diameter of the inflated droplet is x times the initial, undisturbed droplet diameter, D_o, we get

$$E_S = 2\pi(xD_o)^2\sigma \quad . \tag{191}$$

The surface energy of all fragments is

$$\Sigma E_S = n\pi d^2\sigma \quad , \tag{192}$$

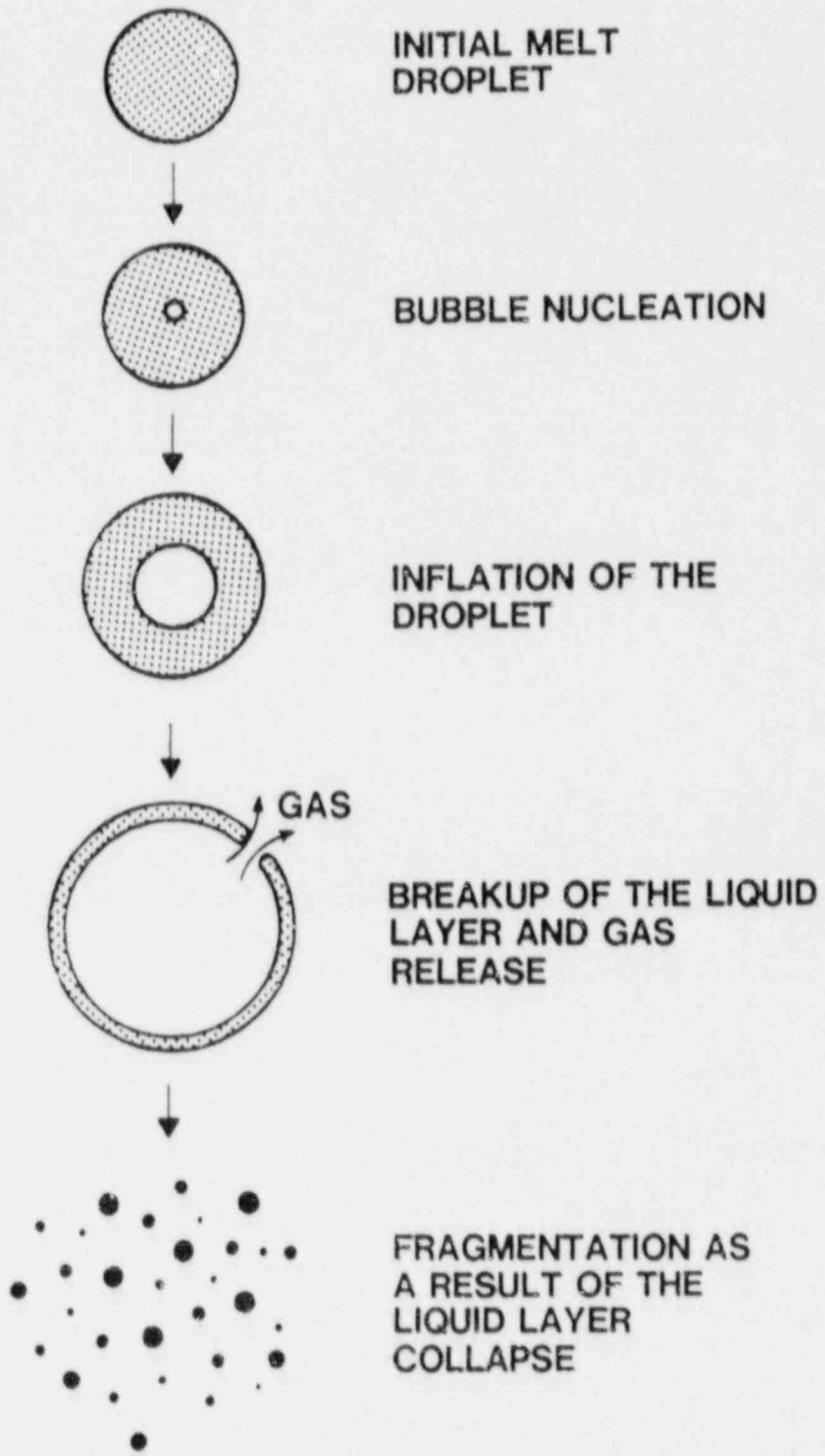

Figure 28. Fragmentation Resulting From Droplet Inflation Followed by Collapse of the Liquid Layer

where n is the total number of fragments and d is the fragment diameter.

From mass balance we obtain

$$n = \left(\frac{D_o}{d}\right)^3 \quad . \tag{193}$$

From condition $E_s = \sum E_s$ it follows, therefore, that

$$d = D_o \frac{1}{2x^2} \tag{194}$$

or, noting that

$$D_o = \left(\frac{6}{\pi N}\right)^{1/3} \quad , \tag{195}$$

where N is the number density of gas bubbles in expanding jet,

$$d = \left(\frac{6}{\pi N}\right)^{1/3} \frac{1}{2x^2} \quad . \tag{196}$$

3.1.4.3 Model Predictions

Model predictions for $N = 10^8$, 10^9, and 10^{10}, and $x = 2$, 3, and 4 are illustrated in Table 18. We assume that the actual value of the parameter x lies between 2 and 4.

3.2 Debris Characterization

3.2.1 Introduction

In this section, the size distribution of the debris collected from the JETA-B2 and JETA-B3 tests is described and characterized. The results obtained here are used in the next section to estimate the fraction of the melt aerosolized in the tests.

The large fragments (a few hundred micrometers to two or three millimeters) recovered from the JETA-B tests consists of roughly spherical particles. Some of these large

Table 18

Fragmentation Resulting From Droplet Inflation Followed by Collapse of the Liquid Layer

	Predicted Fragment Size (μm)		
	Number of Gas Bubbles (m^{-3})		
X	10^8	10^9	10^{10}
2	334	155	72
3	149	69	32
4	84	39	18

particles are punctured and partially void. The composition of the collected particles was not analyzed, as was done in the SPIT tests. However, since the melt composition and the postulated fragmentation mechanisms are the same it is reasonable to assume that the composition of particles is identical in the SPIT and JETA-B tests.

For the SPIT tests Brockmann and Tarbell[106] have reported that the composition of the collected particles appears to be size dependent. The small mode particles (< 1- to 3- μm) are predominantly iron. This suggests that they are formed by iron vapor condensation. The large size fraction particles (> 1- to 3- μm) are predominantly iron, predominantly aluminum oxide, or a combination of the two. This indicates that large particles are formed by mechanical breakup of an inhomogeneous melt of aluminum oxide and iron.

3.2.2 Particle Size Distribution

Size distribution of the debris collected from the JETA-B2 and JETA-B3 tests was obtained by sieve analysis. The particle size distribution plotted on log-normal paper is shown in Figure 29. The data were fitted by the log-normal distribution. It has been found that the log-normal distribution correlates most of the size data for particles obtained by fragmentation.[107]

Kottler[108] presented theoretical basis why log-normal distribution applies to fragmentation processes. If it is assumed that the relative rate of change of particle size in

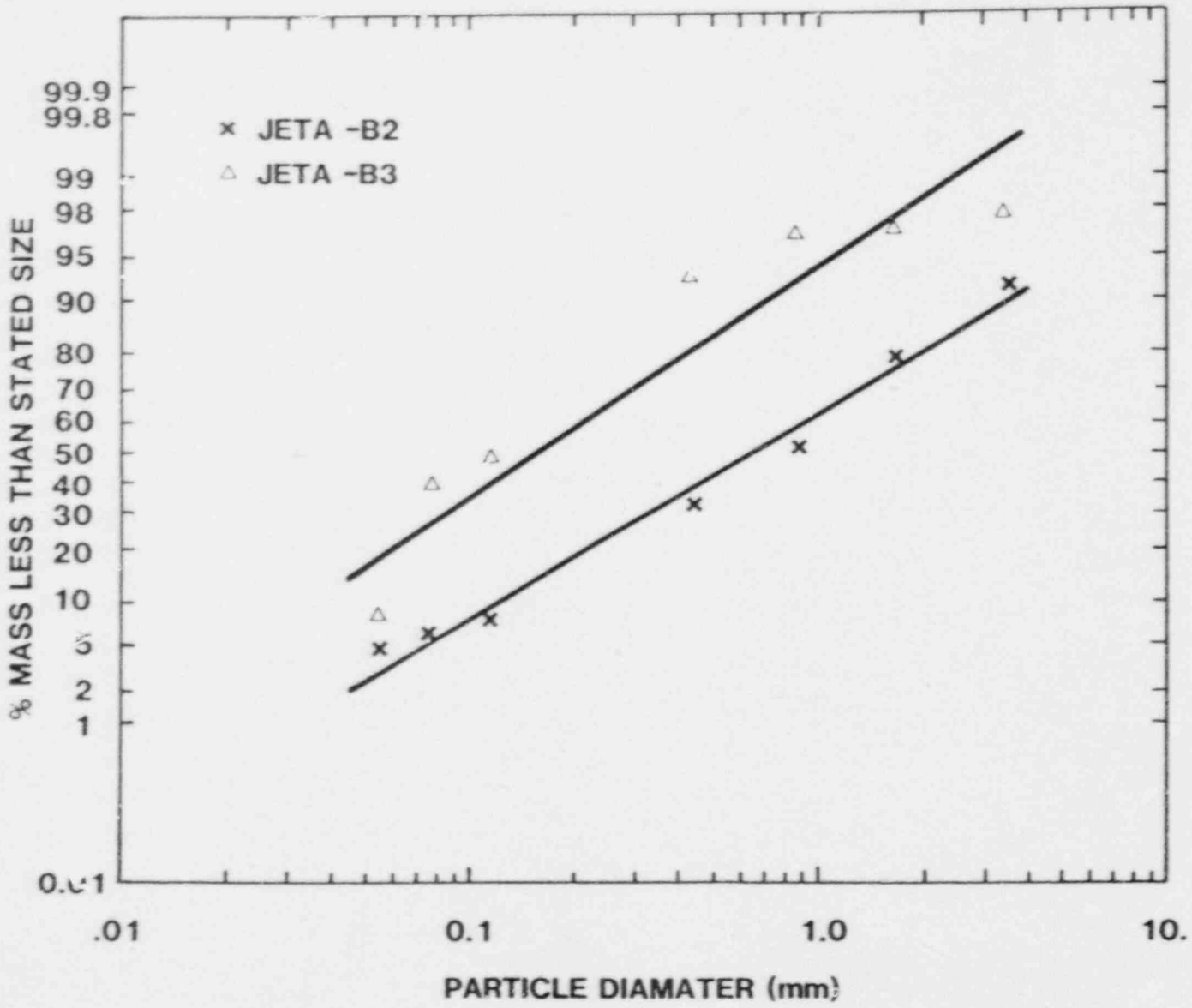

Figure 29. Particle Size Distribution for JETA-B2 and JETA-B3 Tests

fragmentation is independent of the absolute quantity of material present, then

$$\frac{dD}{dt} = -kD \quad , \tag{197}$$

where D is the particle diameter, t is time, and k is a rate constant.

Integrating Equation (197) we get

$$D = D_o e^{-kt} \quad , \tag{198}$$

where D_o is a constant of integration.

Equation (198) may be written in the following form

$$t = a+b \cdot \ln(D) \quad , \tag{199}$$

where a and b are constants.

Equation (199) expresses time as a function of size, D. The time available for fragmentation of each particle will be different and random. It was shown that it is justified to assume that the distribution of times is normal. The distribution of D which follows from the assumed normal distribution of times is called log-normal.

For a random positive variable, in this case the particle size, that is log-normally distributed, the log-normal distribution function is

$$f(D) = \frac{1}{\sqrt{2\pi}\, D\sigma} \exp\left(-\frac{(\ln D-\mu)^2}{2\sigma^2}\right) \tag{200}$$

where μ and σ are distribution parameters.

3.2.3 Particle Size Distribution Parameters

The geometric mean diameter, denoted D_{50}, is given by

$$D_{50} = e^{\mu} \quad . \tag{201}$$

The geometric standard deviation, σ_g, is characterized by e^{σ}

$$\sigma_g = e^{\sigma} = \frac{D_{84}}{D_{50}} = \frac{D_{50}}{D_{16}} \quad , \tag{202}$$

where D_{16}, and D_{50} and D_{84} are the 16, 50 and 84 percent points of the distribution. Since the log-normal distribution plots as a straight line on log-normal paper, the parameters μ and σ can be determined directly from a plot.

In practical applications of the particle size data it is desirable to use the average diameters that have some physical meaning. The various average diameters have been defined by Mugele and Evans[109] by the following expression

$$\bar{D}_{qp}^{q-p} = \int_{-\infty}^{\infty} D^q f(D)dD \Big/ \int_{-\infty}^{\infty} D^p f(D)dD \quad . \tag{203}$$

Some of the mean diameters most often used are number mean (D_{10}), surface mean (D_{20}), volume mean (D_{30}), and volume-surface, or Sauter mean, (D_{32})

Sauter mean is given by

$$\bar{D}_{32} = \frac{\bar{D}_{30}^{3}}{\bar{D}_{20}^{2}} \quad . \tag{204}$$

A very convenient property of log-normal distribution is that it can be written on surface, volume or surface-volume basis. This leads to the following useful relations between means:[11]

$$\ln\bar{D}_{20} = \ln\bar{D}_{10} + 2\ln^2\sigma_g \tag{205}$$

$$\ln\bar{D}_{30} = \ln\bar{D}_{10} + 3\ln^2\sigma_g \tag{206}$$

$$\ln\bar{D}_{32} = \ln\bar{D}_{10} + 2.5\ln^2\sigma_g \tag{207}$$

Particle size distribution parameters for the JETA-B2 and JETA-B3 tests, obtained from Figure 29 and from Equations (205), (206), and (207), are presented in Table 19.

Table 19

Particle Size Distribution Parameters
for JETA-B2 and JETA-B3 Tests

Test	Mass Mean Diameter (μm)	Geometric Standard Deviation σ_g	$\bar{D}_{10}$ (μm)	$\bar{D}_{20}$ (μm)	$\bar{D}_{32}$ (μm)
JETA-B2	700	3.57	5.43	138	310
JETA-B3	160	3.44	1.64	115	75

3.2.4 Discussion and Conclusions

Experimental particle size distribution for JETA-B2 and JETA-B3 tests rather broad distribution (σ_g~3.5). For comparison, e distribution of particles produced by pneumatic atomizers is characterized by σ_g~1.3.

As expected, the mass mean diameter for JETA-B3 is smaller than for JETA-B2 due to higher hydrogen concentration in the melt. Comparison within Section 3.1 calculated fragment sizes suggests that acceleration induced fragmentation resulting from gas expansion could be a dominating fragmentation mechanism, at least in cases when equilibrium hydrogen pressure is high. The maximum stable fragment size calculated for JETA-B3 is 561 μm, see Table 13. According to Pilch,[15] the mass mean fragment size is one half of maximum fragment size, regardless of the Weber number. Thus, for JETA-B3 we have D_{mass} = 280 μm to compare with 160 μm obtained experimentally.

Regarding JETA-B2 test, the calculated Weber number is close to 12 indicating that some acceleration induced fragmentation (from the initial fragment size of approximately 2 to 3 mm) could be possible producing fragment sizes of the order of 1 mm.

In summary, even if we were not able to analytically predict particle size distribution, the fragment sizes determined from the models of primary breakup and secondary fragmentation fall into the particle size range determined experimentally, i.e., ≈ 100 μm to 2 to 3 mm.

3.3 Aerosol Generation

3.3.1 Introduction

As mentioned in Section 1 of this report, a significant amount of aerosol was generated during pressurized melt ejection in the SPIT and JETA-B jet characterization experiments. The aerosol measurements were performed in the SPIT tests. Brockmann and Tarbell[106] estimated the mass fraction of melt aerosolized to be 0.6 to six percent. The following three mechanisms that could produce melt particles smaller than approximately 60 μm have been proposed:

1. Condensation of iron vapor; particles < 1 μm.

2. Film fragmentation as a result of bubble bursting; particles 1 to 10 μm.

3. Pneumatic atomization; particles 10 to 60 μm.

Pneumatic atomization occurs when liquid and gas are simultaneously accelerated through an orifice. This mechanism of melt fragmentation has been reviewed by Pilch and Tarbell.[91] For the reactor accident conditions, they predicted that the mass median size of particles produced by pneumatic atomization could range from 20 to 300 μm.

In the next two sections, we will address mechanisms 1 and 2 above. Due to large uncertainties and complexity of the phenomena involved only simple estimates will be made.

3.3.2 Vaporization of Iron

The vapor pressure of iron is high at the temperature of thermite and corium melts. It is significantly higher than the vapor pressure of aluminum oxide which explains why in SPIT tests the particles in the small size fraction are predominantly iron.[106]

The aerosol is formed when iron vapor condenses. An upper bound estimate of the iron aerosol mass produced in high pressure melt ejection is obtained in the following way. The total mass of condensed iron vapor, m, is

$$m = GAt, \qquad (208)$$

where G is the mass flux of iron atoms across a plane surface, A is the total surface of iron and t is time available for vaporization.

An estimate of G can be derived from the kinetic theory of gases. Assuming a Maxwell-Boltzman velocity distribution

the average positive x-component of velocity for a monoatomic ideal gas is[111]

$$u = \left(\frac{kT}{2\pi m}\right)^{1/2} , \tag{209}$$

where k is the Boltzman constant, T is the temperature, and m is the mass of the atom.

A more convenient expression for u is obtained from Equation (209) using standard thermodynamic relations,

$$u = \left(\frac{R_g T}{2\pi}\right)^{1/2} , \tag{210}$$

where R_g is the gas constant.

The mass flux G is

$$G = \rho u , \tag{211}$$

where ρ is the gas density.

For ideal gas we have

$$\rho = \frac{P}{R_g T} . \tag{212}$$

Substituting Equations (210) and (212) into Equation (211) we get

$$G = \frac{p}{\sqrt{2\pi R_g T}} \tag{213}$$

Here p is the equilibrium vapor pressure corresponding to temperature T.

Equation (213) gives an upper bound for the evaporation or condensation rate. In reality, the rate of mass flux is given by

$$G' = \alpha G \quad . \tag{214}$$

Here α is the condensation or evaporation coefficient (also called the accomodation coefficient). In condensation α is the fraction of the molecules striking the surface that condenses. The evaporation coefficient is defined similarly.

Under equilibrium conditions the condensation and evaporation fluxes are equal. The net evaporation flux under non-equilibrium conditions is obtained by substracting evaporation mass flux from condensation mass flux. Assuming that evaporation and condensation coefficients are equal and neglecting a correction term resulting from the mean molecular velocity toward the interface, we obtain

$$G'_{net} = \frac{\alpha}{\sqrt{2\pi R_g T}} \left[p_s - p_g \left(\frac{T}{T_g} \right)^{1/2} \right] \quad . \tag{215}$$

Here subscripts s and g refer to the equilibrium conditions at temperature T and to gas conditions at the interface.

In evaporation $T \sim T_g$ and we get

$$G'_{net} = \frac{\alpha}{\sqrt{2\pi R_g T}} \left(P_s - P_g \right) \quad . \tag{216}$$

This expression is sometimes called the Hertz-Knudsen equation.[41]

The total area of the iron interface is given by the total area of melt droplets multiplied by the ratio, f, of the area occupied by iron to the total area:

$$A_{Fe} = f\pi \sum_i D_i^2 \quad , \tag{217}$$

where D is the droplet diameter.

The area per unit melt volume is

$$\frac{A_{Fe}}{V} = f \frac{\pi \sum_i D_i^2}{(\pi/6) \sum_i D_i^3} = f \frac{6}{\bar{D}_{32}} \quad , \tag{218}$$

since

$$\frac{\sum_i D_i^3}{\sum_i D_i^2} = \bar{D}_{32} = \text{Sauter diameter} \quad .$$

Thus

$$A_{Fe} = 6fV \frac{1}{\bar{D}_{32}} \tag{219}$$

or

$$A_{Fe} = 6fM \frac{1}{\rho \bar{D}_{32}} \quad , \tag{220}$$

where M is the total melt mass and ρ is its density.

Finally, the time, t, for vaporization is estimated by the time it takes for the jet to travel from the orifice to the ground:

$$t = \frac{h}{V_j} \quad , \tag{221}$$

where h is the distance and v_j is the jet velocity.

Substituting Equations (216), (220), and (221) into (208) we have

$$m = 6\alpha f h M \frac{p_s - p_g}{\rho \bar{v}_j D_{32} \sqrt{2\pi R_g T}} \tag{222}$$

Calculations have been performed for the conditions of the JETA-B2 and JETA-B3 tests. According to von Bogdandy,[26] the accomodation coefficient for liquid metals is usually between 0.1 and 1; we have used $\alpha = 0.5$. The vapor pressure, p_g, was neglected since it is not known. The

temperature of the melt is an important variable since vapor pressure of iron is a strong function of it. Unfortunately, we don't know exactly the temperature of the melt droplets. We have assumed that T = 2200 and 2500 K. These temperatures allow for some incompleteness of the thermite reaction and cooling of the droplets. The vapor pressures of iron corresponding to these temperatures are 5×10^2 Pa and 5×10^3 Pa, respectively.

Finally, the ratio, f, was assumed to be equal to the volume fraction of iron in the melt. With these assumptions the following results have been obtained:

- T = 2200 K

  JETA-B2: m = 0.27 kg
  JETA-B3: m = 0.28 kg

  The fraction of melt aerosolized is 2.6 and 2.7 percent for JETA-B2 and JETA-B3, respectively.

- T = 2500 K

  JETA-B2: m = 2.7 kg
  JETA-B3: m = 2.8 kg

  The fraction of melt aerosolized is 26 and 27 percent for the JETA-B2 and JETA-B3, respectively.

  Equation (222) shows that at a given temperature the fraction of iron aerosolized is a function of the product $v_j D_{32}$. It turns out that in cases here considered the value of this product differs little and is independent of pressure. This is reasonable considering that $v_j \simeq p^{1/2}$ (from Bernoulli's equation) and that $\bar{D}_{32}$ should be inversely proportional to the initial hydrogen concentration in the melt, $\bar{D}_{32} \sim 1/C_o$, or, applying Sievert's law of solubility, $\bar{D}_{32} \sim p^{-1/2}$.

  We want to emphasize that above results are estimates. The actual fraction of iron aerosolized may be smaller because the iron vapor pressure in gas phase, p_g, should reach a saturation value quickly, if the vapor is not effectively removed. However, it is interesting to note that results for T = 2200 K fall into the range of estimated fraction of melt aerosolized in SPIT tests (0.6 to 6 percent).

3.3.3 Aerosol Generation Resulting From Bubble Bursting

One possible mechanism of aerosol generation during pressurized melt ejection is breakup of melt film when gas

bubbles burst. The literature on this mechanism has been reviewed by Ginsberg[112] and Powers et al.[113]

Experimental water data show that film breakup is the dominant aerosol generation mechanism for bubbles larger than ~ 1 mm in diameter. Considering that gas bubbles in experiments and reactor case are ~ 3 to 4 mm in diameter when they burst, the aerosol generation by film breakup may be operative in experiments and reactor case. However, it is not clear if direct extrapolation of water data to thermite melt and corium is allowed.

A number of estimates of the volume of droplets produced per bubble burst has been presented. It appears that most data may be approximated by

$$10^{-7} < \frac{V_a}{V_b} < 10^{-5} \quad .$$

Here V_a is the volume of aerosol produced per bubble burst and V_b is the volume of bubble at instant of burst.

Taking the average of the above range we get

$$V_a = 5 \times 10^{-6} V_b \quad . \tag{223}$$

The total mass of aerosol produced in experiments may be calculated from Equation (223) since bubble volume at instant of burst and number of gas bubbles are known.

Thus for D = 3 mm, N = $10^8/m^3$, and 10.3 kg melt (V = 2.7×10^{-3} m^3) we obtain

$$V_a = 1.9 \times 10^{-8} \ m^3$$

and

$$m = V_a \rho = 7.3 \times 10^{-5} \ kg \quad .$$

Hence the fraction of melt aerosolized by postulated film breakup mechanism is 7×10^{-4} percent.

3.3.4 Conclusions

The results obtained in Sections 3.3.2 and 3.3.3 lead to the following conclusions:

1. Vaporization of iron may produce significant amount of aerosol during pressurized melt ejection.

2. Aerosol generation resulting from film breakup is probably negligible during pressurized melt ejection.

3.4 Overall Jet Breakup Efficiency and Size of Corium Fragments

3.4.1 Introduction

In this section we propose a simple method that makes it possible to directly estimate the size of particles produced by jet fragmentation due to effervescence of dissolved gas. The method is based on the observation that the overall jet breakup efficiencies, defined in next section, differ relatively little for three investigated hydrogen super-saturated jets even if the initial conditions are quite different. More confidence was attached to the proposed method when we found that for some investigated cases of the flashing superheated water the overall breakup efficiencies lie in a rather narrow range.

In Section 3.4.2 we show how breakup efficiency is obtained from the initial conditions for melt ejection and particle size distribution. The breakup efficiency for a few cases of the flashing water is briefly investigated in Section 3.4.3. Predictions for reactor accident situations are presented in Section 3.4.4.

3.4.2 Overall Jet Breakup Efficiency

It is appropriate to define the overall jet breakup efficiency as a ratio of the total surface energy produced by jet breakup to the work available for fragmentation. Under assumption that jet disruption is caused by energetic effervescense of dissolved gases, this work is calculated as the mechanical work which could be performed by dissolved gas in an isentropic expansion process.

Hence

$$\eta = \frac{E_s}{W} \quad . \tag{224}$$

Here η is the breakup efficiency, E_s is the total surface energy of the droplets, and W is isentropic work.

The total surface energy, E_s, and the isentropic work, W, are given by

$$E_s = \pi\sigma\sum_i D_i^2 \tag{225}$$

and

$$W = \frac{mR_gT}{\gamma-1}\left[1-\left(\frac{p_\infty}{p_o}\right)^{(\gamma-1)/\gamma}\right] \tag{226}$$

Here D is the droplet diameter; σ is the surface tension; m is the mass of the dissolved gas at equilibrium pressure, P_o, and temperature, T; and p_∞ is the ambient pressure.

The mass of the dissolved gas is given by

$$m = C_o V_{Fe} \quad , \tag{227}$$

where C_o is the equilibrium gas concentration corresponding to the gas partial pressure p_o, and V_{Fe} is the volume of iron in the melt. As stated earlier, C_o is obtained from the Sievert's law of solubility.

It is convenient to express E_s and W per unit volume of the melt. In a similar way as in Section 3.3.2, we obtain

$$\frac{E_s}{V} = \frac{6\sigma}{\bar{D}_{32}} \quad , \tag{228}$$

where $\bar{D}_{32}$ is the Sauter mean diameter.

Dividing Equation (226) by V and using Equation (227) we get

$$\frac{W}{V} = \frac{fC_oR_gT}{\gamma-1}\left[1-\left(\frac{p_\infty}{p_o}\right)^{(\gamma-1)/\gamma}\right] \quad , \tag{229}$$

where f is the volume fraction of iron in the melt ($f = V_{Fe}/V$).

Hence

$$\eta = \frac{\bar{E}_s}{W} = \frac{6\sigma(\gamma-1)}{fC_o R_g T \bar{D}_{32}\left[1 - p_\infty/p_o^{(\gamma-1)/\gamma}\right]} \qquad (230)$$

Thus, knowing initial conditions for melt ejection and particle size distribution, the breakup efficiency may be determined from Equation (230). Also, knowing η, $\bar{D}_{32}$ may be calculated from Equation (230).

The experimental data base available to us, which is required to calculate breakup efficiency, is rather limited and comes from three experiments, namely Robertson and Ogunleye,[30] JETA-B2, and JETA-B3. The initial conditions and $\bar{D}_{32}$ for the JETA-B2 and JETA-B3 experiments were given earlier.

For the experiment by Robertson and Ogunleye we have

$C_o = 0.19$ kgH/m^{3}Fe

$p_o = 0.1$ MPa

$p_\infty = 266$ Pa

$T = 1873$ K

$\sigma = 1.0$ N/m.

Robertson and Ogunleye have reported that up to 80 percent of the discharged material was collected as a powder with 50 percent passing 250 μm. Assuming log-normal distribution with $\sigma_g = 3.5$ we get

$\bar{D}_{32} = 114$ μm .

We have obtained the following results for the considered experiments:

Robertson and Ogunleye	$\eta = 1.4$ percent
JETA-B2	$\eta = 0.5$ percent
JETA-B3	$\eta = 0.6$ percent

This is an interesting result considering, as mentioned previously, that initial conditions for these three experiments were considerably different.

3.4.3 Breakup Efficiency for Flashing Water

Experimental data base for breakup of liquid jets due to effervescence of dissolved gases is quite limited. This applies especially to the particle size distribution. The situation is somewhat better regarding breakup of the flashing superheated water. In this case, breakup of the liquid is caused by nucleation and subsequent rapid growth and bursting of vapor bubbles. The driving force for vapor nucleation and bubble growth is superheating of the liquid. A considerable amount of work was done in this area because of the importance of the subject in the analysis of loss-of-coolant accidents in light water reactors.[62,100,114-120] Disintegration of liquid jets due to the flashing mechanism has also been studied.[57-59,95,99,121-130]

Since the mechanism of liquid breakup caused by either effervescence of dissolved gas or liquid superheat is principally the same, we have decided to investigate the overall breakup efficiency in the latter case.

The overall breakup efficiency was defined in the similar way as in the previous section. The work available for liquid breakup was taken, following Lienhard,[131] as work that the system could do upon its surroundings in returning to equilibrium

$$W = (h_o - h_f) - T_{sat} (s_o - s_f) \qquad (231)$$

Here h is the specific entalphy, s is the specific entropy, T_{sat} is the saturation temperature at ambient pressure and subscripts o and f denote the locally superheated conditions and saturated liquid, respectively.

The mean drop size for sprays formed by flashing water jets emanating from small nozzle ($D < 1$ mm) was measured by Brown[57] and Gooderum and Bushnell.[99] Anderson, Erdman and Reynolds[120] measured drop size distribution from bulk flashing.

Brown studied breakup of superheated jets emanating from three nozzle types: sharp-edged, rough and extremely rough. We have not analyzed all experiments reported by Brown but found that in four experiments--two in sharp-edged nozzle and two in rough nozzle, where the temperature of the water was the same but the jet Weber number and nozzle diameter were slightly different--the breakup efficiency was

about 0.05 percent. Efficiency for the extremely rough nozzle was significantly higher since, as reported by Brown, much smaller droplets were produced by mechanical breakup of liquid inside the nozzle where surface roughness was very high ($\varepsilon/D = 0.1$).

Calculations for experiments reported by Gooderum and Bushnell could not be exact since the ambient pressure varied between 2 and 98 Torr. However, we have found that breakup efficiencies lie between 0.01 and 0.08 percent.

Breakup efficiency in experiment reported by Anderson, Erdman and Reynolds is about 0.02 percent.

These results seem to suggest that breakup efficiencies lie in a rather narrow range.

3.4.4 Predictions for Reactor Case

Sauter mean diameter was calculated from Equation (230) assuming that the overall jet breakup efficiency is 0.6 percent. The result is presented in Figure 30 where Sauter mean diameter, $\bar{D}_{32}$, is plotted as a function of hydrogen equilibrium pressure in the iron component of the corium melt. Calculations were performed for containment pressures of 0.1 and 0.2 MPa. We see that the $\bar{D}_{32}$ is in the range of 75 to 630 μm for hydrogen equilibrium pressure in the range of 0.1 to 16.0 MPa. This particular size range is in reasonable agreement with results obtained from the models of secondary fragmentation presented in Section 3.1

3.4.5 Conclusions

The method of calculating particle sizes proposed here is based on a very limited experimental data base. It seems, however, that it may be used in cases where the properties of the liquid metal are similar and the effervescing gas is the same.

Inspection of Equation (230) and the fact that breakup efficiencies differ little suggest a relationship between $\bar{D}_{32}$ and initial gas supersaturation, C_o/C_s, since according to Sievert's law of solubility C_o/C_s is proportional to $(p_o/\rho_\infty)^{1/2}$. However, in order to investigate this more experimental data are needed.

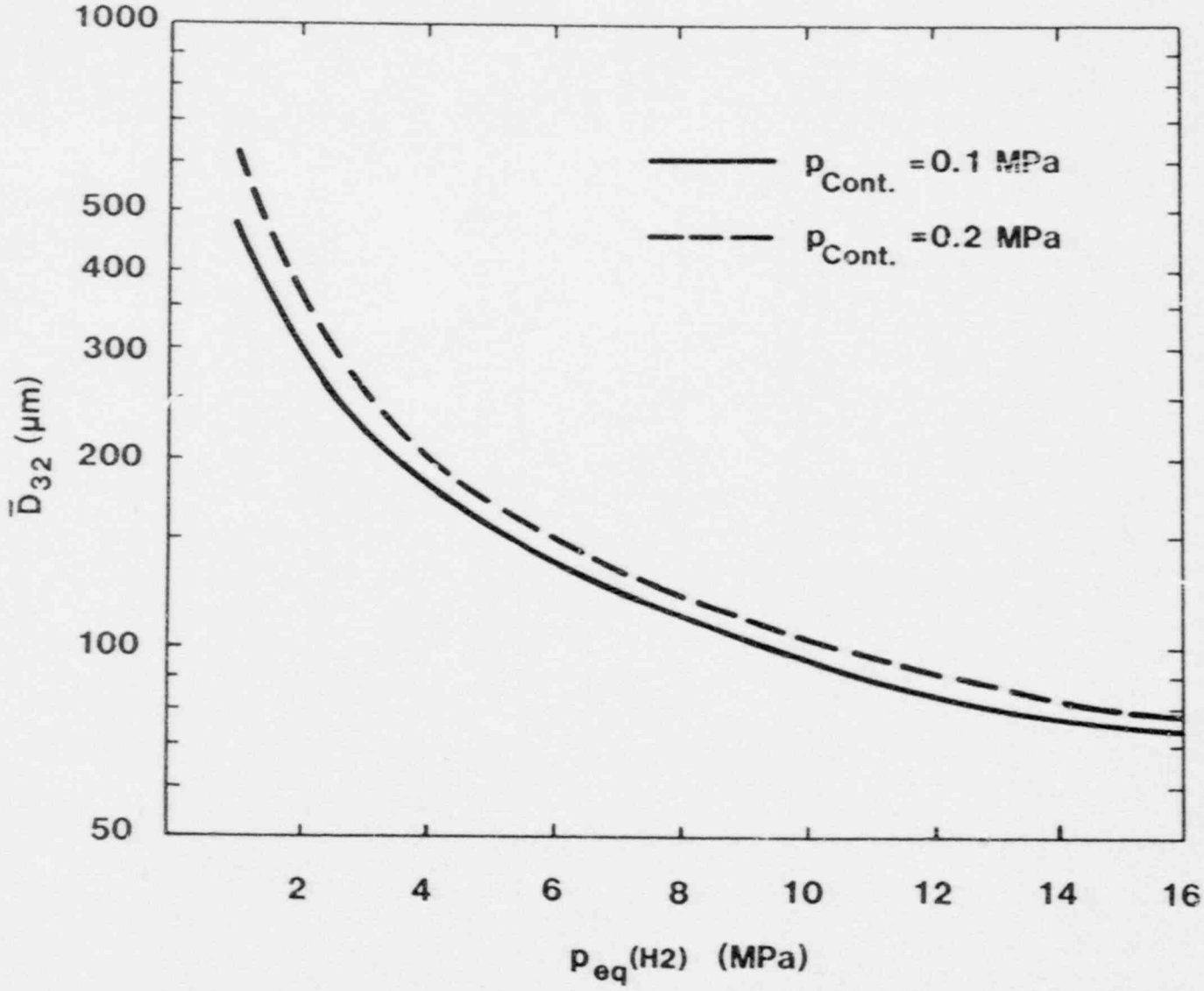

Figure 30. Sauter Mean Droplet Diameter, $\bar{D}32$, as a Function of Hydrogen Equilibrium Pressure in the Iron Component of Corium

4. SUMMARY AND CONCLUSIONS

Discharge of the molten core debris from a pressurized reactor vessel has been recognized as an important accident scenario for pressurized water reactors. Recent high-pressure melt streaming experiments conducted at Sandia National Laboratories, designed to study cavity and containment events related to melt ejection, have resulted in two important observations:

1. Expansion and breakup of the ejected molten jet.

2. Significant aerosol generation during the ejection process.

The expansion and breakup of the jet in the experiments are attributed to rapid evolution of the pressurizing gas (nitrogen in SPIT tests and hydrogen in JETA-B tests) dissolved in the melt. It has been concluded that aerosol particles may be formed by condensation of melt vapor and mechanical breakup of the melt and that the extent of melt disruption influences the aerosol generation.

It was shown that above phenomena are also likely to occur in reactor accidents. The disruption of a corium jet could affect (1) aerosol generation and through this the source term, (2) concrete erosion in the cavity region, (3) molten fuel-coolant interaction, if water is present in the cavity, (4) removal of core debris from the cavity region, and (5) direct containment heating.

As a result of the information and insights gained from the experiments and from theoretical considerations, an analytical and experimental effort was undertaken, aimed at the development of a model describing the behavior of a gas-supersaturated liquid jet expelled from a pressurized vessel. The results of this effort are described in this report.

The investigation of jet behavior during pressurized melt ejection was divided into two parts. First, a one-dimensional model of jet expansion and primary breakup was developed and employed in analysis of experimental data and reactor accidents. This work is described in Section 2 of this report where we also address aero-hydrodynamic stability of liquid jet in gas, stream degassing of molten metals, and gas bubble nucleation in molten metals.

We have shown that the aero-hydrodynamic jet stability theory cannot explain jet behavior observed in experiments.

Review of nucleation theory has led us to the conclusion that possibility of spontaneous nucleation under conditions prevailing in experiments and reactor accidents cannot be disregarded.

The jet expansion model is based on an appropriate bubble growth model. We have found that inertial effects are important for fast growing hydrogen bubble in highly supersaturated liquid metal. Therefore, a general bubble growth model was developed that includes both inertia-controlled and diffusion-controlled growth phases.

The jet expansion model is able to predict the jet void fraction and jet radius as a function of axial distance from nozzle exit, bubble size and bubble pressure. Breakup of the jet is assumed to occur when jet void fraction is about 50 percent. Jet breakup produces spray of melt droplets; these droplets may undergo secondary fragmentation.

A crucial parameter in the model is the number density of gas bubbles in the molten jet. We were not able to calculate this parameter, but we determined it experimentally. An interesting result was obtained: namely, the number density of gas bubbles is approximately the same in all experiments and equal to about $10^8/m^3$ of liquid. The primary jet breakup produces a spray of relatively coarse droplets, about 2 to 3 mm in diameter, both in experiments and reactor accidents.

Parametric calculations have shown that for a TMLB' reactor accident sequence (the Zion reactor) the corium jet is disrupted within a few initial jet diameters from the reactor vessel. The calculations also show that the radius of corium spray at the level of the reactor cavity floor is in the range of 0.8 to 2.6 m for a the hydrogen concentration in the iron component of corium corresponding to a hydrogen equilibrium pressure in the range of 3.2 to 16 MPa. The containment pressure has a strong effect on the jet expansion through its role in the bubble growth.

In Section 3 of this report we (1) developed models of secondary fragmentation of melt droplets, (2) characterized the debris collected in JETA-B tests (3) presented calculations of aerosol generation due to condensation of iron vapor and film breakup, and (4) investigated the overall jet breakup efficiency and from it estimated the size of corium fragments produced in reactor accident situations.

Three possible mechanisms of secondary fragmentation have been investigated, namely acceleration induced fragmentation resulting from gas expansion when gas bubbles burst, fragmentation due to droplet explosion and fragmentation resulting from collapse of gas-inflated melt droplet. Predicted

fragment sizes are in reasonable agreement with experimental data. We have concluded that acceleration induced breakup of melt droplets may be a dominating mechanism of secondary fragmentation.

Particles generated by secondary fragmentation of corium melt are predicted to be in 70-to 350-μm-size range.

Considering aerosol generation we have concluded that vaporization of iron may produce significant amount of aerosol during pressurized melt ejection and that aerosol production resulting from film breakup is probably negligible.

We have found that the overall jet breakup efficiencies differ relatively little for the three molten jets investigated even if the initial conditions are considerably different. Average particle size may be calculated if breakup efficiency is known. In this way the average size of particles produced by breakup of corium jet was estimated. For the hydrogen equilibrium pressure in the iron component of the corium in the range 1.0 to 16.0 MPa, the Sauter mean diameter ($\bar{D}_{32}$) and mass mean diameter are in the 75- to 630-μm and 220- to 1400-μm-size range, respectively. In accordance with experimental results it was assumed that the particle size distribution is lognormal with geometric standard deviation of about 3.5.

5. REFERENCES

1. M. F. Young e al., "MELPROG Code Development and Methods," Proceedings, International Meeting on LWR Severe Accident Evaluation, Vol. 1, p 2.8-1, 1983, Cambridge, MA.

2. N. Rasmussen et al., Reactor Safety Study: An Assessment of Accident Risks in U.S. Commercial Nuclear Power Plants, WASH-1400, NUREG-75/014, Washington, DC, 1975.

3. Commonwealth Edison Co., Zion Probabilistic Safety Study, Chicago, IL, 1981.

4. J. J. Sienicki and B. W. Spencer, "Analysis of Hydrodynamic Phenomena in Simulant Experiments Investigating Cavity Interactions Following Postulated Vessel Meltthrough," Proceedings of the 22nd National Heat Transfer Conference, August 6-8, 1984, Niagara Falls, NY.

5. W. Tarbell, J. Brockmann, and M. Pilch, High-Pressure Melt Streaming (HIPS) Program Plan, Sandia National Laboratories, Albuquerque, NM, NUREG/CR-3025, SAND82-2477, August 1984.

6. D. A. Powers, Solubility of Gases in Molten Materials Produced During Reactor Core Meltdowns, Sandia National Laboratories, Albuquerque, NM, SAND83-1976 (in printing).

7. "Steam Explosions in Light Water Reactors," Report of the Swedish Government Committee on Steam Explosions, (Stockholm: DsI, 1981), p 3.

8. L. S. Nelson and P. M. Duda, Steam Explosion Experiments With Single Drops of Iron Oxide Melted With a CO_2 Laser, Sandia National Laboratories, Albuquerque, NM, NUREG/CR-2295, SAND81-1346, September 1981.

9. G. Long, "Explosions of Molten Aluminum in Water-Cause and Prevention," Metal Progress 71, pp 107-112 (1957).

10. M. Berman, D. V. Swenson, and A. J. Wickett, An Uncertainty Study of PWR Steam Explosions, Sandia National Laboratories, Albuquerque, NM, NUREG/CR-3369, SAND83-1438, May 1984.

11. P. H. Schweitzer, "Mechanisms of Desintegration of Liquid Jets," J of Applied Physics 8, p 513 (August 1937).

12. R. D. Reitz, "Atomization and other Breakup Regimes in a Liquid Jet," Ph. D. Dissertation, Princeton University, Dept. Mechanical and Aerospace Eng. (October 1978).

13. M. Pilch, 1984, Sandia National Laboratories, Albuquerque, New Mexico. Private Communication.

14. T. Ginsberg, "Liquid Jet Breakup Characterization with Application to Melt-Water Mixing," Proceedings of the International ANS/ENS Topical Meeting on Thermal Reactor Safety, San Diego, CA, February 2-6, 1986, Vol. 5, pp II 4-1 - II 4-18, American Nuclear Society, LaGrange Park, 1986.

15. Lord Rayleigh, "On the Instability of Jets," Proceedings of the London Mathematical Society 10, pp 4-13, 1878.

16. R. P. Grant and S. Middleman, "Newtonian Jet Stability," A I Ch E Journal 12(4), pp 669-678 (July 1966).

17. V. Levich, "Physicochemical Hydrodynamics," (New Jersey: Prentice-Hall, Inc. Englewood Cliffs, 1962).

18. M. Pilch, "Acceleration Induced Fragmentation of Liquid Drops," Ph. D. Dissertation, University of Virginia (1981).

19. T. A. Engh and K. Larsen, "Breakup Length of Turbulent Water or Steel Jets in Air," Scand. J. Metallurgy 8, pp 161-167, (1979).

20. J. D. Sharp, "Physical Considerations in the Stream Degassing of Steel," Vacuum Degassing of Steel, The Iron and Steel Institute, Special Report 92, pp 50-54, 1965.

21. R. G. Olsson and E. T. Turkdogan, "Stream Degassing of Steel: Enhanced Performance with Argon Injection," Journal of the Iron and Steel Institute, pp 1-8 (January 1973).

22. J. A. Belk, Vacuum Techniques in Metallurgy, (Pergamon Press, 1963).

23. J. H. Flux, "Vacuum Degassing 1955-1965: A Survey of Processes and Plant for Bulk Steel Production," Vacuum Degassing of Steel, The Iron and Steel Institute, Special Report 92, pp 1-24, 1965.

24. A. V. Bradshaw, "Kinetic Aspects of Vacuum Refining," Le Vide 138, pp 376-416 (November-December 1968).

25. A. V. Bradshaw and F. D. Richardson, "Thermodynamic and Kinetic Aspects of Vacuum Degassing," Vacuum Degassing of Steel, The Iron and Steel Institute, Special Report 92, pp 24-46, 1965.

26. L. von Bogdany, "Gas-Metal Kinetics in Steelmaking," Steelmaking: The Chipman Conference, J. F. Elliot and J. R. Meadowcroft, eds., pp 156-168, The M.I.T. Press, 1965.

27. O. Winkler, "Degassing Kinetics of Molten Metals in Vacuum," J. Vacuum Sci. Technol. 7(6), pp 514-521 (1970).

28. F. D. Richardson, "Interfacial Phenomena and Metallurgical Proccesses," Canadian Metallurgical Quarterly 21(2), pp 111-119 (1982).

29. D. E. Rosner and M. Epstein, "Effects of Interface Kinetics, Capilarity andd Solute Diffusion on Bubble Growth Rates in Highly Supersaturated Liquids," Chem. Eng. Sci. 27, pp 69-88 (1972).

30. D. G. C. Robertson and A. Ogunleye, A Laboratory Study of Stream Degassing of Molten Iron, Imperial College Report, London.

31. J. Szekely and N. Themelis, Rate Phenomena in Process Metallurgy, (New York: Wiley-Interscience, 1971).

32. N. A. Warner, "Stream Break-Up in Vacuum Degassing," J. Iron andd Steel Institute, pp 44-50 (January 1969).

33. S. Mizoguchi, D. G. C. Robertson, and A. V. Bradshaw, "Stream Degassing," Physical Chemistry of Process Metallurgy: The Richardson Conference, J. H. E. Jeffes and R. J. Tait, eds., Institute of Mining and Metallurgy, London, 1974.

34. S. Mizoguhi, D. G. C. Robertson, and A. V. Bradshaw, "Nozzle Pressure During Stream Degassing," Iron and Steel Institute of Japan 18, pp 177-180 (1978).

35. S. Mizoguhi, D. G. C. Robertson, and A. V. Bradshaw, "Bubble Growth During Stream Degassing," Second Australasian Conf. on Heat and Mass Transfer, pp 392-399, University of Sydney, February 1977.

36. A. Ogunleye, "Removal of Dissolved Hydrogen in Liquid Iron," Second International Congress on Hydrogen in Metals, Paris, France, June 6-11, 1977.

37. S. G. Bankoff, "Nucleation," in Two-Phase Fluid Flow and Heat Transfer, Sandia National Laboratories, Albuquerque, NM, 1983.

38. R. C. Reid, "Rapid Phase Transition from Liquid to Vapor," in Advances in Chemical Engineering, Vol. 12, (New York: Academic Press, 1983) pp 106-203.

39. V. P. Skripov, Metastable Liquids (New York: John Wiley and Sons, 1974).

40. F. D. Richardson, Physical Chemistry of Melts in Metallurgy, Vol. 2 (London: Academic Press, 1974).

41. J. P. Hirth and G. M. Pound, Condensation and Evaporation; Nucleation and Growth Kinetics (New York: The Macmillan Company, 1963).

42. L. Bernath, "Theory of Bubble Formation in Liquids," Ind. and Eng. Chem. 44(6), pp 1310-1313 (1957).

43. J. P. Hirth, G. M. Pound, and G. R. St. Pierre, "Bubble Nucleation," Metallurgical Trans. 1, pp 939-945 (April 1970).

44. L. A. Swanger and W. C. Rhines, "On the Necessary Conditions for Homogeneous Nucleation of Gas Bubbles in Liquids," J. of Crystal Growth 12, pp 323-326 (1972).

45. M. Blander and J. L. Katz, "Bubble Nucleation in Liquids," AIChE Journal 21(5), pp 833-848 (September 1975).

46. J. W. Gibbs, The Scientific Papers of J. Willard Gibbs, Vol. 1 (New York: Dover Publications, 1961), pp 252-258.

47. J. Lothe and G. M. Pound, "Statistical Mechanics of Nucleation," in Nucleation, A. C. Zettlemoyer, ed. (New York: Marcel Dekker, Inc., 1969).

48. H. S. Levine, "On the Initiation Mechanism for Explosion During Combustion of Metal Droplets," High Temp. Sci. 3(3), pp 237-243 (May 1971).

49. H. S. Levine, "Formation of Vapor Nuclei in High Temperature Melts," J. Physical Chemistry 76(18), pp 2609-2614 (1972).

50. H. S. Levine, "Homogeneous Nucleation of CO Bubbles in Fe-C-O Melts," Metallurgical Trans. 4, pp 777-782 (March 1973).

51. R. T. Mayer and L. S. Nelson, "The Role of Nitrogen in the Formation of Microbubbles During the Explosive Combustion of Zirconium Droplets in N_2/O_2 Mixtures," High Temp. Sci. 2, pp 35-57 (1970).

52. J. H. Swisher and E. T. Turkdogan, "Decarburization of Iron-Carbon Melts in CO_2-CO Atmospheres; Kinetics of Gas-Metal Surface Reactions," Trans. Metallurgical Society AIME 239, pp 602-610 (May 1967).

53. B. C. Allen, "The Surface Tension of Liquid Metals," in Liquid Metals, Chemistry and Physics, S. Z. Beer, ed. (New York: Marcel Dekker, Inc, 1972).

54. R. W. Ostensen, W. F. Murphy, B. J. Wrona, L. W. Dietrich, and J. C. Florek, "Intrusion of Molten Steel into Cracks in Solid Fuel in a Transient-Uncercooling Accident in a Liquid-Metal Fast Breeder Reactor," Nucl. Technol. 36, pp 200-214 (December 1977).

55. P. Nikolopoulos and G. A. Ondracek, "Interfacial Energies Between Uraniumdioxide and Liquid Metals," J. Nucl. Mater. 98, pp 306-312 (1981).

56. R. S. Kaplan and W. O. Philbrook, "The Rate of CO Bubble Nucleation at Oxide Metal Interfaces Within Liquid Iron Alloys," Metallurgical Trans. 3, pp 483-487 (February 1972).

57. R. Brown, "Sprays Formed by Flashing Liquid Jets," Ph.D. Dissertataion, University of Michigan (1961).

58. V. A. Fedoseev, "Dispersion of a Stream of Superheated Liquid," Colloid Journal USSR 20(4), pp 463-466 (1958).

59. B. A. Kashiwa and R. C. Mjolsness, Analytical Studies Pertaining to Steam Generator Tube Rupture Accidents, Los Alamos National Laboratory, Los Alamos, NM, LA-10307-MS, NUREG/CR-4079, 1985.

60. K. Hijikata, Y. Mori and T. Nagatani, "Experimental Study on Bubble Nucleation in the Oscillating Pressure Field," J Heat Transfer, 100, pp 460-465 (August 1978).

61. D C. Leslie, The Development of Flashing Flow From Existing Nucleation Sites, United Kingdom Atomic Energy Authority Reactor Group, AEEW-R505, Winfrith, Dorchester, 1966.

62. P. Saha, N. Abuaf, and B. J. C. Wu, "A Nonequilibrium Vapor Generation Model for Flashing Flows," Trans. ASME 106, pp 198-203 (February 1984).

63. S. G. Bankoff, "Diffusion-Controlled Bubble Growth," in Advances in Chemical Engineering, Vol. 6, (New York: Academic Press, 1966), pp 1-59.

64. S. G. Bankoff, "Bubble Dynamics," Two-Phase Fluid Flow and Heat Transfer, Sandia National Laboratories, Albuquerque, NM.

65. Lord Rayleigh, "On the Pressure Developed in a Liquid During the Collapse of a Spherical Cavity," Phil. Mag 34, pp 94-98 (1917).

66. M. S. Plesset and S. A. Zwick, "A Nonsteady Heat Diffusion Problem with Spherical Symmetry," J. Appl. Phys. 23(1), pp 95-98 (January 1952).

67. M. S. Plesset and S. A. Zwick, "The Growth of Vapor Bubbles in Superheated Liquids," J. Appl. Phys. 25(4), pp 493-500 (April 1954).

68. H. K. Forster and N. Zuber, "Growth of a Vapor Bubble in a Superheated Liquid," J. Appl. Phys. 25(4), pp 474-478 (April 1954).

69. G. Birkhoff, R. S. Margulies, and W. A. Horning, "Spherical Bubble Growth," Phys. Fluids 1(3), pp 201-204 (May-June 1958).

70. L. E. Scriven, "On the Dynamics of Phase Growth," Chem. Eng. Sci. 10, pp 1-13 (1959).

71. S. G. Bankoff, "Asymptotic Growth of a Bubble in a Liquid with Uniform Initial Superheat," Appl. Sci. Res. A(12), pp 267-281 (1964).

72. B. B. Mikic, W. M. Rohsenow, and P. Griffith, "On Bubble Growth Rates," Int. J. Heat Mass Transfer 13, pp 657-666 (1970).

73. T. G. Theofanous and P. D. Patel, "Universal Relations for Bubble Growth," Int. J. Heat Mass Transfer 19, pp 425-429 (1976).

74. A. Prosperetti and M. S. Plesset, "Vapor-Bubble Growth in a Superheated Liquid," J. Fluid Mech. 85(part 2), pp 349-368 (1978).

75. J. Szekely and G. P. Martins, "Non Equilibrium Effects in the Growth of Spherical Gas Bubbles Due to Solute Diffusion," Chem. Eng. Sci. 26, pp 147-159 (1971).

76. J. Szekely and G. P. Martins, "On Spherical Phase Growth in Multicomponent Systems," Trans. Metallurgical Society AIME 245, pp 1741-1747 (August 1969).

77. G. P. Martins, "The Interaction of Gas Bubbles with Liquids at Sub-Atmospheric Pressures," Ph.D. Dissertation, University of New York at Buffalo (February 1970).

78. J. Szekely, G. P. Martins, and S. D. Fang, "Bubble Growth by Diffusion. The Effect of Viscosity, Inertia and Surface Tension," VDI-Berichte Nr. 182, pp 13-22 (1972).

79. J. Szekely and S. D. Fang, "Non-Equilibrium Effects in the Growth of Spherical Gas Bubbles Due to Solute Diffusion - II. The Combined Effects of Viscosity, Liquid Inertia, Surface Tension and Surface Kinetics," Chem. Eng. Sci. 28, pp 2127-2140 (1973).

80. E. J. Barlow and W. E. Langlois, "Diffusion of Gas from a Liquid into an Expanding Bubble," IBM Journal, pp 329-337 (July 1962).

81. W. E. Langlois, "Similarity Rules for Isothermal Bubble Growth," J. Fluid Mech. 15, pp 111-118 (1963).

82. R. B. Bird, W. E. Stewart, and E. N. Lightfoot, Transport Phenomena, (New York: John Wiley and Sons, 1960).

83. H. Portitsky, "The Collapse or Growth of a Spherical Bubble or Cavity in a Viscous Fluid," Proc. 1st U.S. Natl. Congr. Appl. Mech. 1, pp 813-821, 1951.

84. L. E. Scriven, "On the Dynamics of Phase Growth," Chem. Eng. Sci. 17, p 55 (1962).

85. P. Dergarabedian, "The Rate of Growth of Vapor Bubbles in Superheated Water," J. Appl. Mech. 20, pp 537-545 (1953).

86. J. W. Murdock, "An Investigation of High Velocity Flashing Flow in a Straight Tube," Ph.D. Dissertation, Massachusetts Institute of Technology (January 1965).

87. H. Reiss and V. K. La Mer, "Diffusional Boundary Value Problems Involving Moving Boundaries, Connected With the Growth of Colloidal Particles," J. Chem. Phys. 18(1), pp 1-12 (January 1950).

88. Geoges L. Chahine and Han Lieh Liu, "A Singular-Perturbation Theory of the Growth of a Bubble Cluster in a Superheated Liquid," J Fluid Mech, 156, pp 257-279 (1985).

89. J. D. Fast, Interactions of Metals and Gases, Vol. 1, Thermodynamics and Phase Relations, (New York: Academic Press, 1965).

90. F. E. Haskin et al., Analysis of a Hypothetical Core Meltdown Accident Initiated by Loss of Offsite Power for the Zion 1 Pressurized Water Reactor, Sandia National Laboratories, Albuquerque, NM, NUREG/CR-1988, SAND81-0503, November 1981.

91. M. Pilch and W. Tarbell, High Pressure Ejection of Melt From a Reactor Pressure Vessel: The Discharge Phase, Sandia National Laboratories, Albuquerque, NM, NUREG/CR-4383, SAND85-0012, September 1985.

92. Ascher H. Shapiro, The Dynamics and Thermodynamics of Compressible Fluid Flow - Vol. II, (New York: The Ronald Press Company, 1954).

93. A. F. Ellis and J. Glover, "Mechanism of Fume Formation in Oxygen Steelmaking," J of the Iron and Steel Institute, pp 593-599 (August 1981).

94. D. G. C. Robertson and A. E. Jenkins, "The Reaction of Liquid Iron and Its Alloys in Pure Oxygen," Heterogeneous Kinetics at Elevated Temperatures, pp 393-408.

95. C. T. Crowe and W. J. Comfort, III, "Atomization Mechanisms in Single-Component, Two-Phase, Nozzle Flows," Proceedings of the First International Conference on Liquid Atomization and Spray Systems, The Fuel Society of Japan, Tokyo, Japan, August 27-31, 1978, Paper 2-3, pp 45-50.

96. L. D. Buxton and L. S. Nelson, "Impulse-Initiated Gas Release - A Possible Trigger for Vapor Explosions," Trans Am Nucl Soc 26, pp 398-399 (1977).

97. G. Taylor, "The Instability of Liquid Surfaces When Accelerated in a Direction Perpendicular to Their Plans I," Proc Roy Soc A 201, pp 192-196 (1950).

98. S. Chandrasekhar, "Hydrodynamic and Hydromagnetic Stability," (New York: Dover, 1981).

99. P. B. Gooderum and D. M. Bushnell, "Measurement of Mean Drop Sizes for Sprays from Superheated Waterjets," J Spacecraft and Rockets 6(2) (February 1969).

100. F. Aguilar and S. Thompson, "Nonequilibrium Flashing Model for Rapid Pressure Transients," ASME Paper 81-HT-35, 20th Joint ASME/AIChE National Heat Transfer Conference, Milwaukee, WI, August 2-5, 1981.

101. P. R. Garabedian, "On Steady-State Bubbles Generated by Taylor Instability," Proc Roy Soc (London) A241, pp 423-431 (1957).

102. G. Birkhoff, "Stability of Spherical Bubbles," Q Appl Math 13, pp 451-453 (1956).

103. M. S. Plesset and T. P. Mitchell, "On the Stability of the Spherical Shape of a Vapor Cavity in a Liquid," Q Appl Math 13, pp 419-430 (1956).

104. M. S. Plesset and A. Prosperetti, "Bubble Dynamics and Cavitation," Ann Rev Fluid Mech 9, pp 145-185 (1977).

105. J. C. Lasheras et al., "On the Disruptive Burning of Free Droplets of Alcohol/n-Paraffin Solutions and Emulsions," Eighteen Symposium (International) on Combustion, p 293, The Combustion Institute, 1981.

106. J. E. Brockmann and W. W. Tarbell, "Aerosol Source Term in High Pressure Melt Ejection," Nuc Sci and Eng, 88, pp 342-356 (1984).

107. R. R. Irani and C. F. Callis, Particle Size: Measurements, Interpretation and Applications, (New York: John Wiley and Sons, 1963).

108. F. Kottler, "The Distribution of Particle Sizes," Franklin Institute, Philadelphia Journal, V249-253, pp 339-356 (1950-52).

109. R. A. Mugele and H. D. Evans, "Droplet Size Distribution in Sprays," Ind and Eng Chem, 43(6), pp 1317-1324 (June 1951).

110. Robert S. Brodkey, The Phenomena of Fluid Motions, (Addison-Wesley, 1967).

111. Richard E. Sonntag and Gordon J. Van Wylen, Fundamentals of Statistical Thermodynamics, (New York: John Wiley and Sons, 1966).

112. T. Ginsberg, "Aerosol Generation by Liquid Breakup Resulting From Sparging of Molten Pools of Corium by Gases Released During Core/Concrete Interactions," Nuc Sci and Eng, 89, pp 36-48 (1985).

113. D. A. Powers, J. E. Brockmann, and A. W. Shiver, VANESA: A Mechanistic Model of Radionuclide Release and Aerosol Generation During Core Debris Interactions With Concrete, Sandia National Laboratories, Albuquerque, NM, NUREG/CR-4308, SAND85-1370, July 1986.

114. G. B. Wallis and H. J. Richter, "An Isentropic Streamtube Model for Flashing Two-Phase Vapor-Liquid Flow," J. Heat Transfer 100, pp 595-600 (November 1978).

115. O. C. Jones, Jr., "Flashing Inception in Flowing Liquids," J. Heat Transfer 102, pp 439-444 (August 1980).

116. W. C. Rivard and J. R. Travis, "A Nonequilibrium Vapor Production Model for Critical Flow," Nucl. Sci. Eng. 74, pp 40-48 (1980).

117. M. N. Hutcherson, R. E. Henry, and D. E. Wollersheim, "Two-Phase Vessel Blowdown of an Initially Saturated Liquid - Part 2: Analytical," Trans. ASME 105, pp 694-699 (November 1983).

118. R. J. Peterson, S. S. Grewal, and M. M. El-Wakil, "Investigations of Liquid Flashing and Evaporation Due to Sudden Depressurization," Int. J. Heat Mass Transfer 27(2), pp 301-310 (1984).

119. James M. Wu and Chun-Fa Chuang, "Consequence Analysis of a Steam Generator Tube Rupture Accident," Nucl. Technol 67, pp 381-406 (December 1984).

120. R. C. Anderson, C. A. Erdman, and A. B. Reynolds, "Droplet Size Distribution from Bulk Flashing," Nucl. Sci. Eng. 88(4), pp 495-512 (December 1984).

121. J. M. Schmidt, An Experimental Study of the Behavior of Liquid Streams Injected Into a Low-Pressure Chamber, Progress Report No. 4-94, Jet Propulsion Laboratory, California Institute of Technology, Pasadena, CA, April 22, 1949.

122. W. L. Short, "Some Properties of Sprays Formed by the Disintegration of a Superheated Liquid Jet," Ph.D. Dissertation, University of Michigan (1962).

123. J. M. Stephenson, A Study of Cavitating and Flashing Flows, Washington State University Institute of Technology, Bulletin No. 290, 1965.

124. H. S. Ostrowski, "Evaporation and Induced Air Flow in Sprays Produced by Superheated Water Jets," Ph.D. Dissertation, University of Michigan (1966).

125. J. H. Lienhard and J. M. Stephenson, "Temperature and Scale Effects Upon Cavitation and Flashing in Free and Submerged Jets," J. Basic Eng., Trans. ASME 88, Series D, pp 525-532 (June 1966).

126. J. H. Lienhard, "An Influence of Superheat Upon the Spray Configuration of Superheated Liquid Jets," J. Basic Eng., Trans. ASME 88, Series D, pp 685-687 (September 1966).

127. D. M. Bushnell and P. B. Gooderum, "Atomization of Superheated Water Jets at Low Ambient Pressures," J. Spacecraft and Rockets 5 (January-June 1968).

128. J. H. Lienhard and J. B. Day, "The Breakup of Superheated Liquid Jets," J. Basic Eng., Trans. ASME, 92, pp 516-522 (September 1970).

129. E. Sher and C. Elata, "Spray Formation from Pressure Cans by Flashing," Ind. Eng. Chem., Process Des. Dev. 16(2), pp 737-742 (1977).

130. A. S. P. Solomon, S. D. Rupprecht, L. D. Chen, and G. M. Faeth, "Atomization and Combustion Properties of Flashing Injectors," paper presented at the AIAA 20th Aerospace Sciences Meeting, AIAA-83-0300, Orlando, FL, January 11-14, 1982.

131. J. H. Lienhard, "Some Generalization of the Stability of Liquid-Gas-Vapor Systems," Int J Heat and Mass Transfer, 7, pp 813-817 (1964).

DISTRIBUTION:

U.S. Government Printing Office
Receiving Branch (Attn: NRC Stock)
8610 Cherry Lane
Laurel, MD 20707
505 copies for R1, R3, R5

U.S. Nuclear Regulatory
Commission (22)
Office of Nuclear Regulatory Research
Washington, DC 20555
Attn: E. S. Beckjord
C. N. Kelber
M. Silberberg
G. Marino
L. Chan
C. Ryder
R. W. Wright
T. Walker
R. O. Meyer
J. Mitchell
S. B. Burson
T. Lee (5)
M. Cunningham
J. Murphy
P. Wood
B. Hardin
Z. Rosztoczy
F. Eltawilla

U.S. Nuclear Regulatory Commission (6)
Office of Nuclear Regulatory
Regulation
Washington, DC 20555
Attn: L. G. Hulman
P. Easky
J. Rosenthal
R. Barrett
T. Speis
W. Lyon

U.S. Department of Energy (2)
Albuquerque Operations Office
P.O. Box 5400
Albuquerque, NM 87185
Attn: J. R. Roeder, Director
J. A. Morley, Director
For: C. B. Quinn
R. N. Holton

U.S. Department of Energy
Office of Nuclear Safety Coordination
Washington, DC 20545
Attn: R. W. Barber

Department of Energy (8)
Scientific and Technical Information
Center
P.O. Box 62
Oak Ridge, TN 37831

Electric Power Research Institute (4)
3412 Hillview Avenue
Palo Alto, CA 94303
Attn: R. Vogel
R. Ritzman
W. Lowonstein
R. Sehgal

Brookhaven National Laboratory (5)
Upton, NY 11973
Attn: R. A. Bari
T. Pratt
N. Tutu
G. Greene
T. Ginsberg

Professor R. Seale
Department of Nuclear Engineering
University of Arizona
Tucson, AZ 85721

Oak Ridge National Laboratory
P.O. Box Y
Oak Ridge, TN 37830
Attn: T. Kress

K. Holtzclaw
General Electric - San Jose
Mail Code 682
175 Kurtner Avenue
San Jose, CA 95125

Argonne National Laboratory (5)
9700 South Cass Avenue
Argonne, IL 60439
Attn: J. Rest
C. Johnson
L. Baker, Jr.
D. Cho
B. Spencer

Cathy Anderson
Nuclear Safety Oversight Commission
1133 15th St., NW
Room 307
Washington, DC 20005

Battelle Columbus Laboratory (3)
505 King Avenue
Columbus, OH 43201
Attn: P. Cybulskis
R. Denning
J. Gieseke

Peter Bieniarz
Risk Management Associates
2309 Dietz Farm Road, NW
Albuquerque, NM 87107

R. Deem
Power Authority State of NY
10 Columbus Circle
New York, NY 10019

Dr. S. J. Niemczyk
1545 18th Street, NW
#112
Washington, DC 20036

R. Sherry
JAYCOR
P.O. Box 85154
San Diego, CA 92138

Ktech Corp. (2)
901 Pennsylvania NE
Albuquerque, NM 87110
Attn: R. E. Blose
J. Jackson

Los Alamos National Laboratories
P.O. Box 1663
Los Alamos, NM 87545
Attn: M. Stevenson

UCLA (2)
Nuclear Energy Laboratory
405 Hilgaard Avenue
Los Angeles, CA 90024
Attn: I. Catton
D. Okrent

University of Wisconsin
Nuclear Engineering Department
1500 Johnson Drive
Madison, WI 53706
Attn: M. L. Corradini

EG&G Idaho
Willow Creek Building, W-3
P.O. Box 1625
Idaho Falls, Idaho 83415
Attn: R. Hobbins

Battelle Pacific Northwest Laboratory
P.O. Box 999
Richland, WA 99352
Attn: M. Freshley

W. Stratton
2 Acoma Lane
Los Alamos, NM 87544

Wang Lu
TVA
400 Commerce, W9C157-CK
Knoxville, TN 37902

M. Fontana
Director, IDCOR Program
ENERGEX
575 Oak Ridge Turnpike
Oak Ridge, TN 37830

Fauske and Associates, Inc. (2)
16W070 West 83rd Street
Burr Ridge, IL 60521
Attn: R. Henry
M. Plys

Wiktor Frid (5)
Swedish State Power Board
S-162 FACH 87 VALLINGBY
SWEDEN

J. E. Antill
Berkeley Nuclear Laboratory
Berkeley GL 139 PB
Gloucestershire
ENGLAND, UNITED KINGDOM

W. G. Cunliffe
Bldg. 396
British Nuclear Fuels, Ltd.
Springfields Works
Salwick, Preston
Lancashire
ENGLAND, UNITED KINGDOM

Professor Agustin Alonso
E.T.S. Ingenieros Industriales
Jose Gutierrez Abascal, 2
28006 Madrid
SPAIN

Dr. Alfonso Perez
Department de Seguridad Nuclear
Junta de Energia Nuclear
Avenida Complutense, 22
Madrid - 3
SPAIN

Gesellschaft fur Reaktorsicherheit
(GRS)
Postfach 101650
Glockengrasse 2
5000 Koeln 1
FEDERAL REPUBLIC OF GERMANY

Kraftwerk Union
Hammerbacher Strasse 1214
Postfach 3220
D-8520 Erlangen 2
FEDERAL REPUBLIC OF GERMANY
Attn: Dr. M. Peehs

UKAEA
Reactor Development Division (5)
Winfrith, Dorchester
Dorset DT2 8DH
ENGLAND, UNITED KINGDOM
Attn: R. Potter
A. Nichols
B. Bowsher
P. Smith
T. Butland

Nucleare e della Protezione Sanitaria
(DISP) (2)
Ente Nazionnle Energie Alternative
(ENEA)
Viale Regina Margherita, 125
Casella Postale M. 2358
I-00100 Roma A.D.
ITALY
Attn: Mr. Manilia
Mr. G Petrangeli

Dr. K. J. Brinkman
Reactor Centrum Nederland
1755 ZG Petten
THE NETHERLANDS

Kernforschungszentrum Karlsruhe
Postfach 3640
75 Karlsruhe
FEDERAL REPUBLIC OF GERMANY
Attn: H. Rininsland

Mr. H. Bairiot, Chief
Department LWR Fuel
Belgonucleaire
Rue de Champde Mars. 25
B-1050 Brussels
BELGIUM

Japan Atomic Energy Research
Institute (3)
Tokai-Mura, Naka-Gun
Ibaraki-Ken 319-11
JAPAN
Attn: S. Saito
Dr. K. Soda
K. Sato

P. Fehrenbach
Atomic Energy Canada, Ltd.
Chalk River, Ontario
CANADA KOJ IJO

M. Hayns
UKAEA
Safety and Reliability Directorate
Wigshaw Lane
Culcheth
Warrington WA3 4NE
Cheshire,
ENGLAND, UNITED KINGDOM

J. R. Mathews
Aere Harwell
Didcot
Oxfordshire OX11 ORA
ENGLAND, UNITED KINGDOM

F. Briscoe
UKAEA Culham Laboratory
Abingdon
Oxfordshire OX14 3DB
ENGLAND, UNITED KINGDOM

H. J. Teague (3)
UKAEA
Safety and Reliability Directorate
Wigshaw Lane
Culcheth
Warrington, WA3 4NE
ENGLAND, UNITED KINGDOM

M. Jankowski
IAEA
Division of Nuclear Reactor Safety
Wagranerstrasse 5
P.O. Box 100
A/1400 Vienna
AUSTRIA

Statens Karnkraftinspektion
L. Hammer
P. O. 27106
S-10252 Stockholm
SWEDEN

Studsvik Energiteknik AB
K. Johansson
S-611 82 Nykoping
SWEDEN

Atomic Energy Canada Ltd.
M. Notley
Chalk River, Ontario
CANADA KOJ IJO

Atomic Energy Canada Ltd. (2)
Pinawa, Manitoba
CANADA ROE 1LO
Attn: H. Reginger
D. Wren

Korea Adv Energy Research Inst
H. R. Jun
P. O. Box 7
Daeduk-Danji
Choong-Nam
KOREA

Institute of Nuclear Energy Research
Sen-I Chang
P.O. Box 3
Lungtan
Taiwan 325
REPUBLIC OF CHINA

Sandia Distribution:
3141 S. A. Landenberger (5)
3151 W. L. Garner
6400 D. J. McCloskey
6412 A. L. Camp
6413 E. D. Bergeron
6415 F. E. Haskin
6420 J. V. Walker
6421 P. S. Pickard
6422 D. A. Powers (5)
6422 F. E. Arellano
6422 J. E. Brockmann (2)
6422 E. R. Copus
6422 R. Gomez
6422 T. M. Kerley
6422 W. W. Tarbell (5)
6422 N. Yamano
6423 B. Marshall
6425 W. J. Camp
6425 M. Pilch (5)
6427 M. Berman
6427 L. Pong
6429 K. D. Bergeron
6429 D. E. Carroll
6429 K. E. Washington
6429 D. C. Williams
6440 D. A. Dahlgren
6442 W. A. Von Riesemann
6454 G. L. Cano
6512 D. M. Ericson, Jr.
7530 T. B. Lane
7537 N. R. Keltner
8524 P. W. Dean

NRC FORM 335 (2-84) NRCM 1102, 3201, 3202

U.S. NUCLEAR REGULATORY COMMISSION

BIBLIOGRAPHIC DATA SHEET

SEE INSTRUCTIONS ON THE REVERSE

1 REPORT NUMBER (Assigned by TIDC, add Vol. No., if any)

NUREG/CR-4508
SAND85-1726

2 TITLE AND SUBTITLE

BEHAVIOR OF A CORIUM JET IN HIGH PRESSURE MELT EJECTION FROM A REACTOR PRESSURE VESSEL

3 LEAVE BLANK

4 DATE REPORT COMPLETED

MONTH: February | YEAR: 1988

5 AUTHOR(S)

Wiktor Frid

6 DATE REPORT ISSUED

MONTH: April | YEAR: 1988

7 PERFORMING ORGANIZATION NAME AND MAILING ADDRESS (Include Zip Code)

Sandia National Laboratories
Division 6422
Albuquerque, NM 87185-5800

8 PROJECT/TASK/WORK UNIT NUMBER

9 FIN OR GRANT NUMBER

FIN A1406

10 SPONSORING ORGANIZATION NAME AND MAILING ADDRESS (Include Zip Code)

U. S. Nuclear Regulatory Commission
Office of Nuclear Regulatory Research
Division of Reactor Accident Analysis

11a TYPE OF REPORT

SAND

b PERIOD COVERED (Inclusive dates)

12 SUPPLEMENTARY NOTES

13 ABSTRACT (200 words or less)

This report provides results from analytical and experimental investigations on the behavior of gas supersaturated molten jet expelled from a pressurized vessel. Models are developed for jet expansion, primary breakup of the jet, and secondary fragmentation of melt droplets. The jet expansion model is based on a general relation for bubble growth which includes both inertial-controlled and diffusion-controlled growth phase. The model is able to predict the jet void fraction, jet radius as a function of axial distance from the pressure vessel bubble size, and bubble pressure. Predicted fragment sizes are in reasonably good agreement with the data.

Parametric caluclations for a TMLB' accident show that the corium jet is disrupted within a few initial jet diameters from the vessel. The radius of the corium jet at the level of the reactor cavity floor is predicted to be in the range 0.8m - 2.6m.

14 DOCUMENT ANALYSIS - a KEYWORDS/DESCRIPTORS

Reactor Accident
High Pressure Melt Ejection
Molten Jet
Aerosol
Jet Expansion

b IDENTIFIERS/OPEN ENDED TERMS

15 AVAILABILITY STATEMENT

16 SECURITY CLASSIFICATION

(This page)

(This report)

17 NUMBER OF PAGES

18 PRICE

☆ U.S. GOVERNMENT PRINTING OFFICE: 1988—573-049/61052